

# Bridging pico-to-nanoNewton: Ratiometric Force Probe for Nanoscale Polymer Physics Before Damage

Ryota Kotani<sup>1</sup>, Soichi Yokoyama<sup>1</sup>, Shunpei Nobusue<sup>2</sup>, Shigehiro Yamaguchi<sup>3</sup>, Atsuhiko Osuka<sup>1</sup>, Hiroshi Yabu<sup>4\*</sup>, Shohei Saito<sup>1,5\*</sup>

## Affiliations:

<sup>1</sup>Graduate School of Science, Kyoto University, Japan.

<sup>2</sup>Institute of Advanced Energy, Kyoto University, Japan.

<sup>3</sup>Graduate School of Science, Nagoya University, Japan.

<sup>4</sup>WPI-Advanced Institute for Materials Research (AIMR), Tohoku University, Japan.

<sup>5</sup>PRESTO, Japan Science and Technology Agency

**Abstract:** Understanding nanoscale force transmission in pico-to-nanoNewton range is important in polymer physics. While physical approaches have limitations to analyze local force distribution in condensed environments, chemical doping of mechano-probes is promising. However, there are demanding requirements to probe the local force without structural damage, which corresponds to the force range below covalent bond scission (nanoNewton) and over thermal fluctuation (picoNewton). Here we report a conformationally flexible dual fluorescent mechano-probe with 100-picoNewton threshold that realizes ratiometric analysis on nanoscale force distribution in stretched polymer chain network. Without changing original polymer properties, the force distribution has been reversibly monitored in real time. Chemical control of the probe location demonstrated that local stress concentration is twice more biased at crosslinkers than main chains particularly in a strain-hardening region.

## Main Text:

Understanding pico-to-nanoNewton force transmission in complex hierarchical structures is a main goal in polymer physics (1) and mechanobiology (2). Physical approaches such as optical/magnetic tweezers and atomic force microscopy (AFM) are widely used to evaluate picoNewton force, while these techniques have difficulty in obtaining mechanical force distribution inside condensed materials or molecular crowding environments (Fig. 1A). (3) Instruments of surface force apparatus (SFA), rheometer, and tensile testing are also available for studying more than micro-Newton force transmitted in meso-to-macroscopic structures, but direct quantification method of molecular-level force distribution is still being pursued. Promising alternative is a chemical doping of mechano-responsive molecules as a force probe (4). Those chromophores for materials- and biology-oriented purposes have been independently developed in this decades, because the force ranges of interest are different in these fields. While FRET-type chromophore conjugates have been developed to analyze several picoNewton in mechanobiology (5-8), a variety of mechanophores show responses in several nanoNewton with an internal covalent bond scission (9-11), giving rise to the upsurge of stress-responsive materials (12-18). On the other hand, there are still severe requisites in the design of a force probe that can realize quantitative monitoring of local stress concentration before damage of polymer chain network, without changing original polymer properties by covalent doping. Although sacrificial bond scission of

polymer materials has been monitored using turn-on mechanophores (19,20), nanoscale force distribution in entangled polymer chains has not been elucidated, in spite of the importance for reasonable design of unique tough materials (21-25). Target force range for this purpose is around 10–100 piconewton, below covalent bond scission (several nanoNewton) and beyond spontaneous thermal fluctuation at room temperature ( $k_B T = 4.1$  pN nm) (26) (Fig. 1B). Here we demonstrated that a conformationally flexible flapping mechano-probe enables this study by ratiometric analysis of its bright dual fluorescence, in which well-suited potential energy profiles are designed in the ground state ( $S_0$ ) and the lowest singlet excited state ( $S_1$ ). High brightness permits minimum chemical doping to preserve original polymer properties. By controlling chemical locations of the probe in crosslinked polymers, new quantitative insights into biased nanoscale stress concentration have been obtained through real-time observation of the dual emission from stretched polymers.

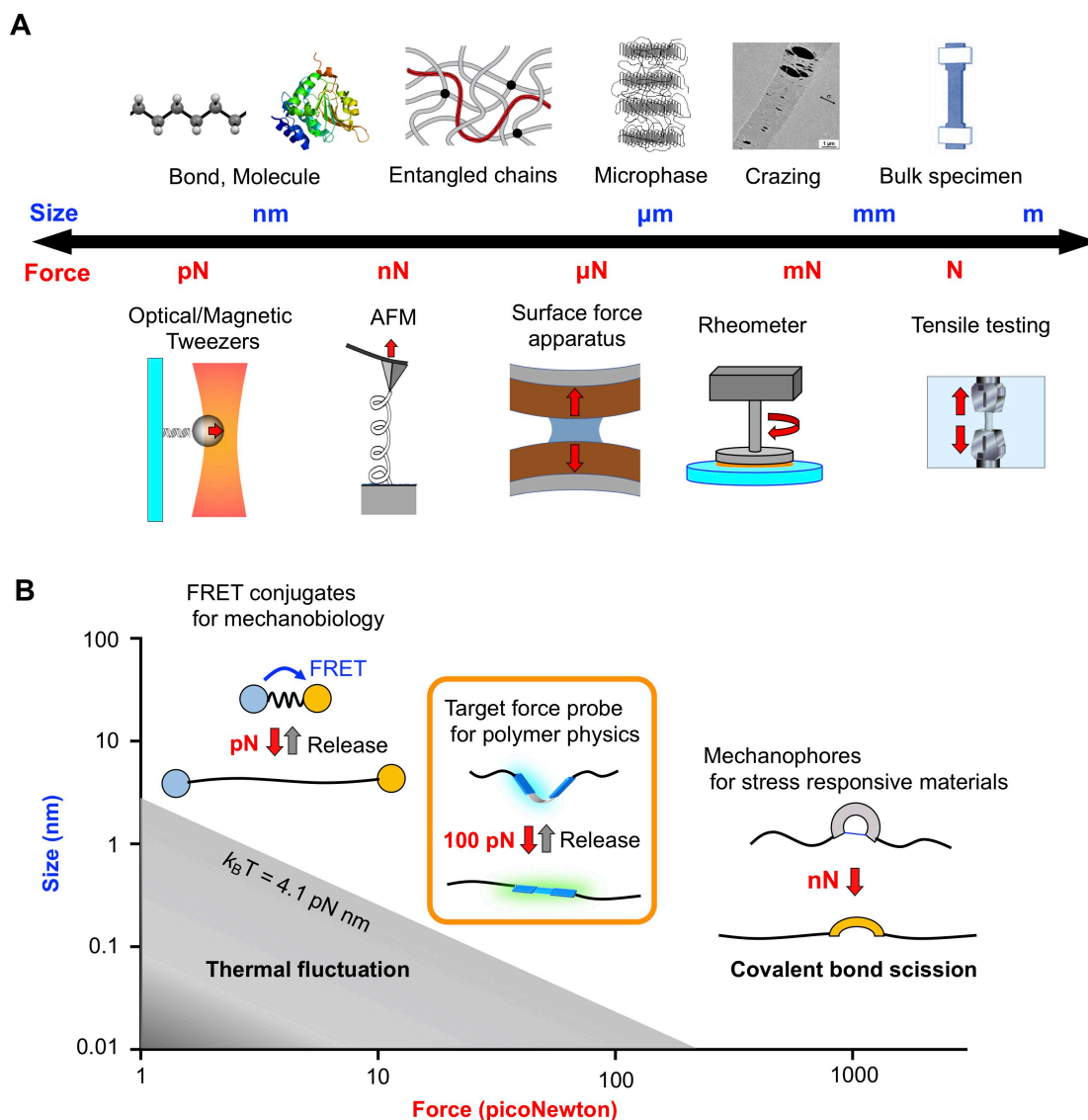


**Fig. 1.** (A) Hierarchical structures of materials and physical measurement methods of mechanical force in different scales. (B) Target force range for nanoscale study of polymer physics.

## Dual fluorescent flapping molecular probe

A flapping molecule (FLAP), composed of two rigid anthraceneimide wings fused with a conformationally flexible eight-membered ring (cyclooctatetraene, COT), shows dual fluorescence (FL) property (Fig. 2A,B) (27). In  $S_0$ , a bent form is most stable, while a planar form has higher energy due to strain effects of the flat COT ring (28). On the other hand, FLAP has two energy minima in  $S_1$  at bent and planar geometries. Emissions from these minima are both allowed, exhibiting a blue FL around 460 nm and a green FL around 520 nm, respectively. Since the energy barrier is low and the planar geometry is slightly more stable in  $S_1$ , FLAP takes a bent-to-planar conformational change within subnanosecond timescale after UV excitation in a solution phase, emitting the green FL dominantly with high FL quantum yield ( $\Phi_F \approx 0.3$ ). Population of excited species at these  $S_1$  minima are largely dependent on local viscosity in solution, while polarity dependence can be ignored due to the non-charge-transfer character (29). Whereas the viscosity probing function is active in the presence of solvent molecules, the planarization dynamics crossing the barrier in  $S_1$  is suppressed in a polymer matrix, and then the blue FL is only observed ( $\Phi_F \approx 0.3$ ). On the other hand, compulsory planarization in  $S_0$  can be induced by external force, as we demonstrated the mechanophore function in a crystal phase transition of FLAP (30). Among conformationally flexible mechanophores that can show detectable signals without covalent bond scission (31-33), FLAP is unique in its dual FL property, which enables ratiometric FL analysis (Fig. 2B). Although a variety of single-component dual-fluorescent chromophores have been reported in photochemistry (34, 35), the force probe application has not been reported. By the ratiometric FL analysis, quantitative evaluation can be realized even when the molecular force probes are distributed heterogeneously and the concentration of the probe changes by polymer deformation.

## 100-pN threshold for the fluorescence switching before covalent bond elongation

Flapping mechanophores (FLAPs) with OH groups were prepared for covalent doping in polycarbonate (PC) and polyurethane (PU). Terminal bulky substituents were introduced for suppressing aggregation of FLAPs (36). Due to the high brightness, doping ratio can be minimized less than  $10^{-4}$  equivalent to other monomer components. Original mechanical properties of host polymers were preserved by the covalent doping (Fig. S20 for PC and Fig. S27 for PU), which is the essential requisite for a force probe. Average distance between doped FLAP molecules was estimated to be  $\approx 20$  nm, much farther than the distance allowed for Förster resonance energy transfer (FRET,  $< 10$  nm). Negative control experiments by the corresponding physical doping confirmed almost no mechanical response of FLAP (Fig. S38). First, we confirmed a sensitive mechanical response of FLAP in the chemically doped polymeric environments. A linear PC prepared from the components in Fig. 2C showed less elastomeric property, rather glassy with glass transition temperature  $T_g$  of 153 °C (Table S14), thereby permitting microscopy observation with small displacement. When the notched PC film was slowly stretched on the inverted microscopy, equipped with a compact tensile testing machine and a hyperspectral camera, rapid growth of stressed region was visualized in micro-to-millimeter scale by a FL change from bluish to greenish colors under UV light. Two-dimensional imaging as a function of the ratio in the FL intensities at 525 and 470 nm made the situation clearer. The spectral response started much earlier than crack propagation from the notch (Fig. 2D). This result strongly suggested that the conformational planarization of FLAP can be specifically induced prior to covalent bond scission of the stressed polymer chains. In addition, the green FL enhancement was less pronounced in a backward region of the crack (region b), in comparison with the crack tip (region c). This

observation indicates spatial transmission of the relaxation process, whereas the mechanically irreversible chromophores have a limitation to trace the relaxation after the activation (12,20).

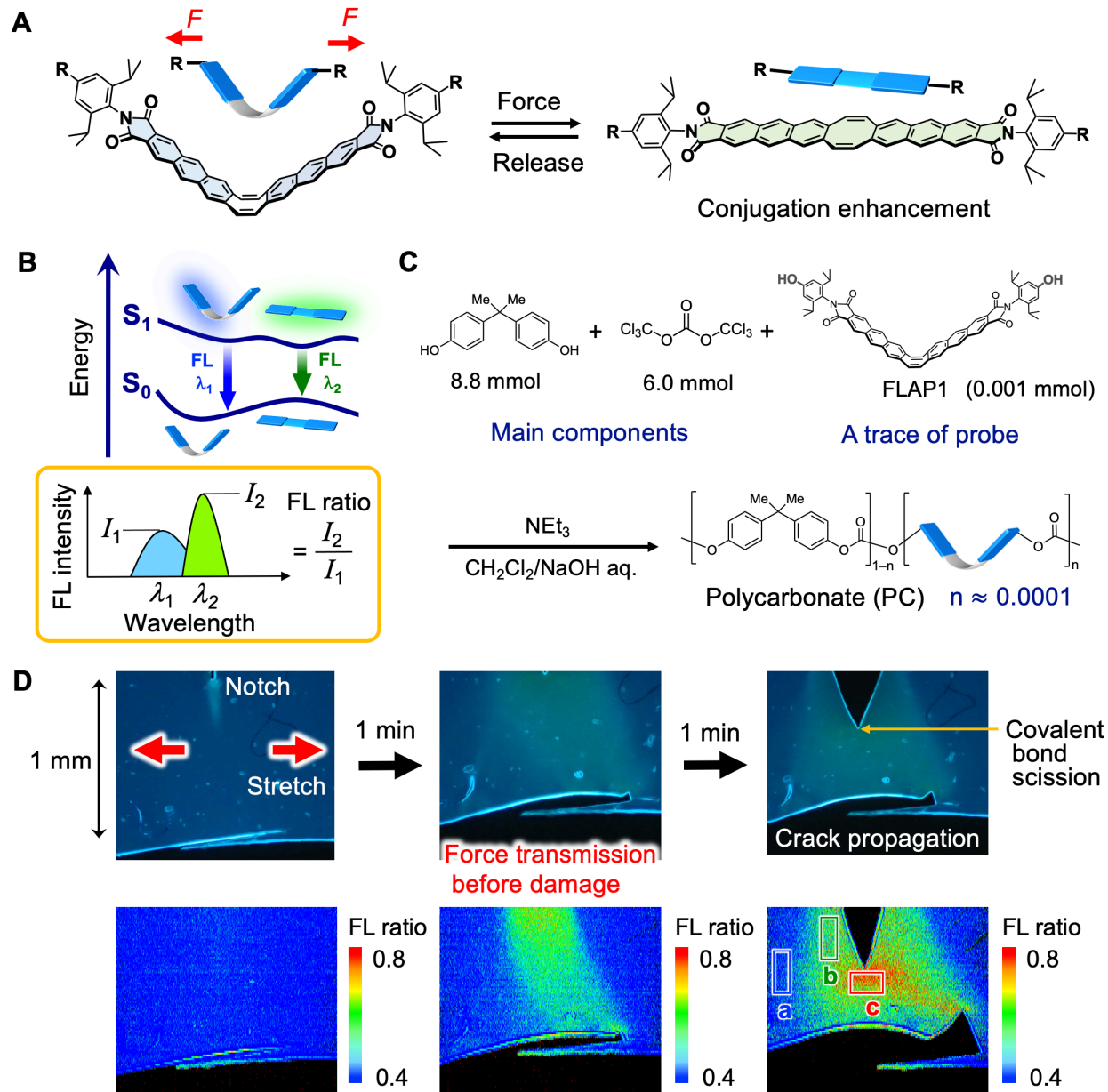


**Fig. 2.** (A) Dual-fluorescent flapping molecular force probe (FLAP) that enables (B) quantitative ratiometric analysis. (C) Preparation of PC from bisphenol A and triphosgene, chemically-doped with a trace of FLAP1 (0.05 wt%). (D) Fluorescence microscopy images of the notched PC specimen under 365-nm UV irradiation. Force transmission induced before crack propagation by tensile testing (strain rate of  $2.0 \times 10^{-3} \text{ s}^{-1}$ ) in several minutes (top). The corresponding two-dimensional ratiometric FL imaging ( $\text{FL}_{525}/\text{FL}_{470}$ ), obtained by a hyperspectral camera (bottom). In the last image, an unstretched region (a), a backward region of the crack (b), and the crack tip (c) were indicated.

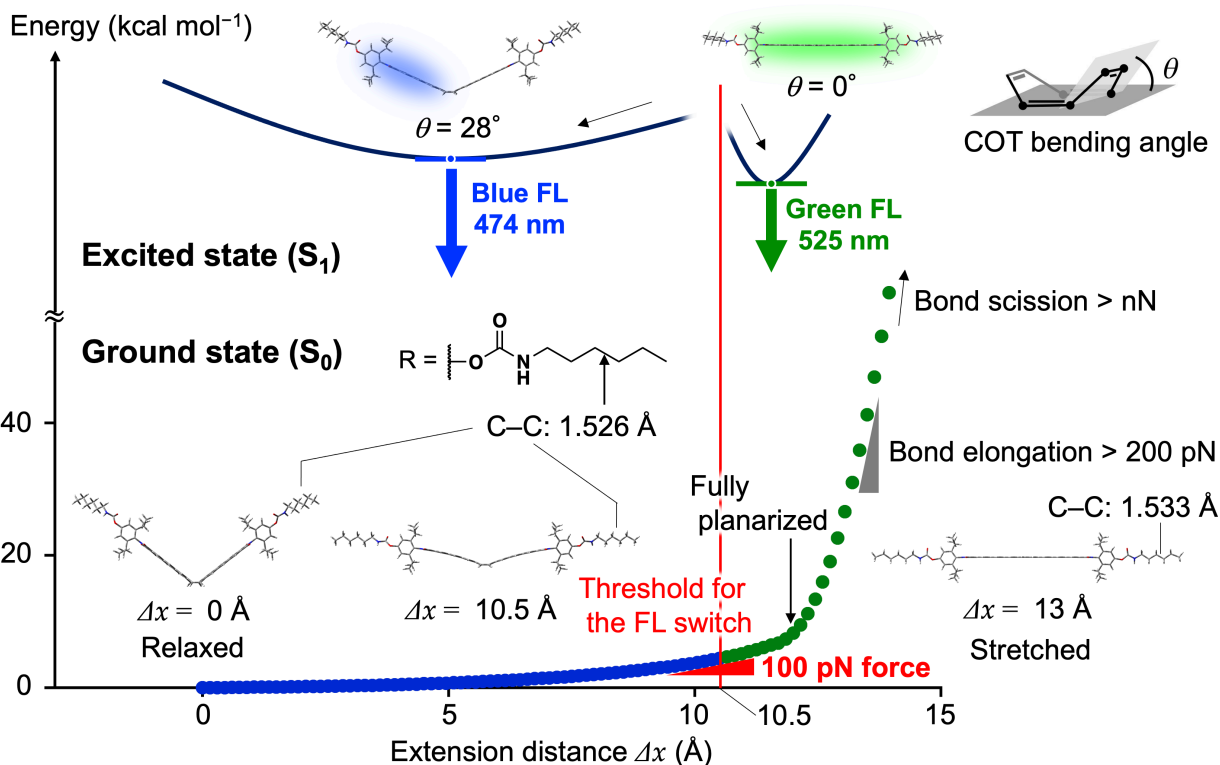


**Fig. 3.** DFT calculated energy profile of a polymer-chain substructure in the vicinity of FLAP ( $R = N$ -hexylcarbamate in Fig 2A). Constrained geometry optimization was performed in  $S_0$  at the PBE0/6-31G(d) level (bottom), in which the distance between terminal carbon atoms was fixed. From the most relaxed geometry, the relative potential energy was scanned as a function of extension,  $\Delta x$ , by 0.15 Å. Excited-state geometry optimization in  $S_1$  at the TD-PBE0/6-31G(d) level was also performed (top) for each geometry obtained in  $S_0$ , where the extension was fixed at the same length. The presence of two relaxed conformers of the FLAP skeleton were indicated in  $S_1$ , whose COT bending angles were 28° (bent) and 0° (planar). Note that the conformational coordinates along the abscissa in  $S_1$  (top) is different from that of  $S_0$  (bottom) in this Figure.

To estimate the threshold of the FL switch at the single-molecule level, (TD-)DFT calculations were performed in  $S_0$  and  $S_1$  on the polymer substructure in the vicinity of FLAP (Fig. 3). Energy profile in  $S_0$  was obtained by plotting relative potential energy of optimized geometries with a fixed distance between terminal carbon atoms. When the structure is relaxed with minimum energy, the distance is 40.4 Å (where extension = 0 Å) and the COT bending angle takes 40.2°. Scanning extension until 15 Å indicated that, in the early stage, the planarization of FLAP occurs specifically without C-C bond elongation in the terminal carbon chains. The planarization completed by 12.0-Å extension is an energetically uphill process, but it only requires 6.7 kcal/mol. Steepness of the early-stage slope, that is the required force for the conformational planarization, is several tens of pico-Newton (pN). Rapid energy increase over 200-pN slope is displayed by further extension, involving the covalent bond elongation. Note that a C-C bond length in the side chain becomes longer, only after the FLAP planarization (Fig S14). Eventually, the side chain breaks outside the FLAP skeleton. To determine the threshold for the FL switching, the corresponding  $S_1$  energy profile must be also considered, because small conformational relaxation in  $S_1$  should be expected

even in the polymeric environment that suppresses a large structural change in principle. In fact, FL spectral conversion by stretching FLAP-doped PUs (see Fig. 4) only showed relative intensity change of two FL bands at 474 and 525 nm, rather than a gradual red shift, which indicates accumulated population of the excited species at two  $S_1$  minima. Since the  $S_1$  relaxation of FLAP proceeds in ultrafast timescale (29), polymer chains around the force probe cannot move at the moment. Therefore, further optimizations in  $S_1$  were conducted with the same extension at each geometry obtained in  $S_0$ . Importantly, the  $S_1$  optimization from half stretched structures below and above 10.5-Å extension converged into two specific conformations of the FLAP skeleton, in which the COT bending angles were 28° (bent) and 0° (planar). Accordingly, the threshold of the FL switching can be expected around the 10.5-Å extension, at which the activation energy is calculated to be 4.5 kcal/mol with the required force of 100 pN.

### **Controlling chemical location of the force probe in crosslinked polyurethanes**

We obtained a new quantitative insight into biased local stress concentration in crosslinked PUs, by controlling chemical location of FLAP as a force probe. Two different polyurethanes, PU1 and PU2, were synthesized by chemical doping of FLAP1 and FLAP2, respectively (Fig. 4A). Photophysical properties of FLAP1 and FLAP2 were identical in solution. Due to the different numbers and positions of the reactive OH groups, FLAP1 is incorporated into a PU main chain, while FLAP2 into a crosslinking point. Except for the difference in the probe locations, the following parameters of these PUs are all the same: stoichiometric amounts of monomer components, polymerization conditions using a tin catalyst, and preparation for dumbbell-shaped test specimen. Indeed, PU1 and PU2 as well as undoped PU (PU0) reproducibly showed ignorable difference in mechanical and thermal properties (Fig. 4B and Fig. S25–27). In Fig 4, crosslinking density, the molar fraction of triethanolamine (TEA) to the sum of the monomers, was set to be 0.10, where the molar ratio of FLAP1 and FLAP2 was small enough to be ignored (0.0001 equivalent to the poly(tetrahydrofuran) (PTHF) monomer, 0.02 wt% to the obtained PUs). Stress–strain curve of the PU specimens indicated highly elastomeric properties (Fig. 4B). Typical rubbery deformations with Young’s modulus of 1.0–1.1 MPa were confirmed for these PUs. Yield point was not clearly observed for the rubbery PU. After a typical plateau-like region around 1 MPa, strain-hardening started around 500% strain, and eventually rupture occurred around 750% strain with  $\approx 6$  MPa. It is worth noting that the rubbery PU was gradually transformed into semi-crystalline PU in several days (Figs. S39–41), as we focused the rubbery PUs in this study.

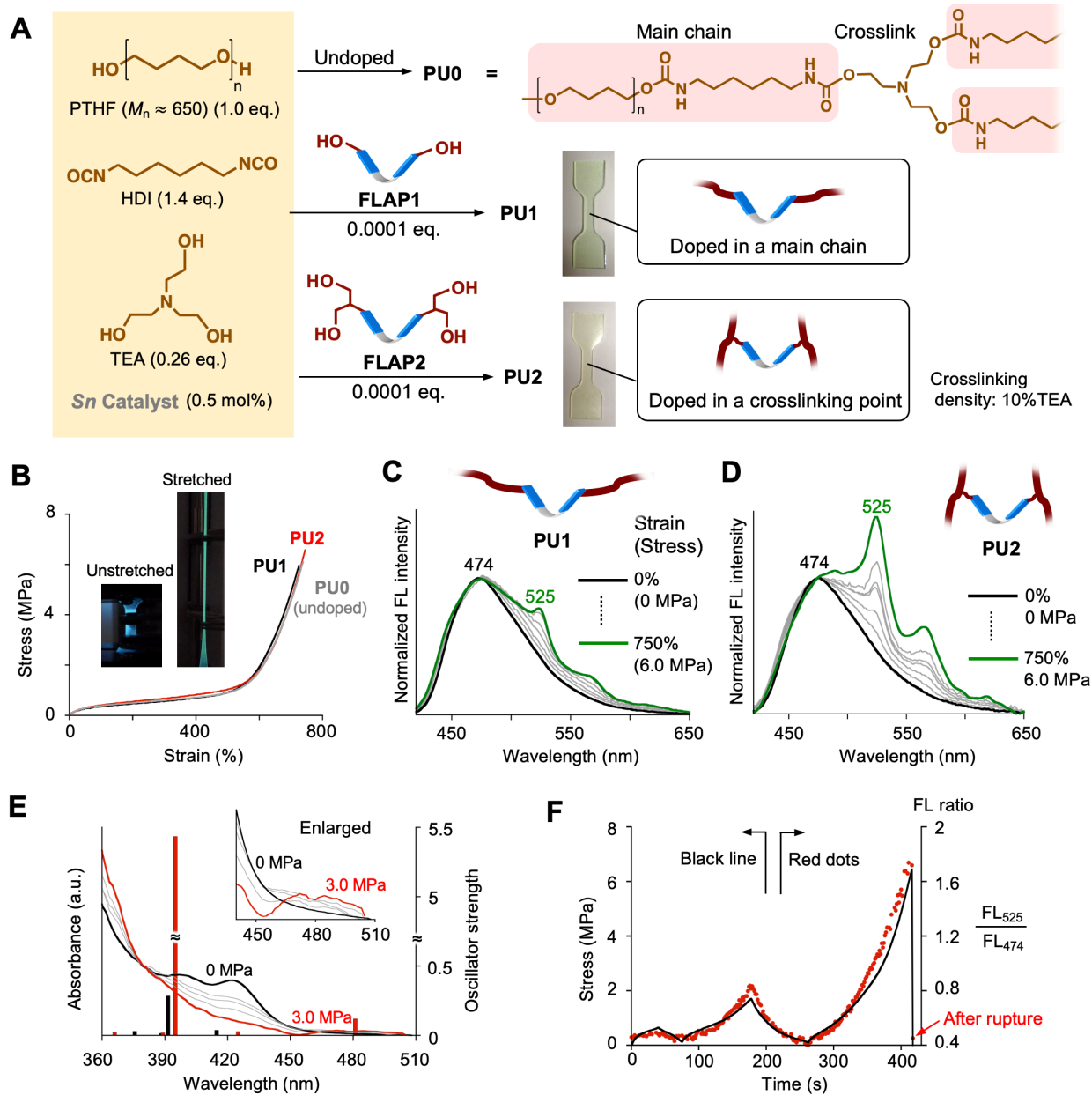


**Fig. 4.** (A) Controlled chemical doping of FLAP1 and FLAP2 in crosslinked polyurethanes, PU1 and PU2, respectively. PTHF: poly(tetrahydrofuran); HDI: hexamethylenediisocyanate; TEA: triethanolamine; Sn catalyst: dibutyltin dilaurate. Crosslinking density can be tuned by molar ratio of TEA to the other monomer components. (B) Stress–strain curves of rubbery polyurethanes, PU1, PU2 and undoped PU0 with the crosslinking density of 10%TEA. Inset images: the unstretched and stretched fluorescent specimens of PU2 under UV light. (C,D) FL spectral changes during the tensile testing of PU1 and PU2. FL intensity was normalized at 474 nm. Excitation wavelength: 365 nm. (E) An absorption spectral change of PU2 by stretching the specimen. Oscillator strengths were calculated at the unstretched and fully stretched geometries (Tables S12 and S13) at the TD PBE0/6-31+G(d) level. (F) Real-time FL response during the loading–unloading cycle of PU2. Time-dependent stress (black) and FL ratio plots (red).

## Fluorescence spectroscopy simultaneously conducted with tensile testing

During the mechanical testing, FL spectra of the PU specimens were measured in a real-time manner (Fig. 4C and 4D). Under continuous UV irradiation (365 nm,  $\approx 100 \text{ mW cm}^{-2}$ ), the fluorescence emission was collected by an optical fiber connected to a multi-channel photodetector. Before stretching, both PU1 and PU2 showed the same blue FL band with a single peak top at 474 nm, corresponding to the emission from the bent FLAP conformation in  $S_1$ . As the stress increased, a green FL band at 525 nm appeared along with vibronic sub-bands at 565 and 618 nm, emitted from the planarized conformation. On the other hand, even in the late stage of stretching, the blue FL band did not disappear, meaning that significant numbers of the force probes are still relaxed just before rupture of specimens. Namely, the macroscopic stress was not ideally distributed to the whole polymer network. The nanoscale stress concentration cannot be discussed by using “turn-on” mechanophores that show no characteristic signal in their unactivated forms. More importantly, the relative degree of the green FL enhancement was remarkably larger in PU2 than PU1, clearly indicating biased nanoscale stress concentration at the crosslinkers, compared with the PU main chains. Stretch-induced absorption spectral change was also confirmed for PU2 (Fig. 4E). Appearance of a detectable absorption band in the long-wavelength region reaching 500 nm provided the strong evidence for the compulsory conformational change of FLAP in the ground state. This weak absorption band can be assigned to a partially allowed  $S_0$ -to- $S_2$  excitation (Table S13), of the effectively  $\pi$  conjugated system at the (almost) planar FLAP conformation in  $S_0$ . Loading-unloading cycle test was also carried out to confirm a repeated and real-time response of the mechanically reversible force probe (Fig. 4F and Fig. S36). The FL ratio beautifully traced time-dependent stress macroscopically loaded on the PU specimen. After the rupture, the ratio value went back immediately to the extent of the unstretched initial phase, which confirmed the reversible response of the FLAP force probe as well as the ignorable influence of photodegradation.

## Quantifying biased nanoscale stress concentration by ratiometric fluorescence analysis

The biased stress concentration at crosslinking points was demonstrated in different crosslinking densities of 8.7%, 10% and 13%TEA (Fig. 5). Stress-strain curves of these polyurethanes are shown in Fig. 5A. The rupture stress and the rupture strain became smaller as the crosslinking density increased. Strain-hardening region of the highly crosslinked PU (13%TEA) started earlier from  $\approx 400\%$  strain, while the other PUs from  $\approx 500\%$  strain. The FL ratio values ( $FL_{525}/FL_{474}$ ) were plotted as a function of strain and stress, respectively (Fig. 5B, C). Here we obtained an important insight. For all these PU2 specimens containing FLAP at crosslinking points, the FL ratio remarkably increased in the strain-hardening region. This behavior is in sharp contrast to the moderate increase in the PU1 specimens with FLAP at main chains. In the plateau-like region below 1-MPa stress, the FL ratios were not largely different between PU1 and PU2, indicating that the local stress concentration were observed to the same degree at main chains and crosslinkers. However, biased stress concentration at crosslinkers became pronounced in the strain-hardening process over 1-MPa stress. With decreasing the crosslinking density, the gap of the FL ratios between PU1 and PU2 at the rupture point became larger. On the other hand, when we focus on the specific strain level in a strain-hardening region (for example 600% strain), generated macroscopic stress were larger in more highly crosslinked polymers, and, accordingly, the FL ratio values for PU1 and PU2 were relatively larger at the same strain. On the basis of spectral separation analysis of the dual FL, we have estimated the corresponding percentage of the number of the stressed FLAP probes over the threshold for the FL switching, where the efficiencies of UV absorption and FL emission of the bent and planar conformations were theoretically considered

(Fig. 4D and Fig S37). With the 10%TEA crosslinking density, the estimated stressed-probe percentage at the rupture point even reached up to  $18.3 \pm 1.5\%$  (PU2) among the crosslinking FLAPs, whereas that in the main chains were around  $8.8 \pm 0.9\%$  (PU1). Note that the low threshold (100 pN) of the FLAP force probe made the stressed-probe percentage more than 1000 times larger in comparison with reported mechanophores that require covalent bond dissociations (37).

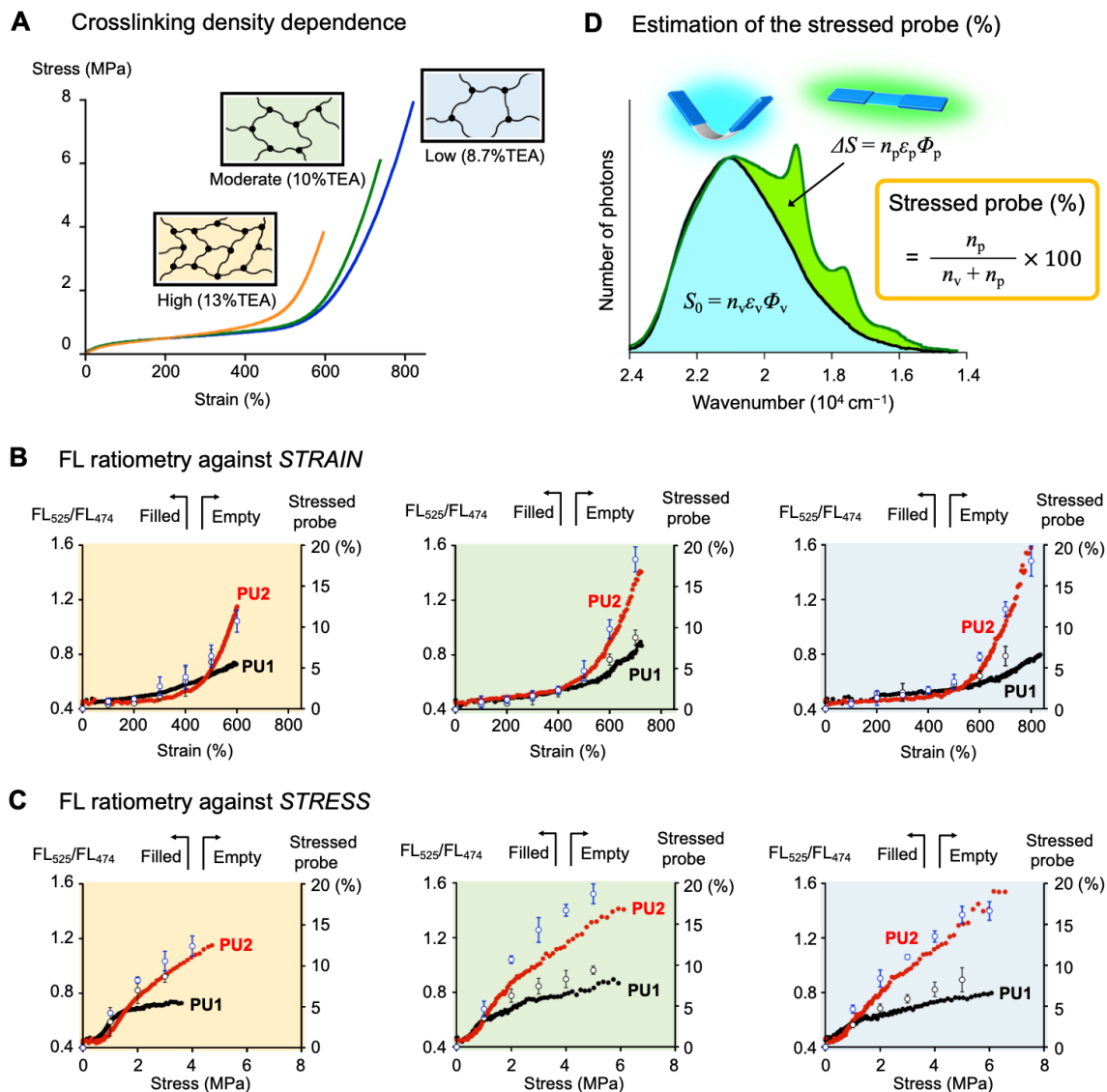


**Fig. 5.** (A) Stress-strain curves of undoped PU0 with the different crosslinking densities. Almost same curves were obtained for PU1 and PU2 at each crosslinking density (Fig S27). (B,C) FL ratio (filled circles) and percentages of the stressed FLAP probe (unfilled circles) as a function of strain (B) and stress (C) in tensile testing. Error bars in the stressed probe (%) indicate standard deviation obtained from three tensile tests. Note the color correspondence of the crosslinking density in (A–C). (D) Estimation of the stressed probe (%) over the 100-pN threshold, on the basis of an observed FL spectrum.  $n$ : number of FLAP molecules,  $\epsilon$ : molar absorption coefficient at the excitation wavelength (365 nm), and  $\Phi$ : FL quantum yield, where the subscripts of “v” and “p” means V-shaped (bent) and planar conformers, respectively. See the details in Fig S37.

## References and Notes:

1. Y. C. Simon, S. L. Craig, *Mechanochemistry in Materials* (Royal Society of Chemistry, UK 2017; vol 26).
2. T. Iskratsch, H. Wolfenson, M P. Sheetz, Appreciating force and shape — the rise of mechanotransduction in cell biology. *Nat. Rev. Mol. Cell Biol.* **14**, 825–833 (2014).
3. K. C. Neuman, A. Nagy, Single-molecule force spectroscopy: optical tweezers, magnetic tweezers and atomic force microscopy. *Nat. Methods.* **5**, 491–505 (2008).
4. Z. Huang, R. Boulatov, Chemomechanics with molecular force probes. *Pure Appl. Chem.* **82**, 931–951 (2010).
5. A. Freikamp, A.-L. Cost, C. Grashoff, The Piconewton Force Awakens: Quantifying Mechanics in Cells, *Trends in Cell Biol.* **26**, 838–847 (2016).
6. Y. Liu, K. Galior, V. P.-Y. Ma, K. Salaita, Molecular Tension Probes for Imaging Forces at the Cell Surface, *Acc. Chem. Res.* **50**, 2915–2924 (2017).
7. F. Meng, T. M. Suchyna, F. Sachs, A fluorescence energy transfer-based mechanical stress sensor for specific proteins in situ. *FEBS J.* **275**, 3072–3087 (2008).
8. C. Grashoff, B. D. Hoffman, M. D. Brenner, R. Zhou, M. Parsons, M. T. Yang, M. A. McLean, S. G. Sligar, C. S. Chen, T. Ha, M. A. Schwartz, Measuring mechanical tension across vinculin reveals regulation of focal adhesion dynamics. *Nature*, **466**, 263–267 (2010).
9. I. M. Klein, C. C. Husic, D. P. Kovács, N. J. Choquette, M. J. Robb, Validation of the CoGEF Method as a Predictive Tool for Polymer Mechanochemistry. *J. Am. Chem. Soc.* **142**, 16364–16381 (2020).
10. M. N. Silberstein, J. Ribas-Arino, D. Mark, Covalent Mechanochemistry: Theoretical Concepts and Computational Tools with Applications to Molecular Nanomechanics. *Chem. Rev.* **112**, 5412–5487 (2012).
11. C. L. Brown, S. L. Craig, Molecular engineering of mechanophore activity for stress-responsive polymeric materials. *Chem. Sci.* **6**, 2158–2165 (2015).
12. D. A. Davis, A. Hamilton, J. Yang, L. D. Cremar, D. V. Gough, S. L. Potisek, M. T. Ong, P. V. Braun, T. J. Martínez, S. R. White, J. S. Moore, N. R. Sottos, Force-induced activation of covalent bonds in mechanoresponsive polymeric materials. *Nature* **459**, 68–72 (2009).
13. M. M. Caruso, D. A. Davis, Q. Shen, S. A. Odom, N. R. Sottos, S. R. White, J. S. Moore, Mechanically-Induced Chemical Changes in Polymeric Materials. *Chem. Rev.* **109**, 5755–5798 (2009).
14. Y. Chen, A. J. H. Spiering, S. Karthikeyan, G. W. M. Perers, E. W. Meijer, R. P. Sijbesma, Mechanically induced chemiluminescence from polymers incorporating a 1,2-dioxatane unit in the main chain. *Nat. Chem.* **4**, 559–562, (2012).
15. J. Li, C. Nagamani, J. S. Moore, Polymer Mechanochemistry: From Destructive to Productive. *Acc. Chem. Res.* **48**, 2181–2190 (2015).
16. Z. Chen, J. A. M. Mercer, X. Zhu, J. A. H. Romaniuk, L. Cegelski, T. J. Martinez, N. Z. Burns, Y. Xia, Mechanochemical unzipping of insulating poly ladderene to semiconducting polyacetylene. *Science* **357**, 475–479 (2017).

17. K. Imato, H. Otsuka, Reorganizable and stimuli-responsive polymers based on dynamic carbon-carbon linkages in diarylbibenzofuranones. *Polymer* **137**, 395-413 (2018).
18. N. Willis-Fox, E. Rognin, T. A. Aljohani, R. Daly, Polymer Mechanochemistry: Manufacturing Is Now a Force to Be Reckoned With. *Chem* **4**, 1–39, (2018).
19. E. Ducrot, Y. Chen, M. Bulters, R. P. Sijbesma, C. Creton. Toughening Elastomers with Sacrificial Bonds and Watching Them Break. *Science* **344**, 186–189 (2014).
20. J. Slootman, V. Waltz, C. J. Yeh, C. Baumann, R. Göstl, J. Comtet, C. Creton, Quantifying and mapping covalent bond scission during elastomer fracture. <https://arxiv.org/abs/2006.09468> (2020).
21. J. P. Gong, Y. Katsuyama, T. Kurokawa, Y. Osada, Double-Network Hydrogels with Extremely High Mechanical Strength. *Adv. Mater.* **15**, 1155–1158 (2003).
22. Y. Okumura, K. Ito, The Polyrotaxane Gel: A Topological Gel by Figure-of-Eight Cross-links. *Adv. Mater.* **13**, 485–487 (2001).
23. J.-Y. Sun, X. Zhao, W. R. K. Illeperuma, O. Chaudhuri, K. H. Oh, D. J. Mooney, J. J. Vlassak, Z. Suo, Highly stretchable and tough hydrogels. *Nature* **489**, 133–136 (2012).
24. E. Filippidi, T. R. Cristiani, C. D. Eisenbach, J. H. Waite, J. N. Israelachvili, B. K. Ahn, M. T. Valentine, Toughening elastomers using mussel-inspired iron-catechol complexes. *Science* **358**, 502–505 (2017).
25. T. Matsuda, R. Kawakami, R. Namba, T. Nakajima, T., J. P. Gong, Mechanoresponsive self-growing hydrogels inspired by muscle training. *Science* **363**, 504-508 (2019).
26. M. K. Beyer, H. Clausen-Schaumann, Mechanochemistry: The Mechanical Activation of Covalent Bonds. *Chem. Rev.* **105**, 2921–2948, (2005).
27. C. Yuan, S. Saito, C. Camacho, S. Irle, I. Hisaki, S. Yamaguchi, A  $\pi$ -conjugated System with Flexibility and Rigidity That Shows Environment-Dependent RGB Luminescence. *J. Am. Chem. Soc.* **135**, 8842–8845 (2013).
28. C. S. Wannere, D. Moran, N. L. Allinger, B. A. Hess, Jr., L. J. Schaad, P. v. R. Schleyer, On the Stability of Large  $[4n]$ Annulenes. *Org. Lett.* **5**, 2983–2986 (2003).
29. R. Kotani, H. Sotome, H. Okajima, S. Yokoyama, Y. Nakaike, A. Kashiwagi, C. Mori, Y. Nakada, S. Yamaguchi, A. Osuka, A. Sakamoto, H. Miyasaka, S. Saito, Flapping viscosity probe that shows polarity-independent ratiometric fluorescence. *J. Mater. Chem. C.* **5**, 5248–5256 (2017).
30. T. Yamakado, K. Otsubo, A. Osuka, S. Saito, Compression of a Flapping Mechanophore Accompanied by Thermal Void Collapse in a Crystalline Phase. *J. Am. Chem. Soc.* **140**, 6245–6248 (2018).
31. G. A. Filonenko, J. R. Khusnutdinova, Dynamic Phosphorescent Probe for Facile and Reversible Stress Sensing. *Adv. Mater.* 1700563 (2017).
32. Y. Sagara, M. Karman, E. Verde-Sesto, K. Matsuo, Y. Kim, N. Tamaoki, C. Weder, Rotaxanes as Mechanochromic Fluorescent Force Transducers in Polymers. *J. Am. Chem. Soc.* **140**, 1584–1587 (2018).

33. K. Straková, J. López-Andarias, N. Jiménez-Rojo, J. E. Chamber, S. J. Marciniak, H. Riezman, N. Sakai, S. Matile, HaloFlippers: A General Tool for the Fluorescence Imaging of Precisely Localized Membrane Tension Changes in Living Cells. *ACS Central Science* **6**, 1376-1385 (2020).
34. M. H. Lee, J. S. Kim, J. L. Sessler, Small molecule-based ratiometric fluorescence probes for cations, anions, and biomolecules. *Chem. Soc. Rev.* **44**, 4185–4191 (2015).
35. J. Gierschner, S. K. Behera, S. Y. Park, Dual Emission: Classes, Mechanism and Conditions. *Angew. Chem. Int. Ed. in press* DOI: 10.1002/anie.202009789 (2020).
36. C. Yuan, S. Saito, C. Camacho, T. Kowalczyk, S. Irle, S. Yamaguchi, Hybridization of a Flexible Cyclooctatetraene Core and Rigid Aceneimide Wings for Multiluminescent Flapping  $\pi$  Systems. *Chem. Eur. J.* **20**, 2193–2200 (2014).
37. K. Imato, T. Kanehara, T. Ohishi, M. Nishihara, H. Yajima, M. Ito, A. Takahara, H. Otsuka, Mechanochromic Dynamic Covalent Elastomers: Quantitative Stress Evaluation and Autonomous Recovery. *ACS Macro Lett.* **4**, 1307–1311 (2015).

**Acknowledgments:** We thank Dr Hiroya Abe and Dr Yuta Saito (Tohoku Univ.) for their help in the early stage of the preliminary study; **Funding:** JST, PRESTO, FRONTIER, Grant number JPMJPR16P6; MEXT/JSPS, KAKENHI, Grant Numbers JP18H01952, 20H04625, 19KK0357, 18H05482, and JP18J22477; Inoue foundation for science; **Author contributions:** H.Y. and S.S. conceived the concept. R.K., H.Y., and S.S. designed the experiments. R.K., S.Y., and S.N. performed the experiments. R.K. and S.S. conducted the quantum calculations. R.K. and S.S. analyzed the data. R.K. and S.S. wrote the manuscript, and S.Y., A.O., and H.Y. proofread it; **Competing interests:** Authors declare no competing interests; and **Data and materials availability:** All data is available in the main text or the supplementary materials.

### Supplementary Materials:

Materials and Methods

Figures S1-S68

Tables S1-S32

## Supplementary materials

### Materials and methods

#### Synthesis and purification

All reagents and solvents were of commercial grade and were used without further purification unless where noted. Tetrahydrofuran (THF) was dried using Glass Contour solvent purification system. Superdehydrated dimethylformamide (DMF) was purchased from Wako Chemicals. Polytetrahydrofutan ( $M_n \sim 650$ ) was dried under vacuum at 70 °C for 2 h before use. Thin layer chromatography (TLC) was performed by silica gel 60 F<sub>254</sub> (Merck). Column chromatography was performed using Wako gel C-300.

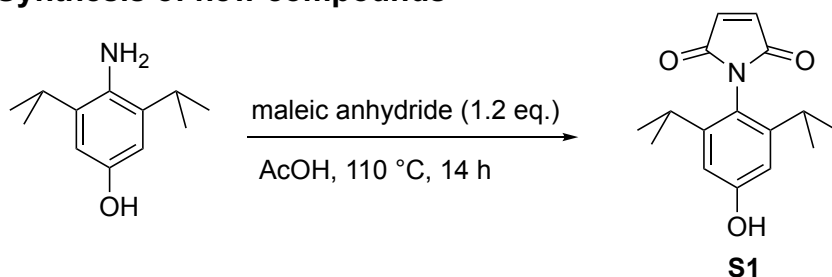
#### Measurements

<sup>1</sup>H and <sup>13</sup>C NMR spectra were recorded on a JEOL ECA-600 (600 MHz for <sup>1</sup>H and 151 MHz for <sup>13</sup>C NMR) spectrometer for **FLAP1**, **FLAP2**, compounds **4–11**, and compounds **S1–S4**. Chemical shifts were expressed as the  $\delta$  scale in ppm relative to internal standards CHCl<sub>3</sub> ( $\delta = 7.26$  ppm for <sup>1</sup>H and  $\delta = 77.16$  ppm for <sup>13</sup>C) and DMSO ( $\delta = 2.50$  ppm for <sup>1</sup>H and  $\delta = 39.52$  ppm for <sup>13</sup>C). High-resolution atmospheric-pressure-chemical-ionization time-of-flight mass-spectrometry (HR-APCI-TOF-MS) was recorded on a BRUKER micrOTOF model using positive mode. UV-visible absorption spectra were recorded on Shimadzu UV-3600 spectrometers. Fluorescence (FL) spectra were recorded on a JASCO Spectrofluorometer FP-8500. Absolute FL quantum yields were determined on a HAMAMATSU C9920-02S. FL lifetime was recorded on Hamamatsu Photonics QuantaTaurus-Tau C11367. Tensile tests were carried out using a SHIMADZU AUTOGRAPH AGS-X with a 1-kN load cell at crosshead. Differential scanning calorimetry (DSC) was recorded on a Hitachi High-Tech TA7000. Rheological measurements were conducted on an Anton Paar MCR702. Real-time FL measurements of PU specimens were performed using an Otsuka Electronics MALTI CHANNEL PHOTO DETECTOR MCPD-68000. Real-time FL measurements of PC specimens under microscope were performed using an AcroEdge small tensile testing machine OZ911, an EBAJAPAN hyperspectral camera NH-8 under an OLYMPUS inverted research microscope IX83 using OLYMPUS mercury lump U-HGLGPS. Cross-Nicol images and scales under microscope were obtained by a Leica DM2500 P optical microscope equipped with a Linkam LTS420E temperature-controlled microscope stage. Photographs and movies of specimens were taken using an OLYMPUS digital camera Tough TG-6.

#### Theoretical study

Theoretical calculations were performed using the Gaussian 16 program. (*SI*)

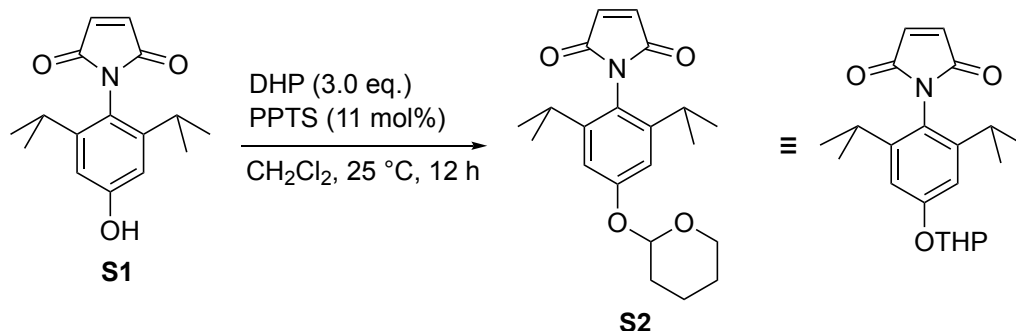
## Synthesis of new compounds



### 1-(4-Hydroxy-2,6-diisopropylphenyl)-1H-pyrrole-2,5-dione (**S1**)

Under Ar atmosphere, 4-amino-3,5-diisopropylphenol (*S2*) (2.77 g, 14.3 mmol) and maleic anhydride (1.68 g, 17.2 mmol) were added to a round-bottom flask (500 mL). After addition of AcOH (70 mL), the reaction vessel was allowed to stir at 110 °C for 14 h. The reaction mixture was diluted with EtOAc. The solution was poured into a separatory funnel, washed with saturated aqueous NaHCO<sub>3</sub> (3 times) and brine, dried over anhydrous Na<sub>2</sub>SO<sub>4</sub> and evaporated. The crude product was purified by silica gel column chromatography (eluent: CH<sub>2</sub>Cl<sub>2</sub>/EtOAc = 20:1). Recrystallization from *n*-hexane furnished **S1** as a white solid (3.08 g, 79%).

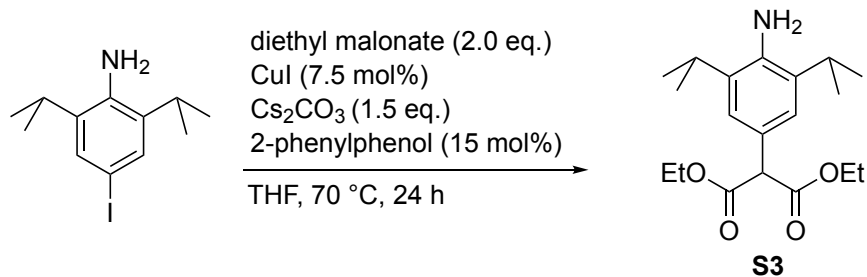
<sup>1</sup>H NMR (600 MHz, CDCl<sub>3</sub>)  $\delta$  (ppm) 6.87 (s, 2H), 6.69 (s, 2H), 4.80 (s, 1H), 2.56 (sept,  $J = 6.9$  Hz, 2H) and 1.13 (d,  $J = 6.9$  Hz, 12H); <sup>13</sup>C NMR (151 MHz, CDCl<sub>3</sub>)  $\delta$  (ppm) 170.99, 157.10, 149.54, 134.43, 118.95, 111.26, 29.50 and 23.95; HR-APCI TOF-MS ( $m/z$ ) found 273.1358, calcd for C<sub>16</sub>H<sub>19</sub>NO<sub>3</sub>: 273.1365 [ $M$ ]<sup>+</sup>.



**1-(2,6-Diisopropyl-4-((tetrahydro-2*H*-pyran-2-yl)oxy)phenyl)-1*H*-pyrrole-2,5-dione (S2)**

Under Ar atmosphere, **S1** (3.08 g, 11.3 mmol) and pyridinium *p*-toluenesulfonate (PPTS, 310 mg, 1.23 mmol) were added to a round-bottom flask (300 mL). After addition of CH<sub>2</sub>Cl<sub>2</sub> (85 mL) and 3,4-dihydro-2*H*-pyran (DHP, 2.87 mL, 33.4 mmol) at 0 °C, the reaction vessel was allowed to stir at 25 °C for 12 h. The reaction mixture was quenched with H<sub>2</sub>O and the solution was poured into a separatory funnel, washed with brine, dried over anhydrous Na<sub>2</sub>SO<sub>4</sub> and evaporated. Recrystallization from CH<sub>2</sub>Cl<sub>2</sub>/*n*-hexane furnished **S2** as a white solid (3.86 g, 96%).

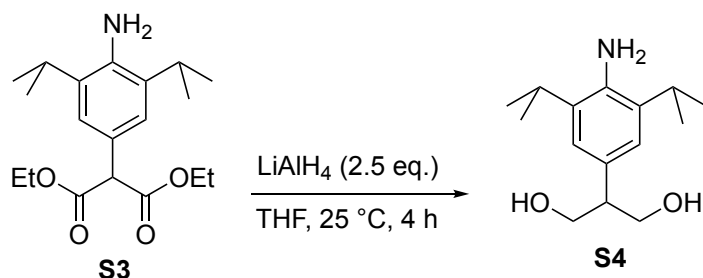
<sup>1</sup>H NMR (600 MHz, CDCl<sub>3</sub>) δ (ppm) 6.92 (s, 2H), 6.86 (s, 2H), 5.45 (m, 1H), 3.92 (m, 1H), 3.63 (m, 1H), 2.57 (sept, *J* = 6.9 Hz, 2H), 2.02 (m, 1H), 1.87 (m, 2H), 1.67–1.69 (m, 2H), 1.62–1.63 (m, 1H) and 1.13 (d, *J* = 6.9 Hz, 12H); <sup>13</sup>C NMR (151 MHz, CDCl<sub>3</sub>) δ (ppm) 170.94, 158.76, 148.89, 134.36, 119.52, 112.33, 96.34, 61.94, 30.49, 29.55, 25.36, 23.95 and 18.71; HR-APCI TOF-MS (*m/z*) found 357.1946, calcd for C<sub>21</sub>H<sub>27</sub>NO<sub>4</sub>: 357.1946 [*M*]<sup>-</sup>.



### Diethyl 2-(4-amino-3,5-diisopropylphenyl)malonate (**S3**)

Under Ar atmosphere, 4-iodo-2,6-diisopropylaniline (*S3*) (6.06 g, 20.0 mmol), CuI (285 mg, 1.50 mmol), Cs<sub>2</sub>CO<sub>3</sub> (9.78 g, 30.0 mmol) and 2-phenylphenol (510 mg, 3.00 mmol) were added to a round-bottom flask (100 mL). After addition of THF (20 mL) and diethyl malonate (6.10 mL, 40.0 mmol), the reaction vessel was allowed to stir at 70 °C for 24 h. The reaction mixture was quenched with H<sub>2</sub>O and diluted with EtOAc. The solution was poured into a separatory funnel, washed with brine, dried over anhydrous Na<sub>2</sub>SO<sub>4</sub> and evaporated. The crude product was purified by silica gel column chromatography (eluent: CH<sub>2</sub>Cl<sub>2</sub>) and **S3** was obtained as brown oil (4.00 g, 55%).

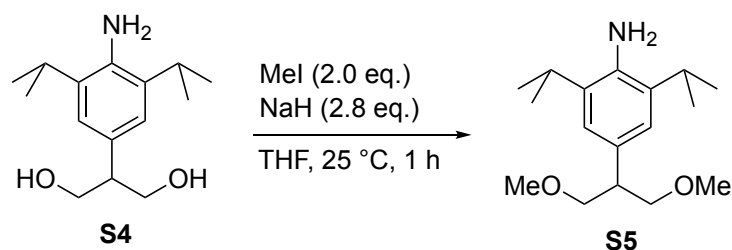
<sup>1</sup>H NMR (600 MHz, CDCl<sub>3</sub>) δ (ppm) 7.04 (s, 2H), 4.50 (s, 1H), 4.25–4.16 (m, 4H), 3.75 (s, 2H), 2.90 (sept, *J* = 6.9 Hz, 2H) and 1.28–1.25 (m, 18H); <sup>13</sup>C NMR (151 MHz, CDCl<sub>3</sub>) δ (ppm) 168.96, 140.43, 132.45, 124.04, 122.55, 61.61, 58.06, 28.16, 22.50 and 14.21; HR-APCI TOF-MS (*m/z*) found 336.2183, calcd for C<sub>19</sub>H<sub>30</sub>NO<sub>4</sub>: 336.2169 [*M*+H]<sup>+</sup>.



### 2-(4-Amino-3,5-diisopropylphenyl)propane-1,3-diol (**S4**)

Under Ar atmosphere, to the suspension of  $\text{LiAlH}_4$  (396 mg, 10.4 mmol) in THF (10 mL), a THF (10 mL) solution of **S3** (1.52 g, 4.18 mmol) was added at 0 °C. The mixture was allowed to stir at 25 °C for 4 h. The reaction mixture was quenched with sat.  $\text{Na}_2\text{SO}_4$  aq., filtered to remove aluminum salts, and washed with EtOAc (50 mL). The filtrate was purified by silica gel column chromatography (eluent: EtOAc). Recrystallization from  $\text{CH}_2\text{Cl}_2/n$ -hexane furnished **S4** as a white solid (910 mg, 87%).

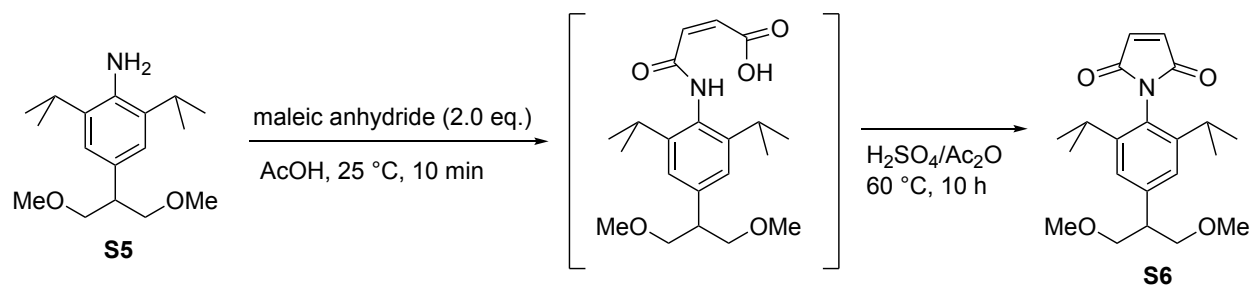
$^1\text{H}$  NMR (600 MHz,  $\text{CDCl}_3$ )  $\delta$  (ppm) 6.87 (s, 2H), 3.98–3.94 (m, 2H), 3.91–3.88 (m, 2H), 3.70 (s, 2H), 3.03 (tt,  $J = 7.8, 5.4$  Hz, 1H), 2.92 (sept,  $J = 6.6$  Hz, 2H), 1.92 (t,  $J = 5.4$  Hz, 2H) and 1.26 (d,  $J = 6.6$  Hz, 12H);  $^{13}\text{C}$  NMR (151 MHz,  $\text{CDCl}_3$ )  $\delta$  (ppm) 139.44, 132.97, 128.69, 122.43, 66.55, 49.75, 28.09 and 22.52; HR-APCI TOF-MS ( $m/z$ ) found 252.1968, calcd for  $\text{C}_{15}\text{H}_{26}\text{NO}_2$ : 252.1958  $[M+\text{H}]^+$ .



#### 4-(1,3-Dimethoxypropan-2-yl)-2,6-diisopropylaniline (S5)

Under Ar atmosphere, to the suspension of NaH (60% dispersion in paraffin liquid, 401 mg, 10.0 mmol) and MeI (445  $\mu\text{L}$ , 7.16 mmol) in THF (9.0 mL), a THF (4.5 mL) solution of **S4** (900 mg, 3.58 mmol) was added at 0  $^\circ\text{C}$ . The mixture was allowed to stir at 25  $^\circ\text{C}$  for 1 h. The reaction mixture was dilute with EtOAc (20 mL) and evaporated. The crude product was purified by silica gel column chromatography (eluent:  $\text{CH}_2\text{Cl}_2$ :*n*-hexane:EtO<sub>2</sub>=1:1:1) to furnish **S5** as brown oil (932 mg, 93%).

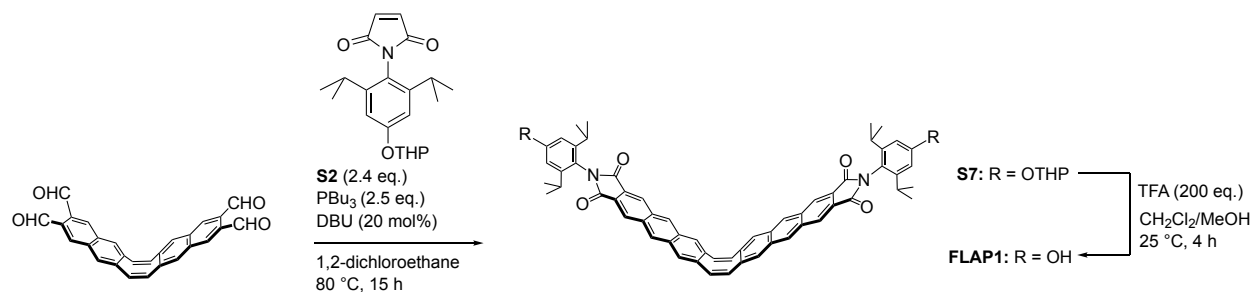
<sup>1</sup>H NMR (600 MHz, CDCl<sub>3</sub>)  $\delta$  (ppm) 6.92 (s, 2H), 3.63 (dd,  $J = 9.2, 6.8$  Hz, 2H), 3.57 (dd,  $J = 9.7, 6.4$  Hz, 2H), 3.39 (s, 6H), 3.06 (tt,  $J = 9.2, 6.4$  Hz, 1H), 2.91 (sept,  $J = 6.9$  Hz, 2H), and 1.27 (d,  $J = 6.9$  Hz, 12H); <sup>13</sup>C NMR (151 MHz, CDCl<sub>3</sub>)  $\delta$  (ppm) 139.12, 132.45, 130.54, 122.43, 74.79, 58.99, 45.84, 28.13 and 22.56; HR-APCI TOF-MS ( $m/z$ ) found 280.2271, calcd for C<sub>17</sub>H<sub>30</sub>NO<sub>2</sub>: 280.2271 [ $M+H$ ]<sup>+</sup>.



### 1-(4-(1,3-Dimethoxypropan-2-yl)-2,6-diisopropylphenyl)-1*H*-pyrrole-2,5-dione (**S6**)

Under Ar atmosphere, **S5** (1.03 g, 3.69 mmol) and maleic anhydride (723 mg, 7.37 mmol) were added to a Schlenk flask (20 mL). After addition of AcOH (2.21 mL), the reaction vessel was allowed to stir at room temperature for 10 min. Then H<sub>2</sub>SO<sub>4</sub> (95%, 369  $\mu$ L) and acetic anhydride (184  $\mu$ L) were added to the reaction mixture and the reaction vessel was allowed to warm at 60 °C for 10 h. The reaction mixture was quenched with H<sub>2</sub>O and diluted with EtOAc. The solution was poured into a separatory funnel, washed with brine, dried over anhydrous Na<sub>2</sub>SO<sub>4</sub> and evaporated. The crude product was purified by silica gel column chromatography (eluent: CH<sub>2</sub>Cl<sub>2</sub>/Et<sub>2</sub>O =6:1) and **S6** was obtained as a white solid (1.06 g, 80%).

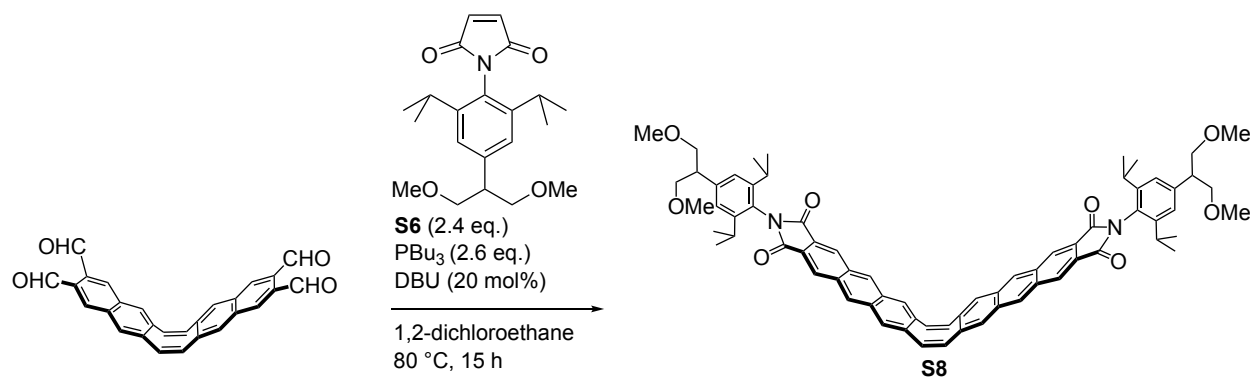
<sup>1</sup>H NMR (600 MHz, CDCl<sub>3</sub>)  $\delta$  (ppm) 7.12 (s, 2H), 6.88 (s, 2H), 3.67–3.64 (m, 2H), 3.63–3.60 (m, 2H), 3.35 (s, 6H), 3.13 (tt,  $J$ =7.2, 6.0 Hz, 1H), 2.59 (sept,  $J$ =6.9 Hz, 2H) and 1.15 (d,  $J$ =6.9 Hz, 12H); <sup>13</sup>C NMR (151 MHz, CDCl<sub>3</sub>)  $\delta$  (ppm) 170.84, 147.24, 142.95, 134.43, 124.79, 123.94, 74.04, 59.09, 46.37, 29.45, and 24.09; HR-APCI TOF-MS ( $m/z$ ) found 359.2096, calcd for C<sub>21</sub>H<sub>30</sub>NO<sub>4</sub>: 359.2091 [ $M$ ]<sup>+</sup>.



## FLAP1

Under Ar atmosphere, **S2** (559 mg, 1.56 mmol) and 1,2-dichloroethane (12 mL) were added to a round-bottom flask (20 mL). After addition of tributylphosphine (410  $\mu\text{L}$ , 1.66 mmol) at  $0\text{ }^\circ\text{C}$ , the reaction vessel was allowed to stir at room temperature for 30 min. Then a 1,2-dichloroethane (10 mL) solution of tetraformyl dinaphthocyclooctatetraene (*x*) (271 mg, 0.651 mmol) was added to the reaction mixture at  $0\text{ }^\circ\text{C}$ , followed by addition of DBU (19.5  $\mu\text{L}$ , 0.130 mmol). The reaction vessel was allowed to stir at  $80\text{ }^\circ\text{C}$  for 15 h. The reaction mixture was quenched with  $\text{H}_2\text{O}$  and poured into a separatory funnel, washed with brine, dried over anhydrous  $\text{Na}_2\text{SO}_4$  and evaporated. The crude product was purified by silica gel column chromatography (eluent:  $\text{CH}_2\text{Cl}_2/\text{AcOEt}$  =20:1) and **S7** was obtained as a yellow solid (138 mg, 20%), which was used for the subsequent reaction. **S7** was added to a round-bottom flask (100 mL). After addition of  $\text{CH}_2\text{Cl}_2$  (30 mL), MeOH (10 mL), and TFA (2.0 mL, 26 mmol), the reaction vessel was allowed to stir at  $25\text{ }^\circ\text{C}$  for 4 h. The reaction mixture was quenched with  $\text{H}_2\text{O}$  and poured into a separatory funnel, washed with brine, dried over anhydrous  $\text{Na}_2\text{SO}_4$  and evaporated. The crude product was purified by silica gel column chromatography (eluent:  $\text{CH}_2\text{Cl}_2/\text{EtOAc}$ =20:1). Recrystallization from  $\text{CH}_2\text{Cl}_2/n$ -hexane furnished **FLAP1** as a yellow solid (107 mg, 92% from **S7**).

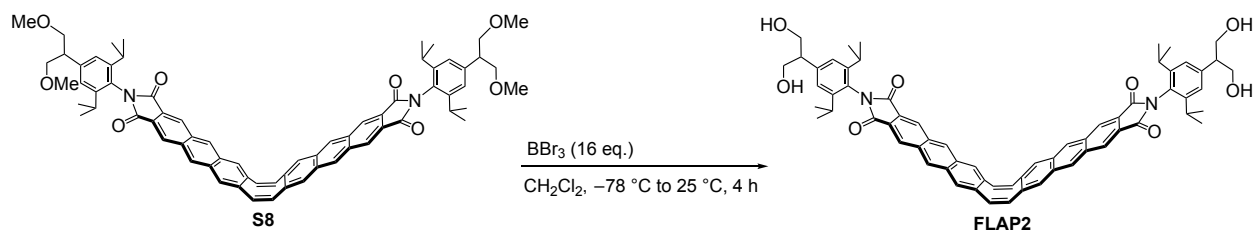
$^1\text{H}$  NMR (600 MHz,  $\text{CDCl}_3$ )  $\delta$  (ppm) 8.55 (m, 8H), 7.94 (s, 4H), 7.24 (s, 4H), 6.75 (s, 4H), 4.90 (s, 2H), 2.70 (sept,  $J = 6.9$  Hz, 4H) and 1.14 (d,  $J = 6.9$  Hz, 24H);  $^{13}\text{C}$  NMR (151 MHz,  $\text{DMSO-}d_6$ )  $\delta$  (ppm) 167.47, 158.59, 147.92, 136.12, 133.09, 131.88, 131.44, 129.93, 128.34, 126.56, 125.73, 118.40, 110.50, 28.65 and 23.56; HR-MALDI TOF-MS ( $m/z$ ) found 895.33, calcd for  $\text{C}_{60}\text{H}_{51}\text{N}_2\text{O}_6$ : 895.37 [ $M+\text{H}$ ] $^+$ . UV/Vis absorption ( $\text{CH}_2\text{Cl}_2$ ):  $\lambda_{\text{max}}$  ( $\epsilon/\text{M}^{-1}\text{ cm}^{-1}$ ) = 332 nm ( $9.28 \times 10^4$ ); fluorescence ( $\text{CH}_2\text{Cl}_2$ ,  $\lambda_{\text{ex}} = 340$  nm):  $\lambda_{\text{max}} = 523, 564,$  and  $610$  nm,  $\Phi_{\text{FL}} = 0.26$ .



### FLAP-4OMe S8

Under Ar atmosphere, **S6** (682 mg, 1.90 mmol) and 1,2-dichloroethane (30 mL) were added to a round-bottom flask (200 mL). After addition of tributylphosphine (507  $\mu\text{L}$ , 2.05 mmol) at  $0\text{ }^\circ\text{C}$ , the reaction vessel was allowed to stir at room temperature for 30 min. Then a 1,2-dichloroethane (15 mL) solution of tetraformyl dinaphthocyclooctatetraene (329 mg, 0.79 mmol) was added to the reaction mixture at  $0\text{ }^\circ\text{C}$ , followed by addition of DBU (24  $\mu\text{L}$ , 0.16 mmol). The reaction vessel was allowed to stir at  $80\text{ }^\circ\text{C}$  for 12 h. The reaction mixture was quenched with  $\text{H}_2\text{O}$  and poured into a separatory funnel, washed with brine, dried over anhydrous  $\text{Na}_2\text{SO}_4$  and evaporated. The crude product was purified by silica gel column chromatography (eluent:  $\text{CH}_2\text{Cl}_2/\text{Et}_2\text{O}=5:1$ ) and **S8** was obtained as a yellow solid (208 mg, 25%).

$^1\text{H}$  NMR (600 MHz,  $\text{CDCl}_3$ )  $\delta$  (ppm) 8.55 (s, 4H+4H), 7.94 (s, 4H), 7.24 (s, 4H), 7.17 (s, 4H), 3.69–3.62 (m, 8H), 3.37 (s, 12H), 3.16 (tt,  $J=7.2, 6.0$  Hz, 2H), 2.72 (sept,  $J=6.8$  Hz, 4H) and 1.15 (d,  $J=6.8$  Hz, 24H);  $^{13}\text{C}$  NMR (151 MHz,  $\text{CDCl}_3$ )  $\delta$  (ppm) 167.88, 146.68, 142.80, 136.63, 133.36, 132.39, 132.20, 129.84, 128.49, 126.64, 125.92, 123.88, 123.56, 74.16, 59.07, 46.37, 29.48, and 24.12; HR-MALDI TOF-MS ( $m/z$ ) found 1089.53, calcd for  $\text{C}_{70}\text{H}_{70}\text{N}_2\text{O}_8\text{Na}$ : 1089.50 [ $M+\text{Na}$ ] $^+$ .



## FLAP2

Under Ar atmosphere, **S8** (9.8 mg, 9.2  $\mu\text{mol}$ ) and  $\text{CH}_2\text{Cl}_2$  (0.7 mL) were added to a Schlenk flask (20 mL). After addition of  $\text{CH}_2\text{Cl}_2$  solution of  $\text{BBr}_3$  (1.0 M, 147  $\mu\text{L}$ ) at  $-78\text{ }^\circ\text{C}$ , the reaction vessel was allowed to stir and warm to  $25\text{ }^\circ\text{C}$  over 4 h. The reaction mixture was quenched with  $\text{H}_2\text{O}$  and poured into a separatory funnel, washed with brine, dried over anhydrous  $\text{Na}_2\text{SO}_4$  and evaporated. The crude product was purified by silica gel column chromatography (eluent: EtOAc) and **FLAP2** was obtained as a yellow solid (6.7 mg, 72%).

$^1\text{H}$  NMR (600 MHz,  $\text{CDCl}_3$ )  $\delta$  (ppm) 8.56 (s, 4H), 8.55 (s, 4H), 7.94 (s, 4H), 7.24 (s, 4H), 7.14 (s, 4H), 4.05–4.00 (m, 8H), 3.18–3.14 (m, 2H), 2.74 (sept,  $J = 6.8$  Hz, 4H), 2.01 (t,  $J = 6.0$  Hz, 4H) and 1.16 (d,  $J = 6.8$  Hz, 24H);  $^{13}\text{C}$  NMR (151 MHz,  $\text{DMSO}-d_6$ )  $\delta$  (ppm) 167.30, 145.81, 143.99, 136.18, 133.13, 131.89, 131.47, 129.99, 128.37, 126.76, 125.69, 125.42, 123.63, 62.64, 50.82, 28.70, and 23.67; HR-MALDI TOF-MS ( $m/z$ ) found 1033.42, calcd for  $\text{C}_{66}\text{H}_{62}\text{N}_2\text{O}_8\text{Na}$ : 1033.44  $[\text{M}+\text{Na}]^+$ .  $\lambda_{\text{max}}$  ( $\epsilon / \text{M}^{-1} \text{ cm}^{-1}$ ) = 331 nm ( $9.37 \times 10^4$ ); fluorescence ( $\text{CH}_2\text{Cl}_2$ ,  $\lambda_{\text{ex}} = 340$  nm):  $\lambda_{\text{max}} = 524, 565, \text{ and } 610$  nm,  $\Phi_{\text{FL}} = 0.32$ .

## Photophysical properties of parent FLAP

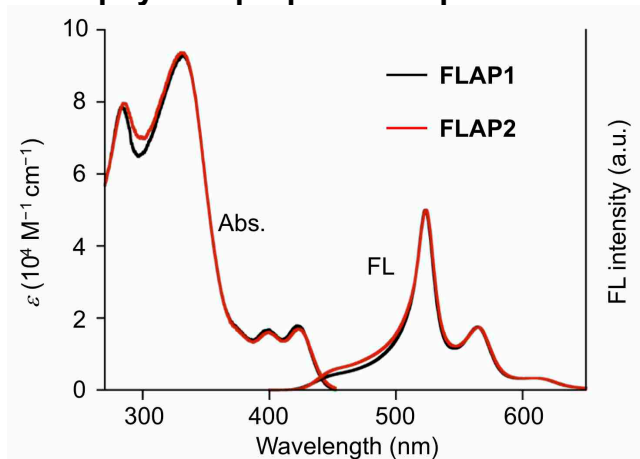


**Fig. S1.** UV/visible absorption (Abs) and FL spectra of **FLAP1** and **FLAP2** in  $\text{CH}_2\text{Cl}_2$ .

**Table S1.** Photophysical constants of **FLAP1** and **FLAP2** in  $\text{CH}_2\text{Cl}_2$ .  $\lambda_{\text{ex}} = 365 \text{ nm}$ .

	$\Phi_{\text{FL}}$	$\tau_{\text{FL}} \text{ (ns)}^{\text{a}}$	$k_{\text{r}} \text{ (s}^{-1}\text{)}^{\text{b}}$	$k_{\text{nr}} \text{ (s}^{-1}\text{)}^{\text{c}}$
<b>FLAP1</b>	0.26	11.0	$2.4 \times 10^7$	$6.7 \times 10^7$
<b>FLAP2</b>	0.32	10.6	$3.0 \times 10^7$	$6.4 \times 10^7$

<sup>a</sup> FL lifetime.  $\lambda_{\text{em}} = 525 \text{ nm}$ . <sup>b</sup> Radiative decay constant. <sup>c</sup> Non-radiative decay constant.  $k_{\text{r}}$  and  $k_{\text{nr}}$  were calculated from the equations below.

$$\Phi_{\text{FL}} = k_{\text{r}} / k_{\text{r}} + k_{\text{nr}}$$

$$\tau_{\text{FL}} = 1 / k_{\text{r}} + k_{\text{nr}}$$

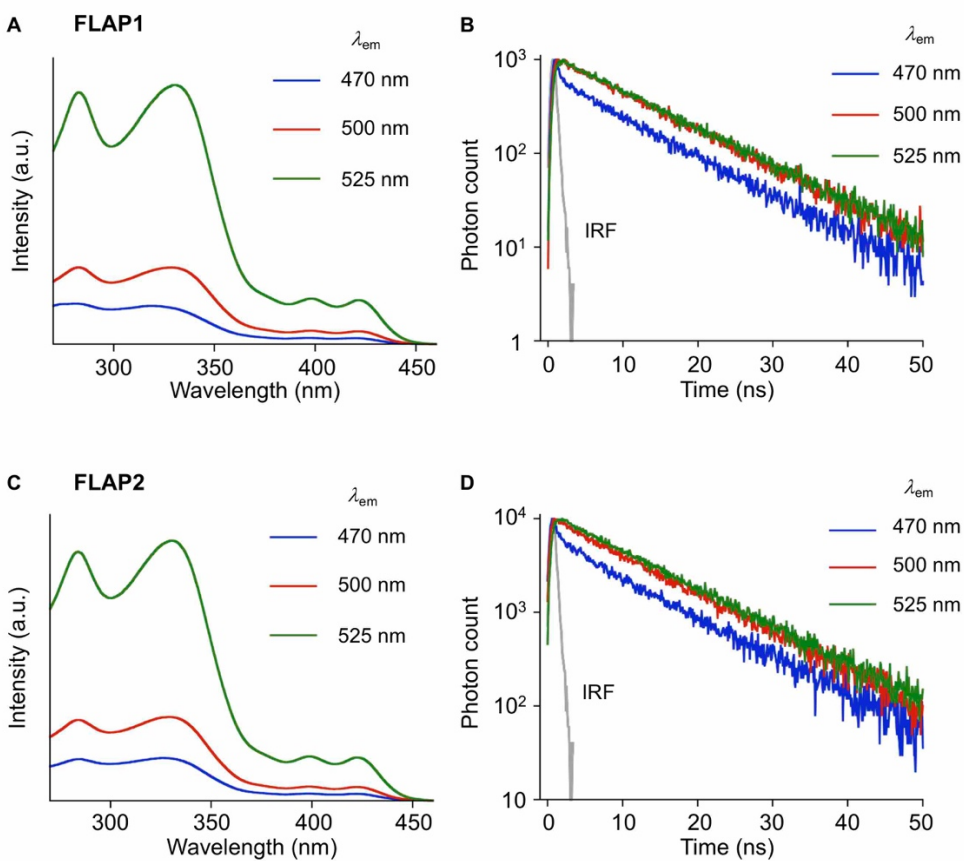


**Fig. S2.** (A) Excitation spectra and (B) FL decay profiles of **FLAP1**, and (C) excitation spectra and (D) FL decay profiles of **FLAP2** in  $\text{CH}_2\text{Cl}_2$ . Concentration: *ca.*  $10^{-6}$  M.

**Table S2.** Photophysical constants of **FLAP1** and **FLAP2** in  $\text{CH}_2\text{Cl}_2$ .  $\lambda_{\text{ex}} = 365$  nm.

	$\lambda_{\text{em}}$ (nm)	$\chi^2$	$\tau_{\text{FL}}$ (ns) <sup>a</sup>	$\tau_1$ (ns)	$\tau_2$ (ns)	$A_1$	$A_2$
<b>FLAP1</b>	470	1.06	9.0	0.2	9.9	320	66
	500	1.16	10.6	0.3	10.8	88	110
	525	1.03	11.0				
<b>FLAP2</b>	470	1.25	8.9	0.2	9.8	270	66
	500	1.07	10.4	0.3	10.7	94	104
	525	1.05	10.6				

<sup>a</sup> Mean FL lifetime calculated from the equation below.

$$\tau_{\text{FL}} = \frac{\tau_1^2 A_1 + \tau_2^2 A_2}{\tau_1 A_1 + \tau_2 A_2}$$

, where  $A_1$  and  $A_2$  was determined by analysis of the fitting equation below.

$$G(t) = A_1 \exp\left(-\frac{t}{\tau_1}\right) + A_2 \exp\left(-\frac{t}{\tau_2}\right)$$

, where  $G(t)$  was photon count as a function of time.

## Computational studies of monomer FLAP

Density functional theory (DFT) calculations of the isolated molecules were performed using the Gaussian 16 program (*x*). The appropriate density functional (PBE0) was selected because of reproducibility of the absorption spectrum of the FLAP series (*x*). All optimized structures gave no imaginary frequencies. In the Fig. S4–12, compositions (%) and oscillator strength  $f$  were calculated based on the respective optimized structure. H and L stand for HOMO and LUMO, respectively. Here and elsewhere, compositions were calculated by taking the square of the dominant configuration and multiplying the result by two, in order to account for excitations involving  $\alpha$  and  $\beta$  spin orbitals.

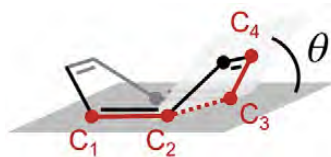


**Fig. S3.** Definition of a bending angle  $\theta$  used in the computational studies.  $\theta$  was calculated by two planes based on the  $C_1$ – $C_2$ – $C_3$  plane and the  $C_2$ – $C_3$ – $C_4$  plane.

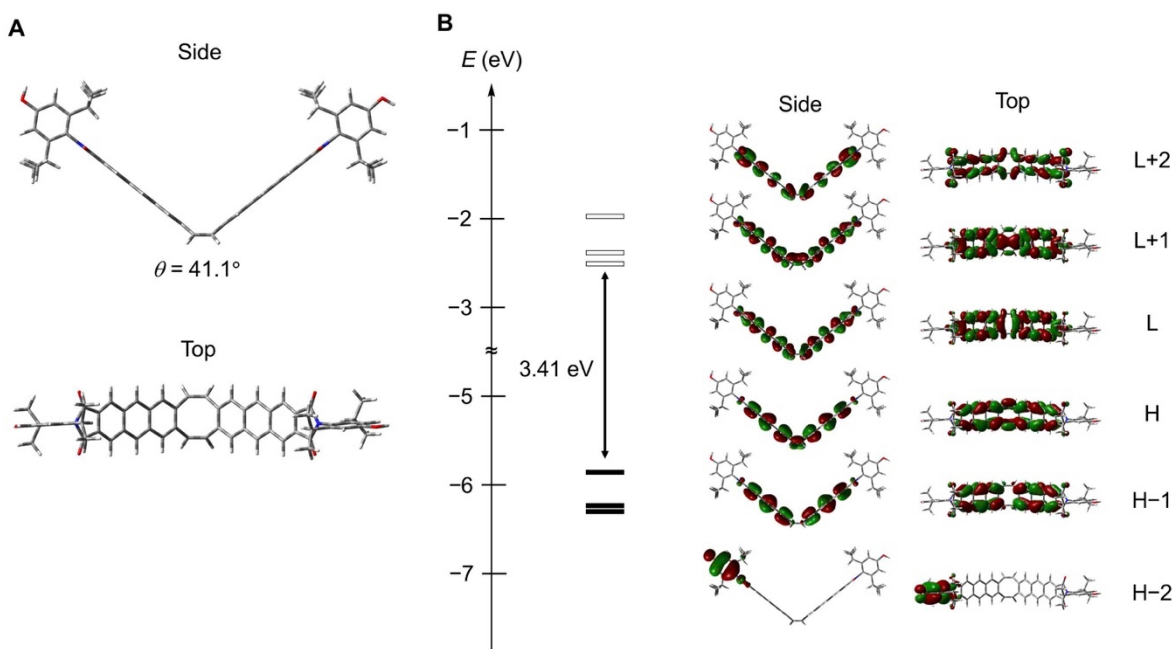


**Fig. S4.** (a) Optimized structures and (b) energy diagrams and MOs of **FLAP1** in the  $S_0$  optimized geometry at the PBE0/6-31+G(d) level.

**Table S3.** Summary of excitation energies, configurations and oscillator strengths of the  $S_0 \rightarrow S_n$  ( $n \leq 3$ ) transitions for  $S_0$  optimized **FLAP1** at the TD PBE0/6-31+G(d) level.

Transition	Excitation energy	Configuration(s)	Oscillator strength
$S_0 \rightarrow S_1$	2.89 eV (429 nm)	H $\rightarrow$ L (96%)	0.0000
$S_0 \rightarrow S_2$	2.99 eV (415 nm)	H-1 $\rightarrow$ L (7%) H $\rightarrow$ L+1 (93%)	0.0385
$S_0 \rightarrow S_3$	3.19 eV (389 nm)	H-7 $\rightarrow$ L+1 (4%) H-6 $\rightarrow$ L (16%) H-1 $\rightarrow$ L+3 (8%) H $\rightarrow$ L+2 (68%)	0.2660

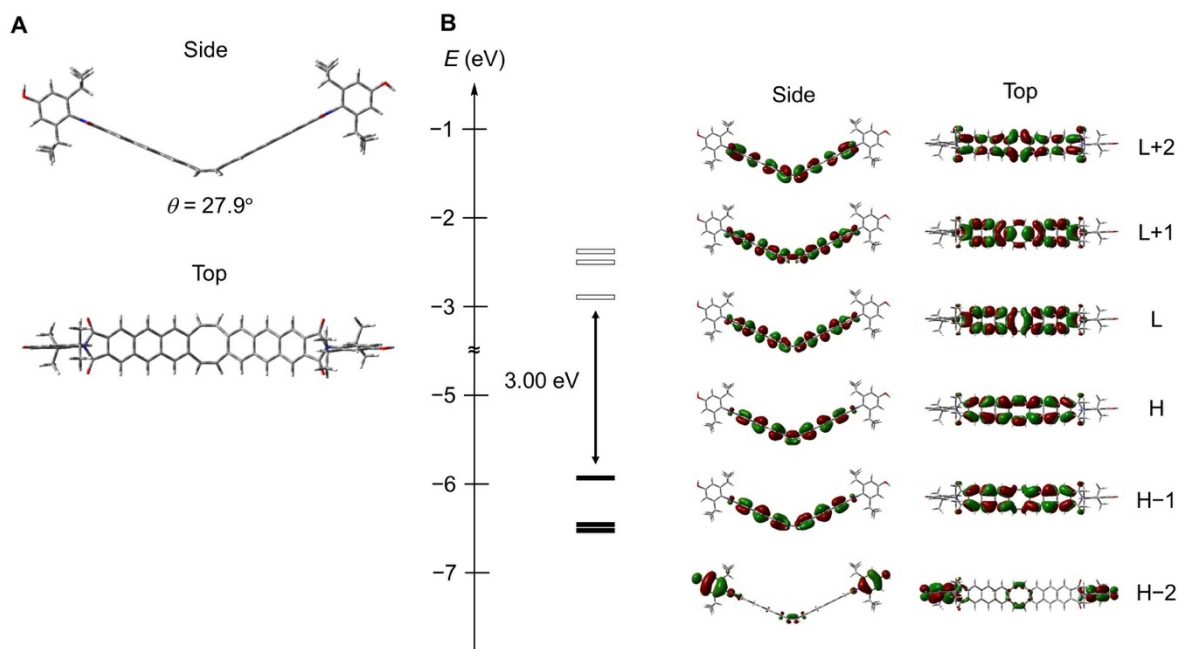


**Fig. S5.** (A) Optimized structures and (B) energy diagrams and MOs of **FLAP1** in the  $S_1$  optimized shallow V-shaped geometry at the TD PBE0/6-31G+(d) level.

**Table S4.** Summary of excitation energy, configuration and oscillator strength of the  $S_0 \rightarrow S_1$  transition for shallow V-shaped  $S_1$  optimized **FLAP1** at the TD PBE0/6-31+G(d) level.

Transition	Excitation energy	Configuration	Oscillator strength
$S_0 \rightarrow S_1$	2.52 eV (492 nm)	H $\rightarrow$ L (98%)	0.0000

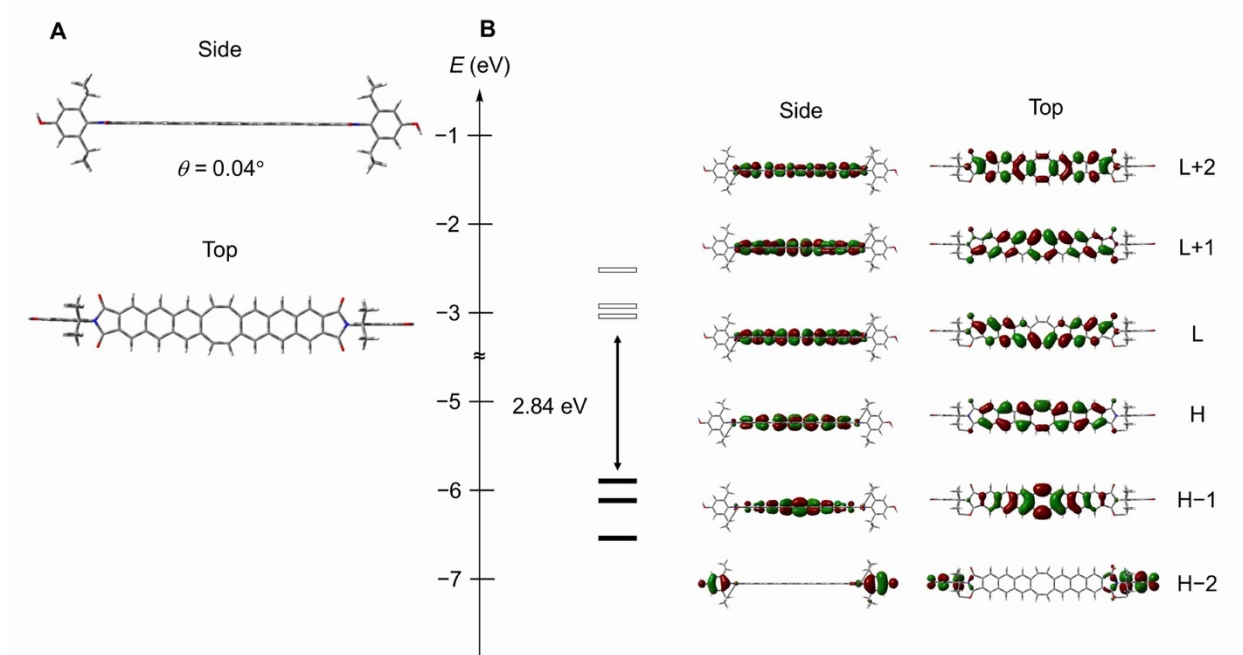


**Fig. S6.** (A) Optimized structures and (B) energy diagrams and MOs of **FLAP1** in the  $S_1$  optimized planar geometry at the TD PBE0/6-31G+(d) level.

**Table S5.** Summary of excitation energy, configurations and oscillator strength of the  $S_0 \rightarrow S_1$  transition for planar  $S_1$  optimized **FLAP1** at the TD PBE0/6-31+G(d) level.

Transition	Excitation energy	Configurations	Oscillator strength
$S_0 \rightarrow S_1$	2.21 eV (561 nm)	H-1 $\rightarrow$ L (35%) H $\rightarrow$ L (44%) H $\rightarrow$ L+1 (19%)	0.0731

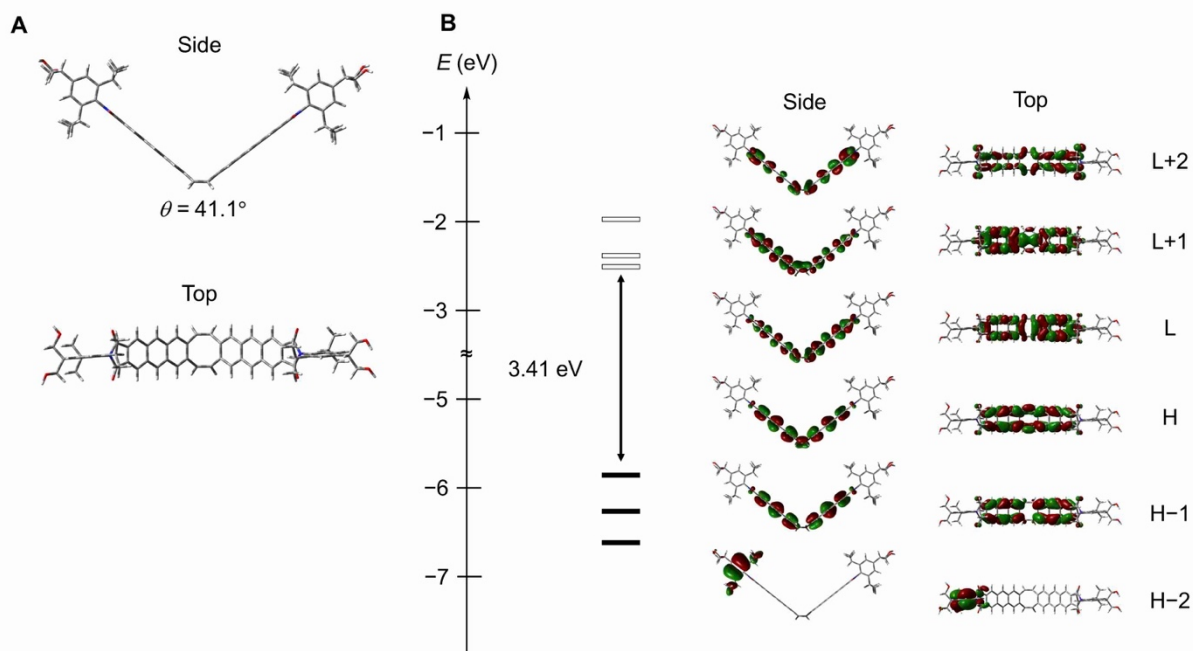


**Fig. S7.** (A) Optimized structures and (B) energy diagrams and MOs of **FLAP2** in  $S_0$  optimized geometry at the PBE0/6-31+G(d) level.

**Table S6.** Summary of excitation energies, configurations and oscillator strengths of the  $S_0 \rightarrow S_n$  ( $n \leq 3$ ) transitions for  $S_0$  optimized **FLAP2** at the TD PBE0/6-31+G(d) level.

Transition	Excitation energy	Configuration(s)	Oscillator strength
$S_0 \rightarrow S_1$	2.89 eV (429 nm)	H $\rightarrow$ L (96%)	0.0000
$S_0 \rightarrow S_2$	2.99 eV (415 nm)	H-1 $\rightarrow$ L (7%) H $\rightarrow$ L+1 (92%)	0.0387
$S_0 \rightarrow S_3$	3.19 eV (389 nm)	H-7 $\rightarrow$ L+1 (4%) H-6 $\rightarrow$ L (13%) H-1 $\rightarrow$ L+3 (8%) H $\rightarrow$ L+2 (69%)	0.2882

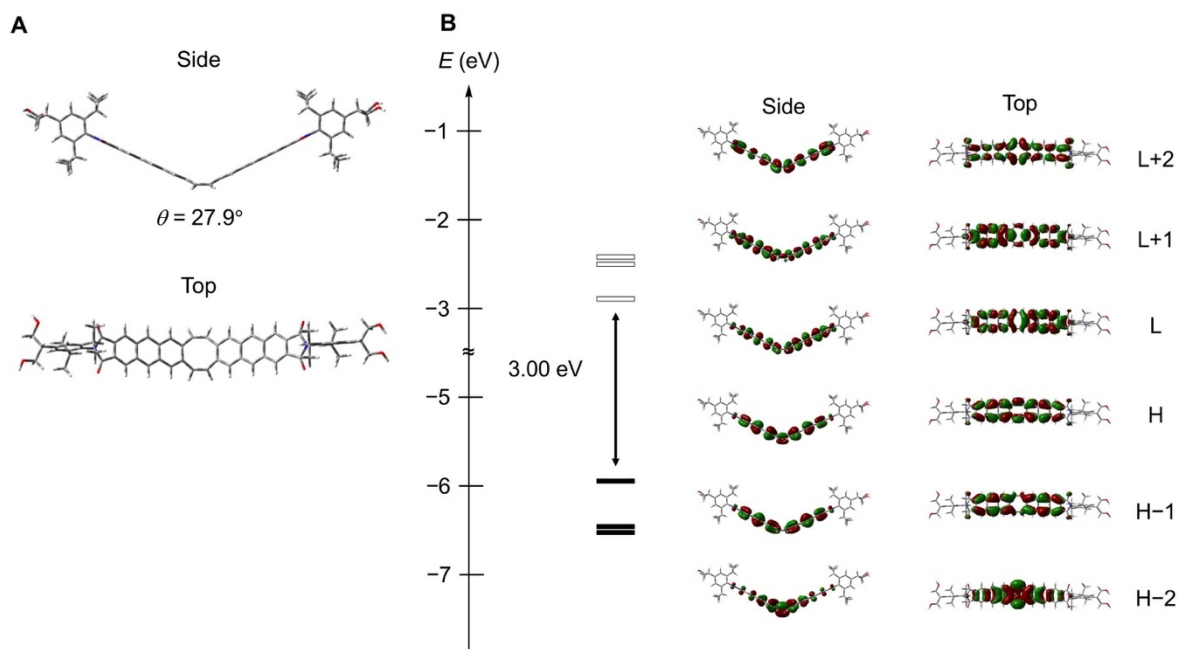


**Fig. S8.** (A) Optimized structures and (B) energy diagrams and MOs of **FLAP2** in the  $S_1$  optimized shallow V-shaped geometry at the TD PBE0/6-31G+(d) level.

**Table S7.** Summary of excitation energy, configuration and oscillator strength of the  $S_0 \rightarrow S_1$  transition for shallow V-shaped  $S_1$  optimized **FLAP2** at the TD PBE0/6-31+G(d) level.

Transition	Excitation energy	Configuration	Oscillator strength
$S_0 \rightarrow S_1$	2.52 eV (492 nm)	H $\rightarrow$ L (98%)	0.0005

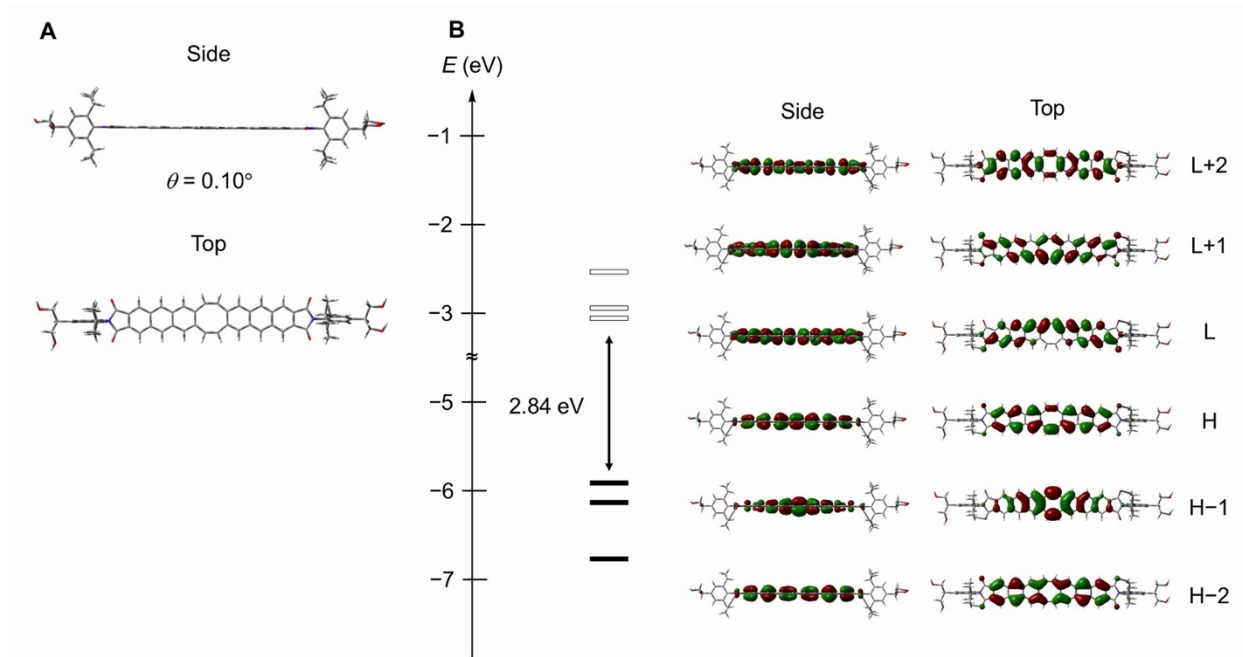


**Fig. S9.** (A) Optimized structures and (B) energy diagrams and MOs of **FLAP2** in the  $S_1$  optimized planar geometry at the TD PBE0/6-31G+(d) level.

**Table S8.** Summary of excitation energy, configurations and oscillator strength of the  $S_0 \rightarrow S_1$  transition for planar  $S_1$  optimized **FLAP2** at the TD PBE0/6-31+G(d) level.

Transition	Excitation energy	Configurations	Oscillator strength
$S_0 \rightarrow S_1$	2.21 eV (561 nm)	H-1 $\rightarrow$ L (35%) H $\rightarrow$ L (44%) H $\rightarrow$ L+1 (19%)	0.0749

Calculations performed at the CAM-B3LYP/6-31+G(d) level of theory

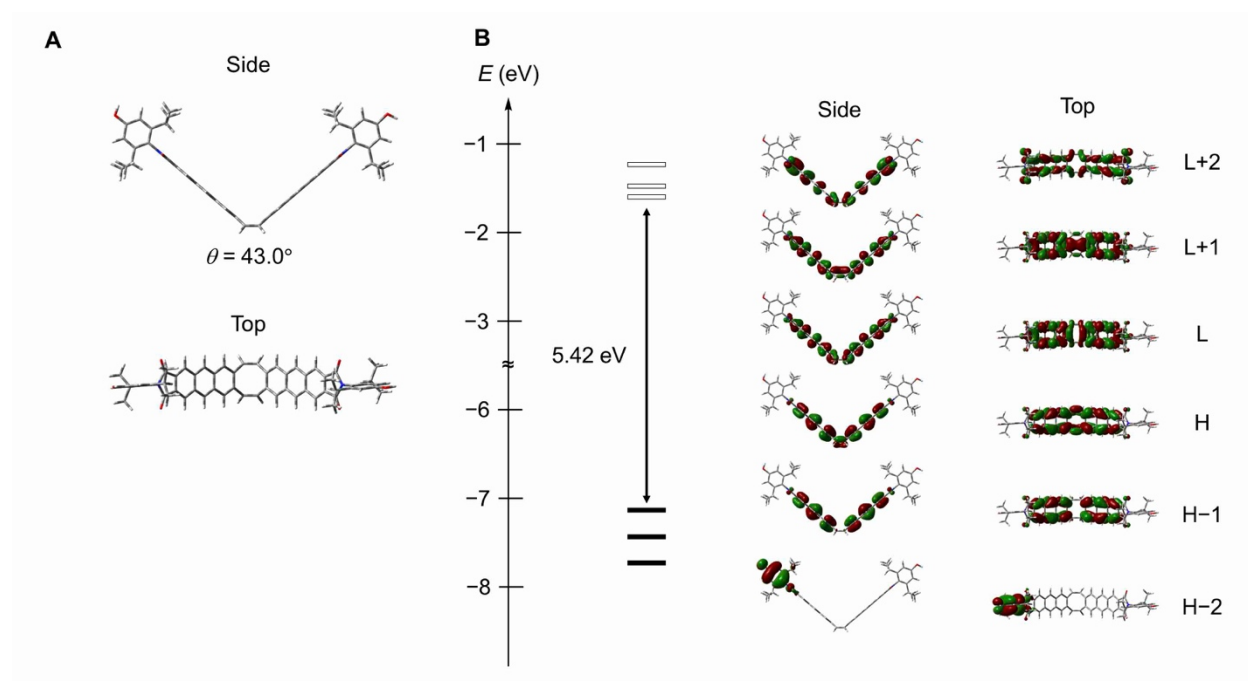


**Fig. S10.** (a) Optimized structures and (b) energy diagrams and MOs of **FLAP1** in the  $S_0$  optimized geometry at the CAM-B3LYP/6-31+G(d) level.

**Table S9.** Summary of excitation energies, configurations and oscillator strengths of the  $S_0 \rightarrow S_n$  ( $n \leq 3$ ) transitions for  $S_0$  optimized **FLAP1** at the TD CAM-B3LYP/6-31+G(d) level.

Transition	Excitation energy	Configurations	Oscillator strength
$S_0 \rightarrow S_1$	3.38 eV (367 nm)	H-1 $\rightarrow$ L+1 (33%) H $\rightarrow$ L (63%)	0.0000
$S_0 \rightarrow S_2$	3.40 eV (365 nm)	H-1 $\rightarrow$ L (40%) H $\rightarrow$ L+1 (57%)	0.0847
$S_0 \rightarrow S_3$	3.65 eV (340 nm)	H-7 $\rightarrow$ L+1 (11%) H-5 $\rightarrow$ L (15%) H-1 $\rightarrow$ L+3 (22%) H $\rightarrow$ L+2 (43%)	0.2185

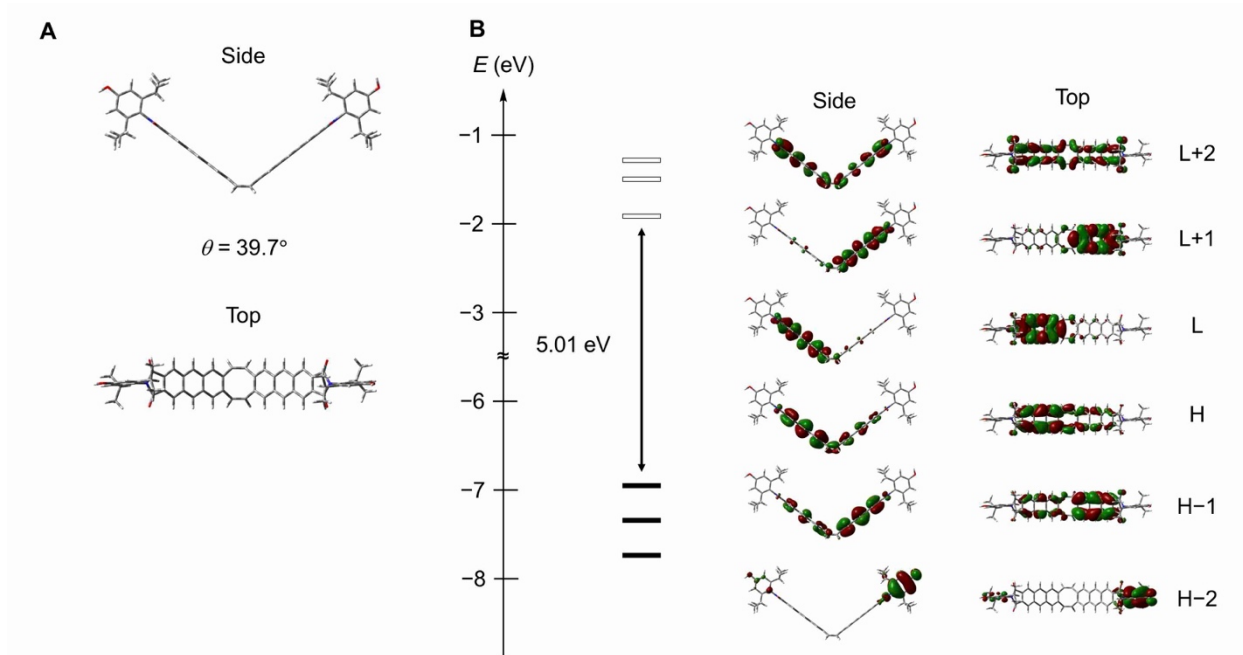


**Fig. S11.** (A) Optimized structures and (B) energy diagrams and MOs of **FLAP1** in the  $S_1$  optimized shallow V-shaped geometry, at the TD CAM-B3LYP/6-31G+(d) level.

**Table S10.** Summary of excitation energy, configurations and oscillator strength of the  $S_0 \rightarrow S_1$  transition for shallow V-shaped  $S_1$  optimized **FLAP1** at the TD CAM-B3LYP/6-31+G(d) level.

Transition	Excitation energy	Configurations	Oscillator strength
$S_0 \rightarrow S_1$	2.90 eV (428 nm)	H-1 $\rightarrow$ L (8%) H $\rightarrow$ L (88%)	0.0423

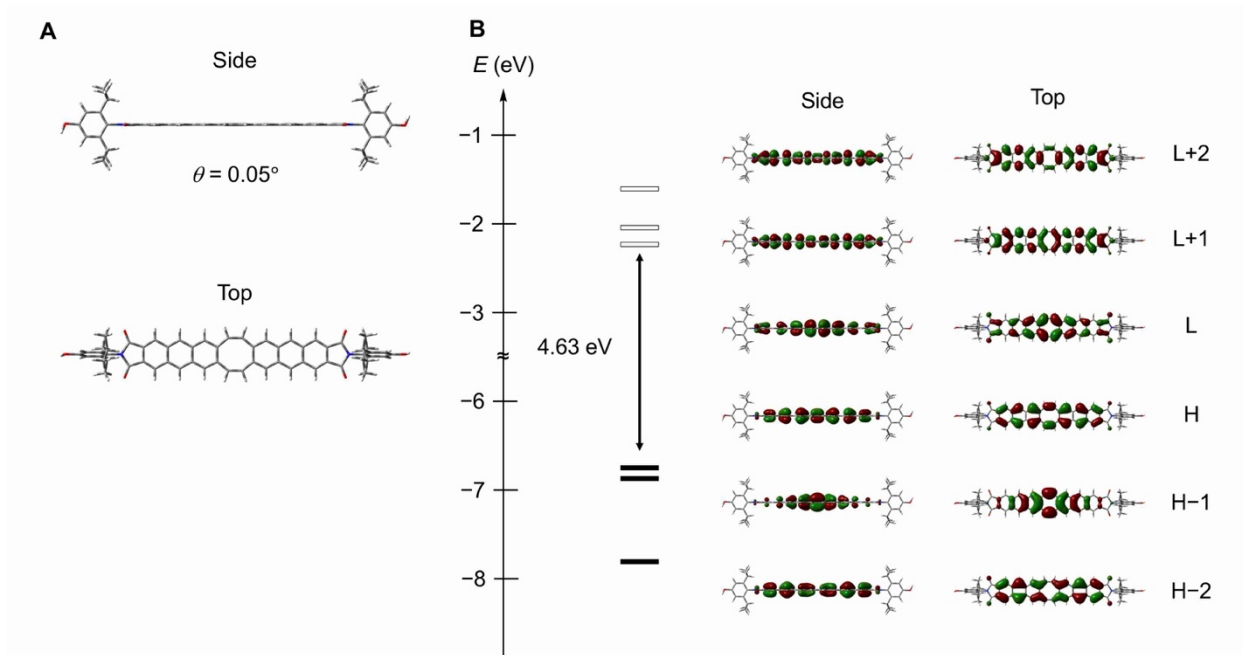


**Fig. S12.** (A) Optimized structures and (B) energy diagrams and MOs of **FLAP1** in the  $S_1$  optimized planar geometry at the TD CAM-B3LYP/6-31G+(d) level.

**Table S11.** Summary of excitation energy, configuration and oscillator strength of the  $S_0 \rightarrow S_1$  transition for planar  $S_1$  optimized **FLAP1** at the TD CAM-B3LYP/6-31+G(d) level.

Transition	Excitation energy	Configuration	Oscillator strength
$S_0 \rightarrow S_1$	2.22 eV (558 nm)	H $\rightarrow$ L (94%)	0.0000

## Computational studies of urethane-attached FLAP

The extension calculations of single-molecule **FLAP1'** were carried out by optimizing each structure where the next step structure was extended by 0.15 Å between C<sup>A</sup> and C<sup>B</sup> atoms by using the 'modredundant' keyword of Gaussian16 at the PBE0/6-31G(d) level.

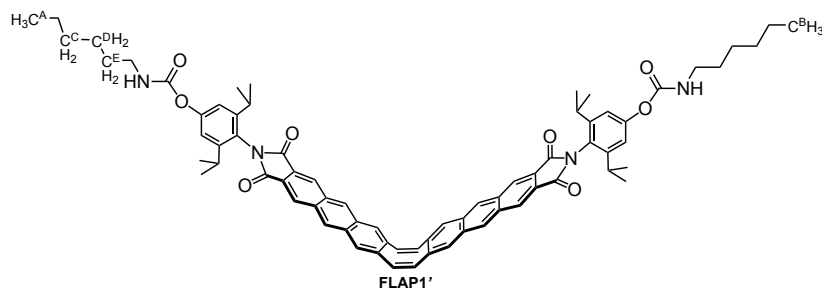


**Fig. S13.** Chemical structures of **FLAP1'** used in the computational extension studies.

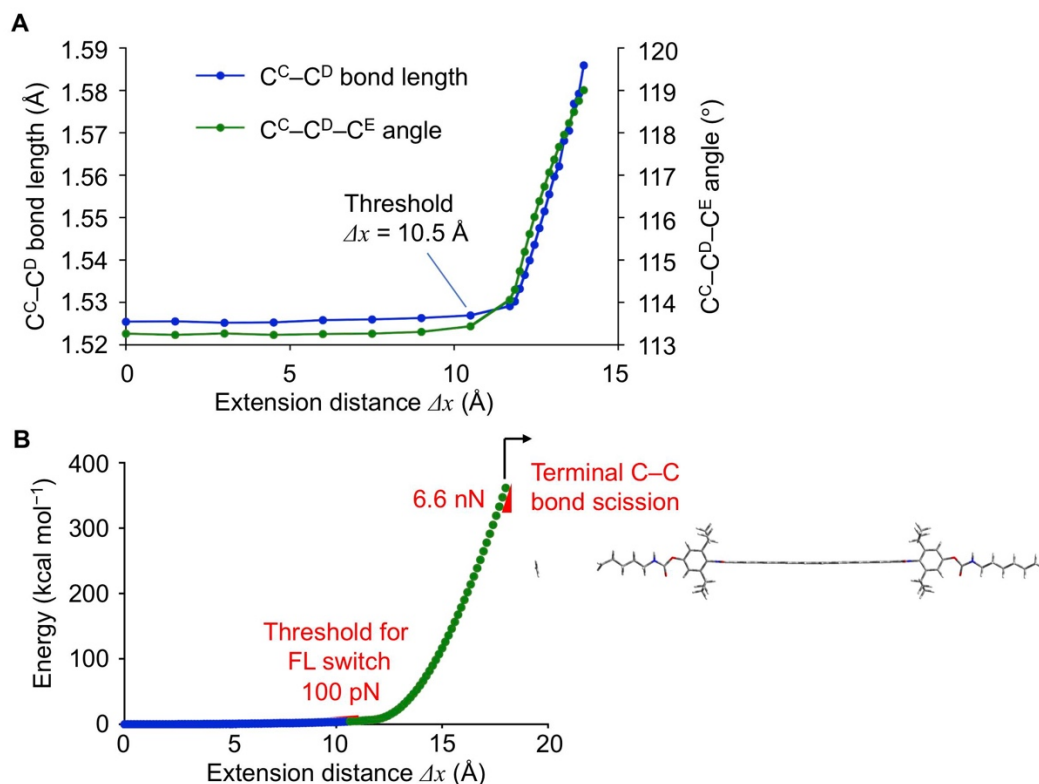


**Fig. S14.** (A) Changes in C–C bond length and C–C–C bond angles of **FLAP1'**. (B) Calculated energy diagram of **FLAP1'** until the terminal C–C bond scission at the PBE0/6-31G(d) level.

## Calculated absorption spectral with long alkyl chain

In order to reproduce the absorption spectral changes upon mechanical testing, we used TD-DFT calculations for the unstretched ( $\Delta x = 0 \text{ \AA}$ ) and fully stretched ( $\Delta x = 13.0 \text{ \AA}$ ) geometries. The simulated absorption spectra (calculated oscillator strengths) are shown in Fig. 3E.

**Table S12.** Summary of excitation energies ( $> 360 \text{ nm}$ ), configurations and oscillator strengths of the  $S_0 \rightarrow S_n$  transitions for unstretched ( $\Delta x = 0 \text{ \AA}$ ) geometries at the TD PBE0/6-31+G(d) level.

Transition	Excitation energy	Configuration(s)	Oscillator strength
$S_0 \rightarrow S_1$	2.87 eV (431 nm)	H $\rightarrow$ L (97%)	0.0000
$S_0 \rightarrow S_2$	2.99 eV (415 nm)	H-1 $\rightarrow$ L (7%) H $\rightarrow$ L+1 (92%)	0.0377
$S_0 \rightarrow S_3$	3.16 eV (391 nm)	H-6 $\rightarrow$ L (16%) H-2 $\rightarrow$ L (2%) H-1 $\rightarrow$ L+3 (7%) H $\rightarrow$ L+2 (69%)	0.2858
$S_0 \rightarrow S_4$	3.20 eV (389 nm)	H-1 $\rightarrow$ L (91%) H $\rightarrow$ L+1 (7%)	0.0149
$S_0 \rightarrow S_5$	3.30 eV (376 nm)	H-6 $\rightarrow$ L+1 (22%) H-2 $\rightarrow$ L+1 (4%) H-1 $\rightarrow$ L+2 (29%) H $\rightarrow$ L+3 (33%)	0.0299
$S_0 \rightarrow S_6$	3.31 eV (375 nm)	H-1 $\rightarrow$ L+1 (96%)	0.0000

**Table S13.** Summary of excitation energies ( $> 360 \text{ nm}$ ), configurations and oscillator strengths of the  $S_0 \rightarrow S_n$  transitions for fully stretched ( $\Delta x = 13.0 \text{ \AA}$ ) geometries at the TD PBE0/6-31+G(d) level.

Transition	Excitation energy	Configurations	Oscillator strength
$S_0 \rightarrow S_1$	2.55 eV (486 nm)	H $\rightarrow$ L (98%)	0.0000
$S_0 \rightarrow S_2$	2.58 eV (481 nm)	H-1 $\rightarrow$ L (38%) H $\rightarrow$ L+1 (59%)	0.1196
$S_0 \rightarrow S_3$	2.89 eV (429 nm)	H-1 $\rightarrow$ L+1 (95%) H-1 $\rightarrow$ L+4 (3%)	0.0000
$S_0 \rightarrow S_4$	2.92 eV (425 nm)	H $\rightarrow$ L+2 (96%)	0.0228
$S_0 \rightarrow S_5$	3.09 eV (401 nm)	H-2 $\rightarrow$ L+1 (37%) H-1 $\rightarrow$ L+2 (49%) H $\rightarrow$ L+3 (9%)	0.0000
$S_0 \rightarrow S_6$	3.14 eV (395 nm)	H-1 $\rightarrow$ L (59%) H $\rightarrow$ L+1 (38%)	5.4348
$S_0 \rightarrow S_7$	3.19 eV (389 nm)	H-2 $\rightarrow$ L (95%) H $\rightarrow$ L+2 (3%)	0.0185
$S_0 \rightarrow S_8$	3.39 eV (366 nm)	H-4 $\rightarrow$ L+2 (10%) H-3 $\rightarrow$ L (87%)	0.0000
$S_0 \rightarrow S_9$	3.39 eV (366 nm)	H-4 $\rightarrow$ L (87%) H-3 $\rightarrow$ L+2 (10%)	0.0236

## Synthesis and characterization of PC

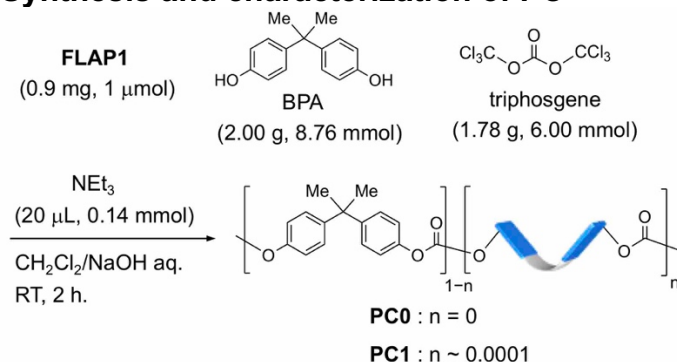


**Figure S15.** Synthesis of polycarbonate.

To the mixtures of bisphenol A (BPA) (2.00 g, 8.76 mmol), which had been recrystallized from AcOH and washed with  $\text{H}_2\text{O}$ , and NaOH (2.73 g, 68.2 mmol) in  $\text{H}_2\text{O}$  (20 mL), **FLAP1** (0.9 mg, 1  $\mu$ mol) and triphosgene (2.60 g, 8.76 mmol) in  $\text{CH}_2\text{Cl}_2$  (20 mL) were added. After addition of triethylamine (TEA) (20  $\mu$ L, 0.14 mmol), the reaction mixture was stirred vigorously at 25  $^\circ\text{C}$  for 2 h. Then, water layer was removed by decantation and the remaining organic layer was poured into MeOH (100 mL). The precipitation was washed with MeOH (100 mL) followed by  $\text{H}_2\text{O}$  (100 mL), and dried under vacuum to give a block of PC ( $\sim 2.3$  g). Punching a PC sheet to obtain a dog-bone shaped specimen JIS K 6251 (No. 3) meeting requirements of ISO 37.

**PU0:**  $^1\text{H NMR}$  (600 MHz,  $\text{CDCl}_3$ )  $\delta$  (ppm) 7.25–7.23 (m, 4H), 7.17–7.15 (m, 4H), and 1.67 (s, 6H).

**PU1:**  $^1\text{H NMR}$  (600 MHz,  $\text{CDCl}_3$ )  $\delta$  (ppm) 7.25–7.24 (m, 4H), 7.17–7.15 (m, 4H), and 1.68 (s, 6H). Note that peaks arising from the FLAP monomer were too small to detect.

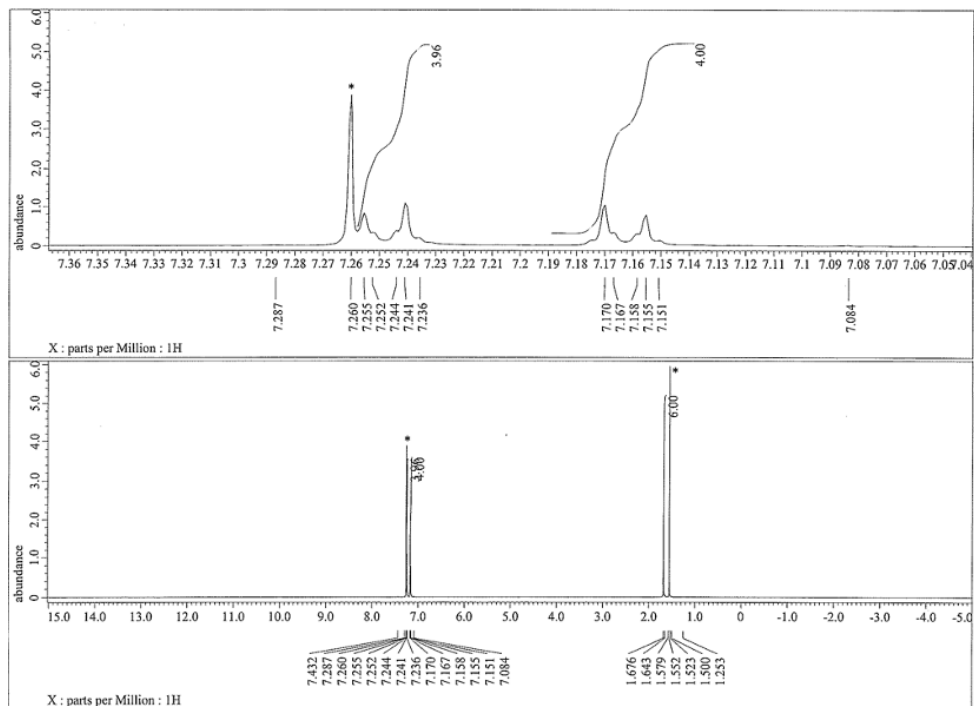


**Figure S16.**  $^1\text{H}$  NMR spectrum of PC0 in  $\text{CDCl}_3$  at 25  $^\circ\text{C}$ . Peaks marked with \* indicate residual solvents.

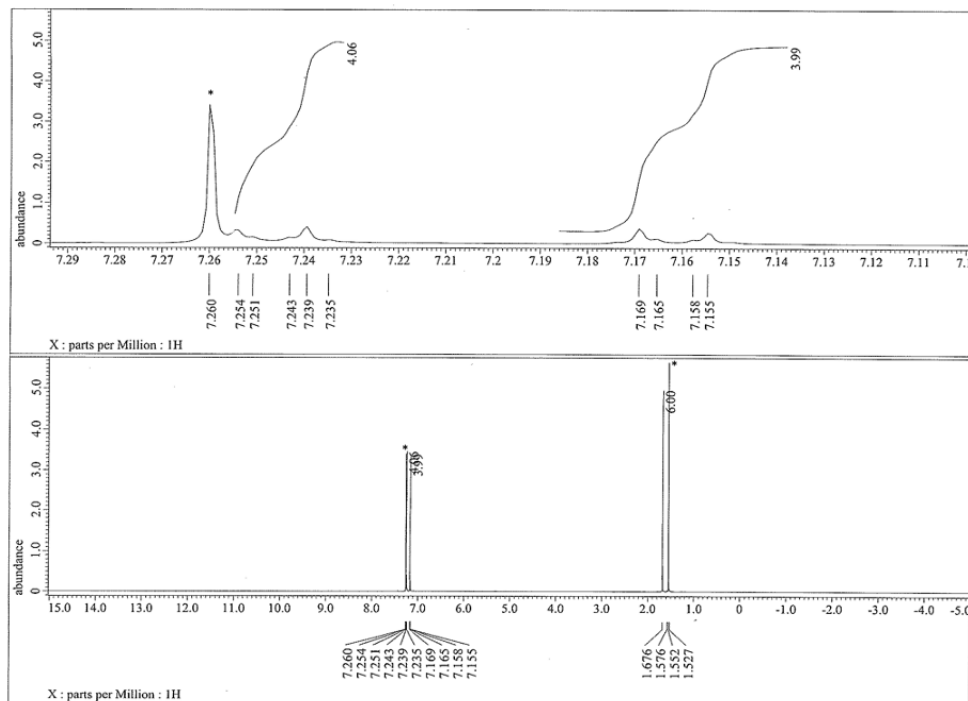


**Figure S17.**  $^1\text{H}$  NMR spectrum of PC1 in  $\text{CDCl}_3$  at 25  $^\circ\text{C}$ . Peaks marked with \* indicate residual solvents.

## DSC measurement of PC

Differential scanning calorimetry (DSC) measurement of the PC specimen was conducted under N<sub>2</sub> atmosphere at a flow speed of 30 mL min<sup>-1</sup>. Heating and cooling process was shown in Figure S18. Figure S19 shows endotherm of the 2nd cooling (E→F) and heating (G→H) cycles. Each sample was placed into an aluminum pan and covered with an aluminum cover, which was well pressed with a designated pressing tool. A vacant pan and a cover, which was also pressed, was used as a reference sample.

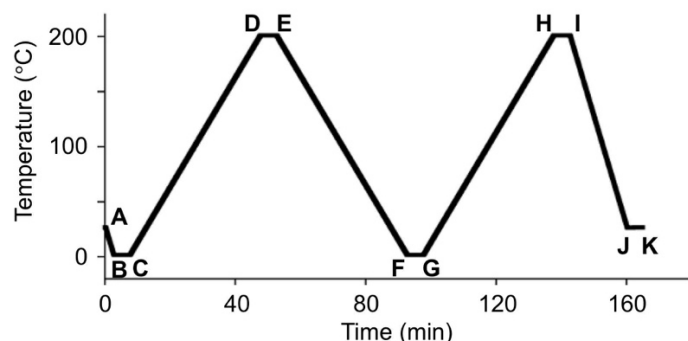


**Figure S18.** Heating and cooling process of DSC measurement of PC.

**A→B:** Cooling from 25 to 0 °C at a rate of 5 °C min<sup>-1</sup>.

**B→C:** Hold at 0 °C for 5 min.

**C→D:** Heating from 0 to 200 °C at a rate of 5 °C min<sup>-1</sup>.

**D→E:** Hold at 200 °C for 5 min.

**E→F:** Cooling from 200 to 0 °C at a rate of 5 °C min<sup>-1</sup>

**F→G:** Hold at 0 °C for 5 min.

**G→H:** Heating from 0 to 200 °C at a rate of 5 °C min<sup>-1</sup>.

**H→I:** Hold at 200 °C for 5 min.

**I→J:** Cooling from 200 to 25 °C at a rate of 10 °C min<sup>-1</sup>.

**J→K:** Hold at 25 °C for 5 min.

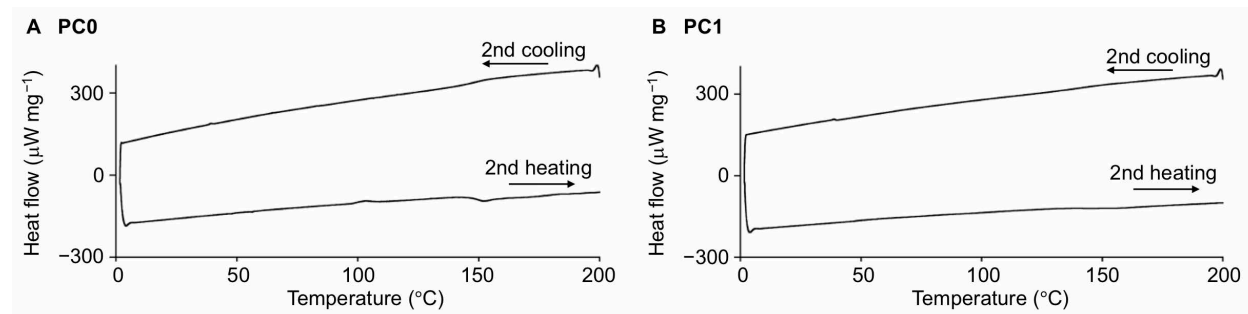


**Figure S19.** DSC traces of PC0 and PC1.

**Table S14.** Summary of DSC measurement of PC.

	weight (mg)	$T_g$ (°C)
<b>PC0</b>	4.96	151
<b>PC1</b>	6.14	153

## Mechanical properties of PC

Uniaxial tensile tests were carried out on dumbbell-shaped specimens. True strain  $\epsilon_{\text{true}}$  is calculated by  $\epsilon_{\text{true}} = \ln(L/L_0)$ , where crosshead displacement is  $L$  and the initial length ( $L_0 = 30$  mm). True stress  $\sigma_{\text{true}}$  is calculated by  $\sigma_{\text{true}} = F/A$ , where  $F$  is the recorded force and  $A$  is the cross-sectional area for deformed specimen. Here, the cross-sectional area is determined by approximating the specimen as incompressible and is calculated by  $A = A_0(L/L_0)$ , where  $A_0$  is the initial cross-sectional area for the specimen. Toughness was calculated based on an area of the true stress–strain (S–S) curve. Young’s modulus is defined as the slope of S–S curves at 0–1% true strain. Tensile velocity was fixed at  $5 \text{ mm min}^{-1}$ , corresponding to strain rate of  $2.8 \times 10^{-3} \text{ s}^{-1}$ .

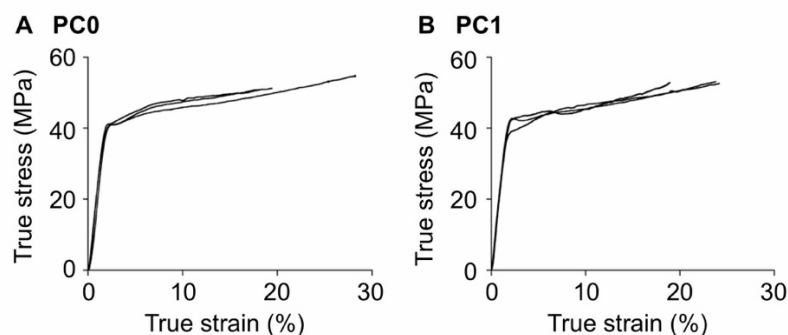


**Figure S20.** S–S curves of **PC0** and **PC1**.

**Table S15.** Summary of mechanical properties for PC.

	True strain at break (%)	True stress at break (MPa)	Toughness at break ( $\text{MJ m}^{-3}$ )	Young’s modulus (GPa)
<b>PC0</b>	$22.0 \pm 5.4$	$52.3 \pm 2.1$	$10.3 \pm 2.3$	$2.20 \pm 0.28$
<b>PC1</b>	$22.3 \pm 2.9$	$52.9 \pm 0.3$	$10.0 \pm 1.4$	$2.49 \pm 0.10$

## Photophysical properties of non-stretched PU

Photophysical properties of **PC1** in Figs. S21 and S22 were recorded on a JASCO Spectrofluorometer FP-8500. No excimer formation was observed in this experiment.

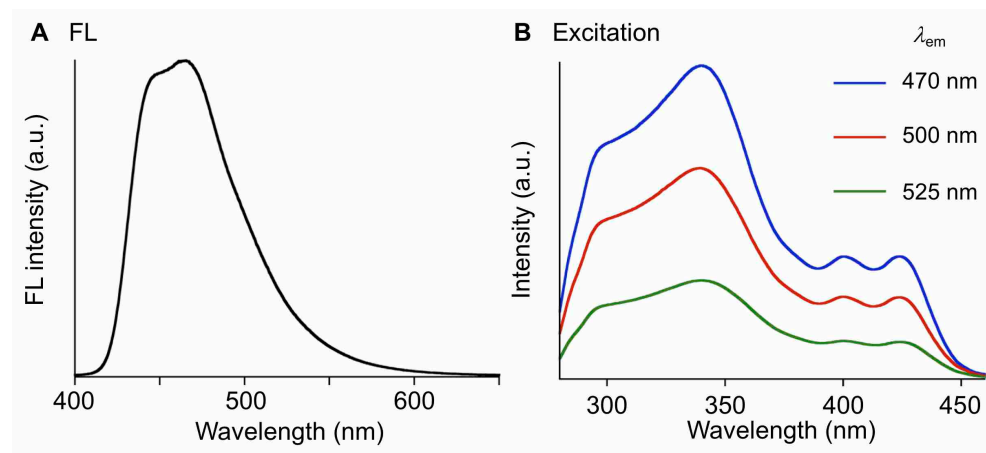


**Figure S21.** (A) FL and (B) excitation spectra of **PC1**.

**Table S16.** Photophysical constants of **PC1**.  $\lambda_{\text{ex}} = 365$  nm.

$\Phi_{\text{FL}}$	$\tau_{\text{FL}}$ (ns) <sup>a</sup>	$k_{\text{r}}$ (s <sup>-1</sup> )	$k_{\text{nr}}$ (s <sup>-1</sup> )
0.30	6.8	$4.4 \times 10^7$	$1.0 \times 10^8$

<sup>a</sup>  $\lambda_{\text{em}} = 470$  nm.

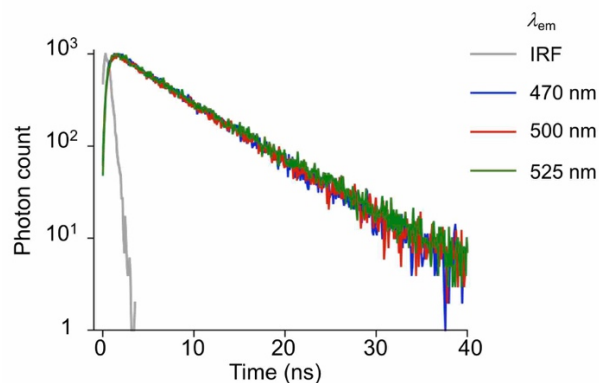


**Figure S22.** FL decay profiles of **PC1**.  $\lambda_{\text{ex}} = 365$  nm.

**Table S17.** Photophysical constants of **PC1**.  $\lambda_{\text{ex}} = 365$  nm.

$\lambda_{\text{em}}$ (nm)	$\chi^2$	$\tau_{\text{FL}}$ (ns)
470	1.11	6.8
500	1.26	6.8
525	1.24	7.0

## **FL measurement under microscope of PC**

This experiment was conducted by combination use of a microscope (OLYMPUS inverted research microscope IX83), a tensile testing machine (AcroEdge tensile testing machine OZ911) and a hyperspectral camera (EBAJAPAN hyperspectral camera NH-8). A strip PC specimen (width  $\sim 1$  mm and thickness  $\sim 0.03$  mm), which was half-cut for a single notch by a scissors was used for the test. This specimen was held with an initial distance of 25 mm, and was extended at the speed of  $0.05 \text{ mm s}^{-1}$  from both sides. At the same time, FL spectra were obtained through the hyperspectral camera. The data was acquired by an exposure time of 500 ms at an interval of 5 nm. The FL optical micrograph (shown in Fig. 3B) was taken by a digital camera (OLYMPUS TG-6).

## Synthesis of PU

Poly(tetrahydrofuran) (PTHF,  $M_n \sim 650$ , Aldrich) was dried under vacuum ( $\sim 2$  torr) for 2 h at 70 °C. After cooling to 25 °C, dimethylformamide (DMF, Super dehydrated grade, Wako Chemicals), FLAP, hexamethylene diisocyanate (HDI, TCI chemicals) and triethanolamine (TEA, Wako Chemicals) were added, and the reaction mixture was stirred at 25 °C for 10 min. Then, dibutyltin dilaurate (DBTDL, Aldrich) (30  $\mu$ L, 50  $\mu$ mol) in THF (0.5 mL) was added to the reaction and stirred at 25 °C for 2 min. The reaction mixture was poured into a Teflon mold and polymerized under  $N_2$  atmosphere at 25 °C for 48 h. Then, dog-bone shaped specimens were wash with  $H_2O$  and dried under vacuum for 8 h at 70 °C to obtain transparent PU specimens with thickness of 1.5 mm and width of 6 mm.

The distance between each FLAP molecule in PU was estimated to be 20 nm as follows; the weight ratio of FLAP to the polymer was 0.2 mg  $g^{-1}$  equal to 0.2  $\mu$ mol  $m^{-3}$  (polymer density: 1.0  $g\ cm^{-3}$ ). Therefore, the volume occupied by one molecule FLAP was calculated to be  $8.0 \times 10^{-24}\ m^3$ . Taking the cube root, the average-distance between each chromophore was determined to be  $2.0 \times 10^{-8}\ m^3$  (20 nm).

**Table S18.** Synthesis of PU0.

	PU0(0.087)	PU0(0.10)	PU0(0.13)
PTHF	5.22 g (8.03 mmol)	4.80 g (7.38 mmol)	4.99 g (7.68 mmol)
HDI	1.73 mL (10.8 mmol)	1.65 mL (10.3 mmol)	1.94 mL (12.1 mmol)
TEA	268 mg (1.80 mmol)	292 mg (1.96 mmol)	439 mg (2.94 mmol)
DMF	14.9 mL	13.9 mL	14.5 mL

**Table S19.** Synthesis of PU1.

	PU1(0.087)	PU1(0.10)	PU1(0.13)
FLAP1	1.5 mg (1.7 $\mu$ mol)	1.3 mg (1.5 $\mu$ mol)	1.6 mg (1.8 $\mu$ mol)
PTHF	5.14 g (7.91 mmol)	4.67 g (7.18 mmol)	5.03 g (7.74 mmol)
HDI	1.69 mL (10.5 mmol)	1.61 mL (10.0 mmol)	1.96 mL (12.2 mmol)
TEA	262 mg (1.75 mmol)	285 mg (1.91 mmol)	443 mg (2.97 mmol)
DMF	14.7 mL	13.5 mL	14.5 mL
FLAP/polymer <sup>a</sup>	0.21 mg $g^{-1}$	0.20 mg $g^{-1}$	0.21 mg $g^{-1}$

<sup>a</sup> Weight ratio of FLAP to the polymer.

**Table S20.** Synthesis of PU2.

	PU2(0.087)	PU2(0.10)	PU2(0.13)
FLAP2	1.5 mg (1.5 $\mu$ mol)	1.5 mg (1.5 $\mu$ mol)	1.5 mg (1.5 $\mu$ mol)
PTHF	5.21 g (8.01 mmol)	5.49 g (8.45 mmol)	4.92 g (7.57 mmol)
HDI	1.71 mL (10.6 mmol)	1.89 mL (11.8 mmol)	1.91 mL (11.9 mmol)
TEA	266 mg (1.78 mmol)	335 mg (2.24 mmol)	430 mg (2.88 mmol)
DMF	14.9 mL	15.9 mL	14.2 mL
FLAP/polymer <sup>a</sup>	0.21 mg $g^{-1}$	0.19 mg $g^{-1}$	0.20 mg $g^{-1}$

<sup>a</sup> Weight ratio of FLAP to the polymer.

## DSC measurement of PU

Differential scanning calorimetry (DSC) measurement of the PU specimen was conducted under N<sub>2</sub> atmosphere at a flow speed of 30 mL min<sup>-1</sup>. Heating and cooling process was shown in Figure S23. Figure S25 shows endotherm of the 2nd cooling (E→F) and heating (G→H) cycles. Each sample was placed into an aluminum pan and covered with an aluminum cover, which was well pressed with a designated pressing tool. A vacant pan and a cover, which was also pressed, was used as a reference sample.

The degree and easiness of crystallization was more pronounced in the smaller cross-linking density as suggested in the values of  $\Delta H_{r \rightarrow c}$  and  $\Delta H_{c \rightarrow r}$ . Cross-Nicol images also suggest that crystalline specimens were transformed into rubbery state (optically isotropic) upon heating.

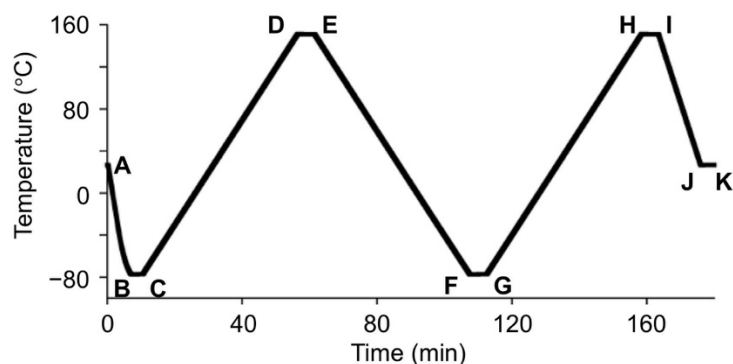


**Fig. S23.** Heating and cooling process of DSC measurement of PU.

**A→B:** Cooling from 25 to -80 °C at a rate of 20 °C min<sup>-1</sup>.

**B→C:** Hold at -80 °C for 5 min.

**C→D:** Heating from -80 to 150 °C at a rate of 5 °C min<sup>-1</sup>.

**D→E:** Hold at 150 °C for 5 min.

**E→F:** Cooling from 150 to -80 °C at a rate of 5 °C min<sup>-1</sup>

**F→G:** Hold at -80 °C for 5 min.

**G→H:** Heating from -80 to 150 °C at a rate of 5 °C min<sup>-1</sup>.

**H→I:** Hold at 150 °C for 5 min.

**I→J:** Cooling from 150 to 25 °C at a rate of 10 °C min<sup>-1</sup>.

**J→K:** Hold at 25 °C for 5 min.

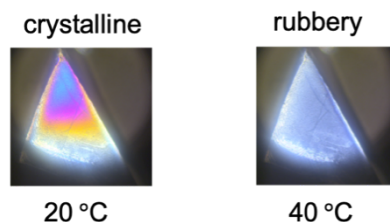


**Fig. S24.** Cross-Nicol images of PU0(0.087) at 20 and 40 °C.

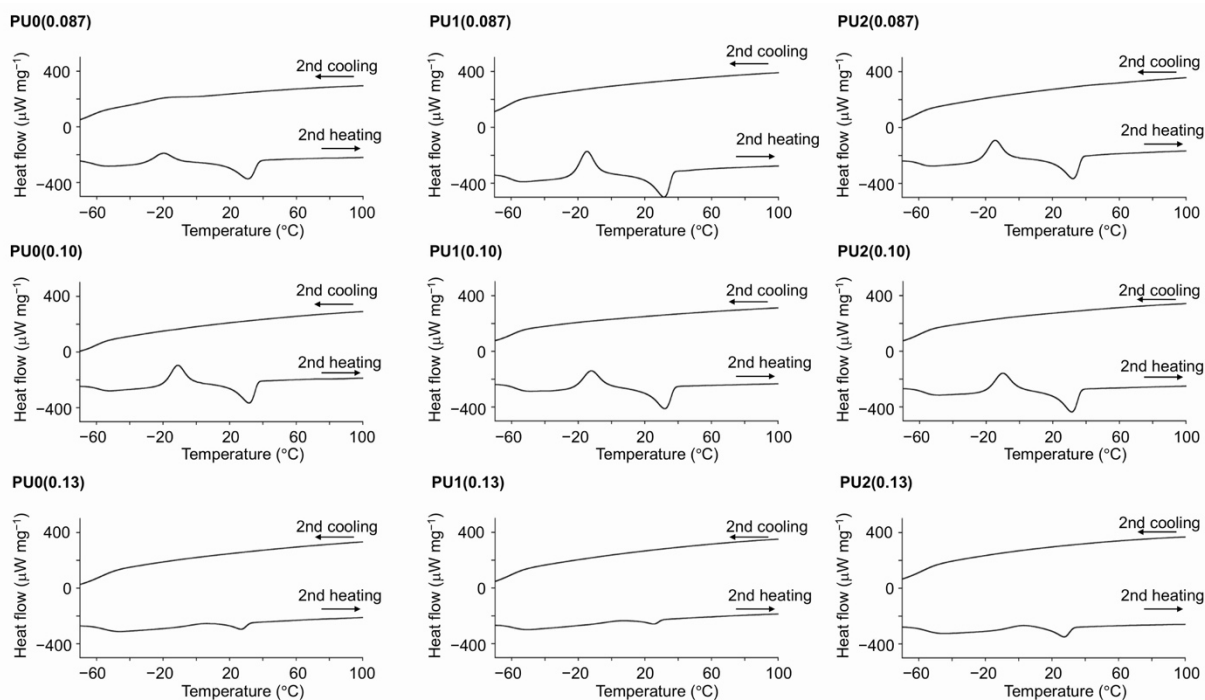


**Fig. S25.** DSC traces of PUs.

**Table S21.** Summary of DSC measurement of PUs.

	weight (mg)	$T_g$ (°C) <sup>a</sup>	$T_{r \rightarrow c}$ (°C) <sup>b</sup>	$\Delta H_{r \rightarrow c}$ (J g <sup>-1</sup> ) <sup>c</sup>	$T_{c \rightarrow r}$ (°C) <sup>d</sup>	$\Delta H_{c \rightarrow r}$ (J g <sup>-1</sup> ) <sup>e</sup>
<b>PU0(0.087)</b>	7.50	-60	-19	-16	31	21
<b>PU1(0.087)</b>	6.42	-60	-14	-24	31	24
<b>PU2(0.087)</b>	6.25	-58	-14	-24	32	22
<b>PU0(0.10)</b>	6.84	-58	-11	-23	32	20
<b>PU1(0.10)</b>	9.99	-56	-12	-24	32	22
<b>PU2(0.10)</b>	7.33	-57	-10	-26	31	19
<b>PU0(0.13)</b>	6.67	-56	5	-3.7	27	5.7
<b>PU1(0.13)</b>	6.01	-59	8	-2.8	25	4.0
<b>PU2(0.13)</b>	5.88	-56	3	-3.9	27	6.5

<sup>a</sup> Glass transition temperature determined by the maximum DDSC peak of the 2nd heating run.

<sup>b</sup> Rubbery-to-crystalline crystallization temperature determined by the DDSC value of the 2nd heating run to be 0.

<sup>c</sup> Enthalpy of rubbery-to-crystalline transition determined by the area of the DSC curve.

<sup>d</sup> Crystalline-to-rubbery crystallization temperature determined by the DDSC value of the 2nd heating run to be 0.

<sup>e</sup> Enthalpy of crystalline-to rubbery transition determined by the area of the DSC curve.

## Rheological measurement of PU

Dynamic mechanical analysis (DMA) was conducted on an Anton Paar MCR 702 rheometer at a cooling rate of  $5\text{ }^{\circ}\text{C min}^{-1}$  from 100 to  $0\text{ }^{\circ}\text{C}$  at a frequency of 1 Hz with a 10-mm parallel plate. At this temperature range, no rheological characteristic peaks were observed and storage modulus  $G'$  was within the orders of  $10^5$  Pa.

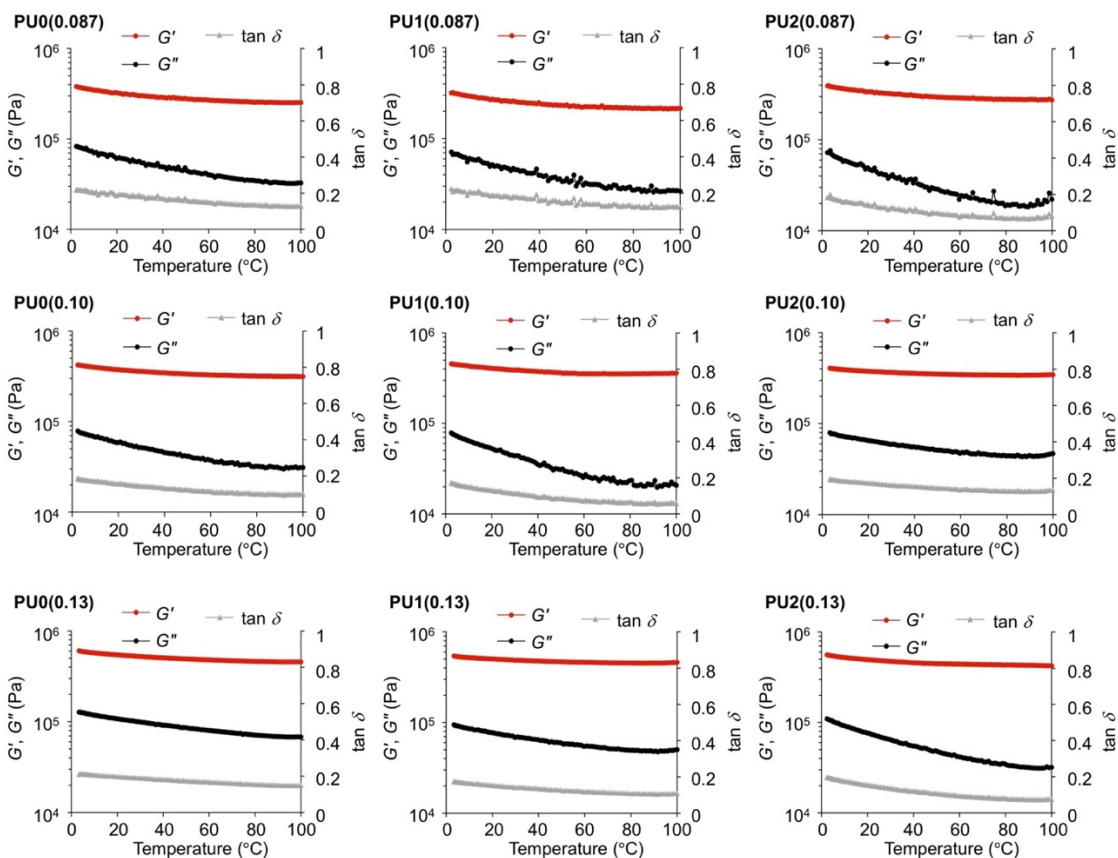


Fig. S26. DMA traces of PUs.

Table S22. Summary of rheometric measurement for PUs at  $25\text{ }^{\circ}\text{C}$ .

	$G'$ (Pa) <sup>a</sup>	$G''$ (Pa) <sup>b</sup>	$\tan \delta$ <sup>c</sup>
<b>PU0(0.087)</b>	$3.1 \times 10^5$	$5.9 \times 10^4$	0.19
<b>PU1(0.087)</b>	$2.6 \times 10^5$	$4.8 \times 10^4$	0.18
<b>PU2(0.087)</b>	$3.3 \times 10^5$	$4.2 \times 10^4$	0.13
<b>PU0(0.10)</b>	$3.7 \times 10^5$	$5.5 \times 10^4$	0.15
<b>PU1(0.10)</b>	$3.9 \times 10^5$	$4.8 \times 10^4$	0.12
<b>PU2(0.10)</b>	$3.7 \times 10^5$	$6.2 \times 10^4$	0.17
<b>PU0(0.13)</b>	$5.3 \times 10^5$	$1.0 \times 10^5$	0.19
<b>PU1(0.13)</b>	$4.9 \times 10^5$	$7.3 \times 10^4$	0.15
<b>PU2(0.13)</b>	$4.8 \times 10^5$	$7.0 \times 10^4$	0.15

<sup>a</sup> Storage modulus at  $25\text{ }^{\circ}\text{C}$ . <sup>b</sup> Loss modulus at  $25\text{ }^{\circ}\text{C}$ . <sup>c</sup> Loss tangent calculated from  $G''/G'$  at  $25\text{ }^{\circ}\text{C}$ .

## Mechanical properties of rubbery PU

Uniaxial tensile tests were carried out on dumbbell-shaped specimens. Rubbery samples were prepared by heating at 60 °C for 1 min with a handy dryer. Nominal stress,  $\sigma_N$ , is defined as a force  $f$  divided by the initial cross-sectional area  $S_0$  (typically 1.5-mm thickness  $\times$  6-mm width).

$$\sigma_N = \frac{f}{S_0}$$

Nominal strain,  $\epsilon_N$ , is defined as sample gauge ( $\Delta L$ ) divided by the initial length ( $L_0 = 10$  mm).

$$\epsilon_N = \frac{\Delta L}{L_0}$$

Toughness  $U$  was calculated based on an area of the stress–strain (S–S) curve.

Young's modulus  $E$  is defined as the slope of S–S curves at 0–10% strain. Tensile velocity was fixed at 100 mm min<sup>-1</sup>, corresponding to strain rate of 0.17 s<sup>-1</sup>.

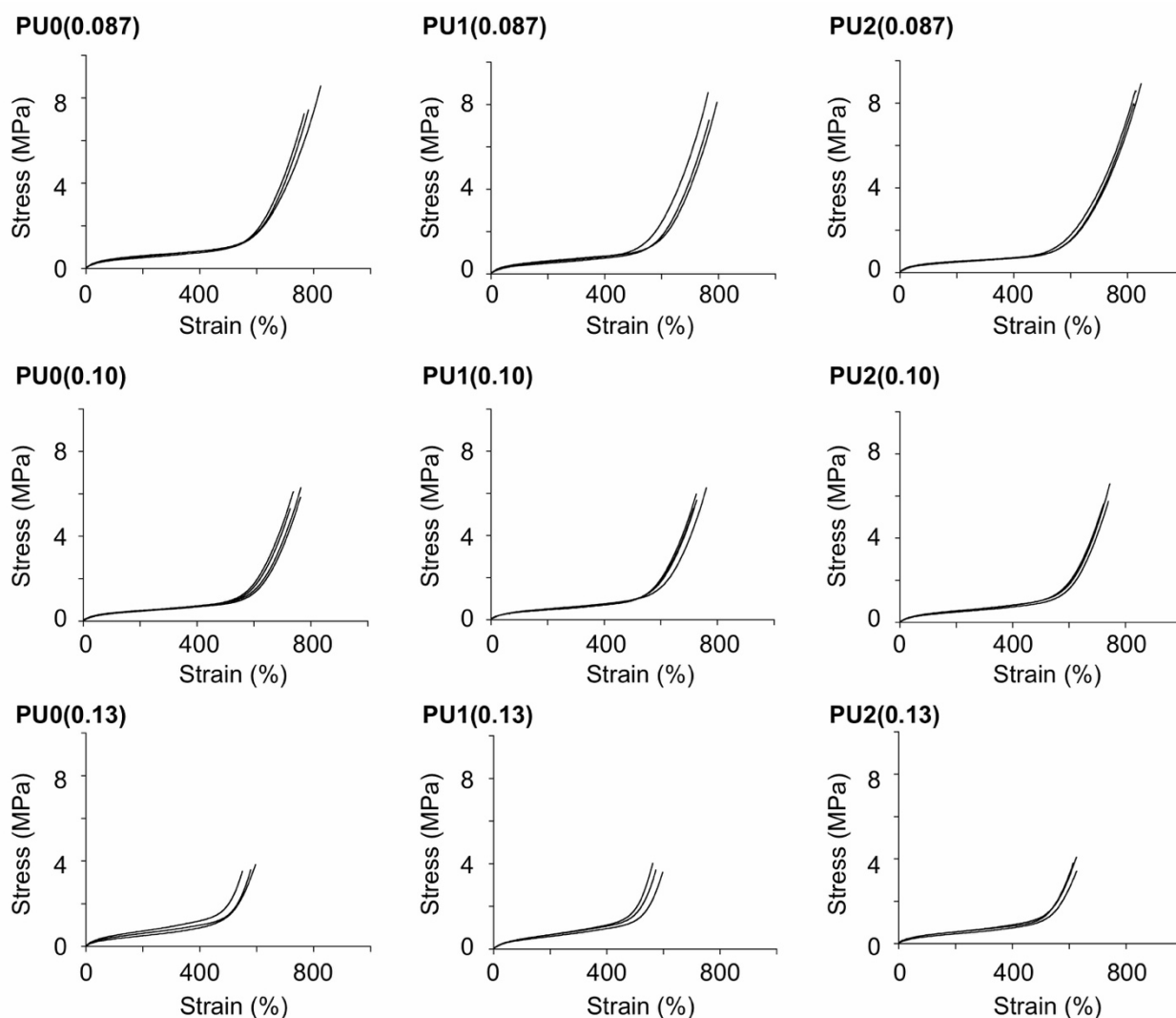


**Fig. S27.** S–S curves of rubbery PUs.

**Table S23.** Summary of mechanical properties of uniaxial tests for rubbery PUs.

	Strain at break (%)	Stress at break (MPa)	Toughness at break (MJ m <sup>-3</sup> )	Young's modulus (MPa)
<b>PU0(0.087)</b>	801 ± 44	7.2 ± 1.9	12.0 ± 3.3	1.2 ± 0.1
<b>PU1(0.087)</b>	791 ± 30	7.8 ± 0.7	12.3 ± 1.2	1.2 ± 0.2
<b>PU2(0.087)</b>	824 ± 8	8.2 ± 0.3	12.6 ± 0.5	1.1 ± 0.1
<b>PU0(0.10)</b>	749 ± 19	5.9 ± 0.4	8.7 ± 0.7	1.1 ± 0.1
<b>PU1(0.10)</b>	732 ± 20	5.8 ± 0.4	8.6 ± 0.7	1.0 ± 0.1
<b>PU2(0.10)</b>	733 ± 11	6.0 ± 0.4	9.2 ± 1.0	1.1 ± 0.1
<b>PU0(0.13)</b>	575 ± 24	3.6 ± 0.2	5.4 ± 0.2	1.1 ± 0.1
<b>PU1(0.13)</b>	577 ± 18	3.6 ± 0.4	5.6 ± 0.1	1.1 ± 0.1
<b>PU2(0.13)</b>	616 ± 12	4.0 ± 0.5	5.8 ± 0.6	1.1 ± 0.2

Values of average ± standard deviation of 3–4 specimen were shown.

FL spectra in Figs. S28–33 were recorded on a JASCO Spectrofluorometer FP-8500. Crystalline samples were used as stored at room temperature for more than 2 days. Rubbery samples were prepared by heating at 60 °C for 1 min with a handy dryer.

Although mechanical properties were largely affected by crystallinity (Fig. S41), changes in FL spectra, FL quantum yields, and FL lifetimes were almost negligible regardless of the crystallinity for unstretched PU. No excimer formation was observed in this experiment.

**Table S24.** Photophysical constants of PUs.  $\lambda_{\text{ex}} = 365$  nm.

	$\Phi_{\text{FL}}$	$\tau_{\text{FL}}$ (ns) <sup>a</sup>	$k_{\text{r}}$ (s <sup>-1</sup> )	$k_{\text{nr}}$ (s <sup>-1</sup> )
crystalline <b>PU1(0.087)</b>	0.30	6.8	$4.4 \times 10^7$	$1.0 \times 10^8$
rubbery <b>PU1(0.087)</b>	0.26	6.9	$3.8 \times 10^7$	$1.1 \times 10^8$
crystalline <b>PU1(0.10)</b>	0.30	6.7	$4.4 \times 10^7$	$1.0 \times 10^8$
rubbery <b>PU1(0.10)</b>	0.28	6.9	$4.0 \times 10^7$	$1.0 \times 10^8$
crystalline <b>PU1(0.13)</b>	0.33	6.9	$4.8 \times 10^7$	$9.7 \times 10^7$
rubbery <b>PU1(0.13)</b>	0.31	7.1	$4.3 \times 10^7$	$9.8 \times 10^7$
crystalline <b>PU2(0.087)</b>	0.35	6.8	$5.1 \times 10^7$	$9.6 \times 10^7$
rubbery <b>PU2(0.087)</b>	0.37	7.0	$3.8 \times 10^7$	$9.0 \times 10^7$
crystalline <b>PU2(0.10)</b>	0.35	6.7	$5.2 \times 10^7$	$9.6 \times 10^7$
rubbery <b>PU2(0.10)</b>	0.35	7.1	$5.0 \times 10^7$	$9.1 \times 10^7$
crystalline <b>PU2(0.13)</b>	0.33	7.0	$4.6 \times 10^7$	$9.6 \times 10^7$
rubbery <b>PU2(0.13)</b>	0.33	6.9	$4.8 \times 10^7$	$9.7 \times 10^7$

<sup>a</sup>  $\lambda_{\text{em}} = 470$  nm.

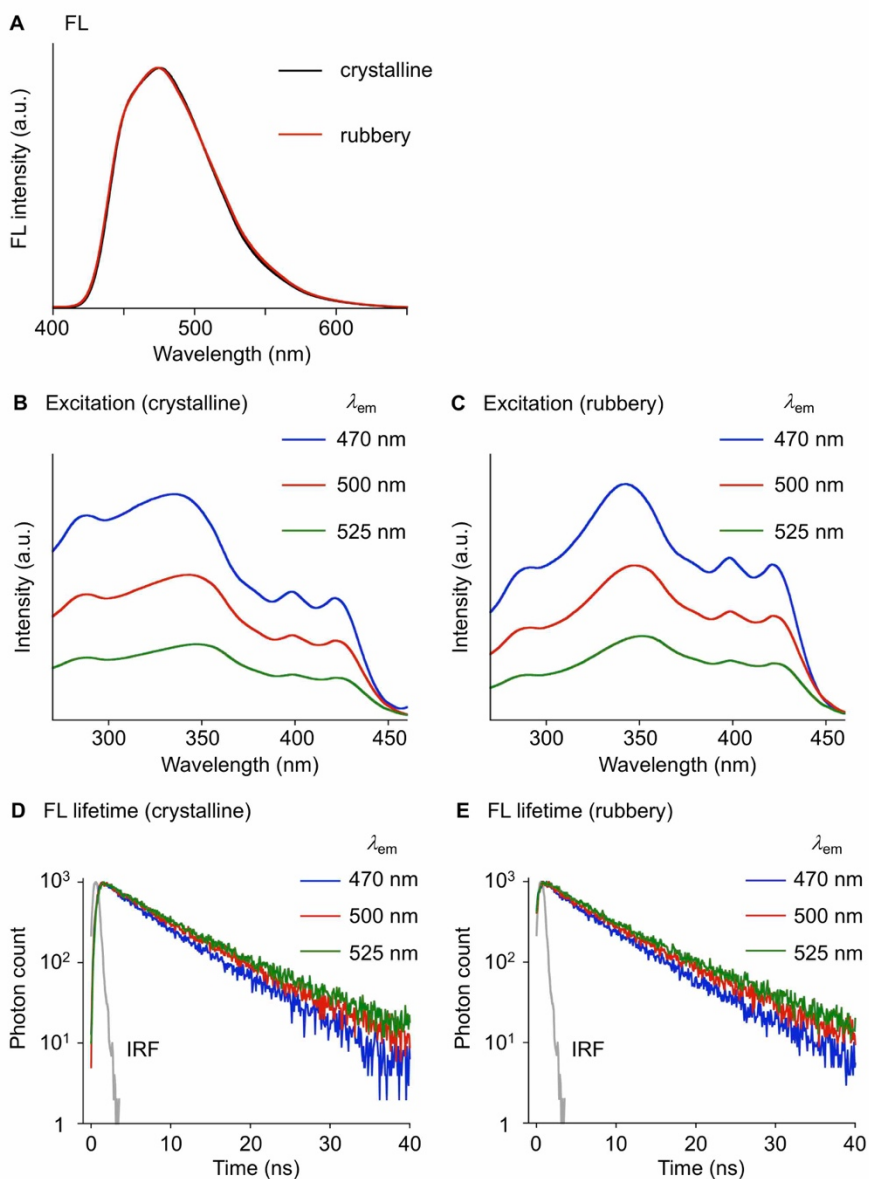


**Fig. S28.** (A) FL spectra of crystalline and rubbery **PU1(0.087)**.  $\lambda_{\text{ex}} = 365$  nm. Excitation spectra of (B) crystalline and (C) rubbery **PU1(0.087)**. FL decay profiles of (D) crystalline and (E) rubbery **PU1(0.087)**.

**Table S25.** Photophysical constants of **PU1(0.087)**.  $\lambda_{\text{ex}} = 365$  nm.

	$\lambda_{\text{em}}$ (nm)	$\chi^2$	$\tau_{\text{FL}}$ (ns)	$\tau_1$ (ns)	$\tau_2$ (ns)	$A_1$	$A_2$
crystalline	470	1.26	6.8	2.1	7.3	36	90
	500	1.19	7.8	2.8	8.4	33	88
	525	1.12	9.0	5.7	11.8	73	40
rubbery	470	1.02	6.9	2.3	7.5	36	88
	500	1.07	8.2	4.6	9.9	58	60
	525	1.05	9.6	6.2	14.3	90	28

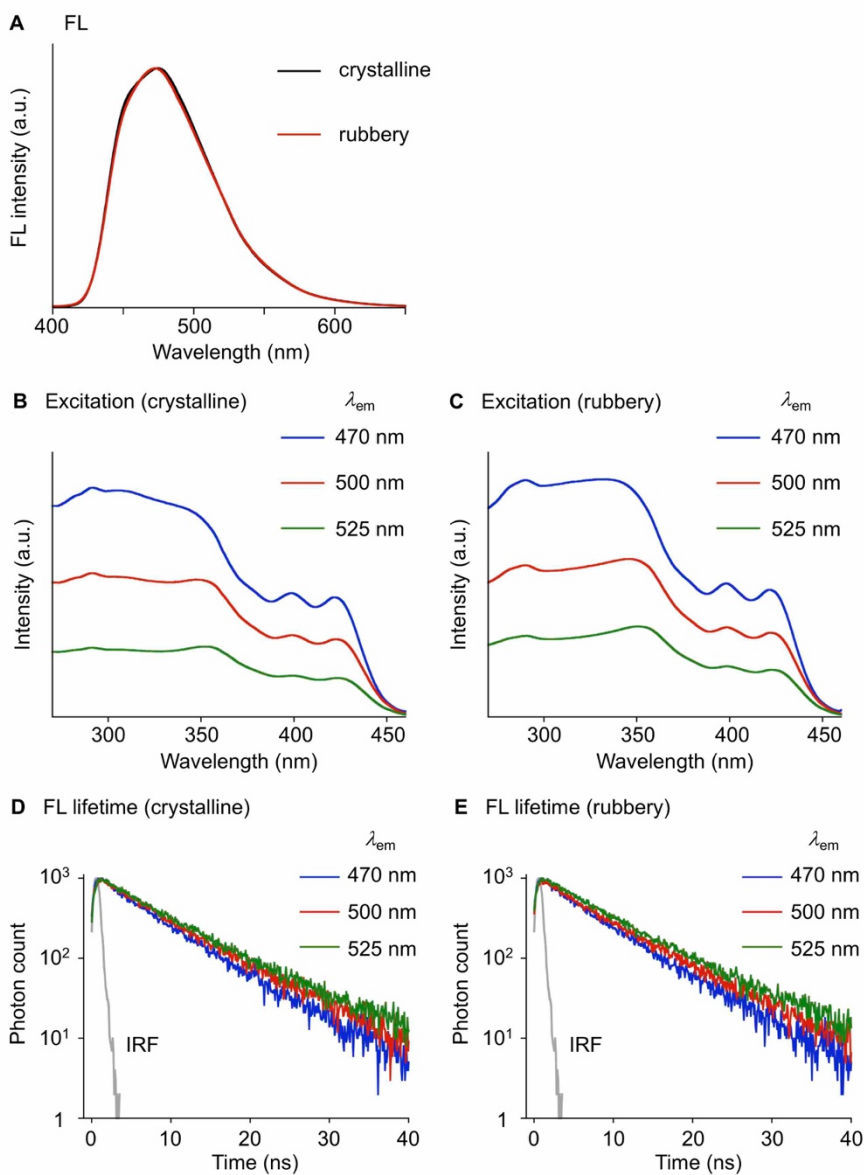


**Fig. S29.** (A) FL spectra of crystalline and rubbery **PU1(0.10)**.  $\lambda_{\text{ex}} = 365$  nm. Excitation spectra of (B) crystalline and (C) rubbery **PU1(0.10)**. FL decay profiles of (D) crystalline and (E) rubbery **PU1(0.10)**.

**Table S26.** Photophysical constants of **PU1(0.10)**.  $\lambda_{\text{ex}} = 365$  nm.

	$\lambda_{\text{em}}$ (nm)	$\chi^2$	$\tau_{\text{FL}}$ (ns)	$\tau_1$ (ns)	$\tau_2$ (ns)	$A_1$	$A_2$
crystalline	470	1.07	6.7	1.5	7.1	34	98
	500	1.13	7.6	3.2	8.1	25	90
	525	1.10	9.0	6.5	13.6	90	23
rubbery	470	1.15	6.9	2.8	7.4	32	90
	500	1.04	8.8	6.6	15.8	98	13
	525	1.10	9.7	7.3	19.4	108	10

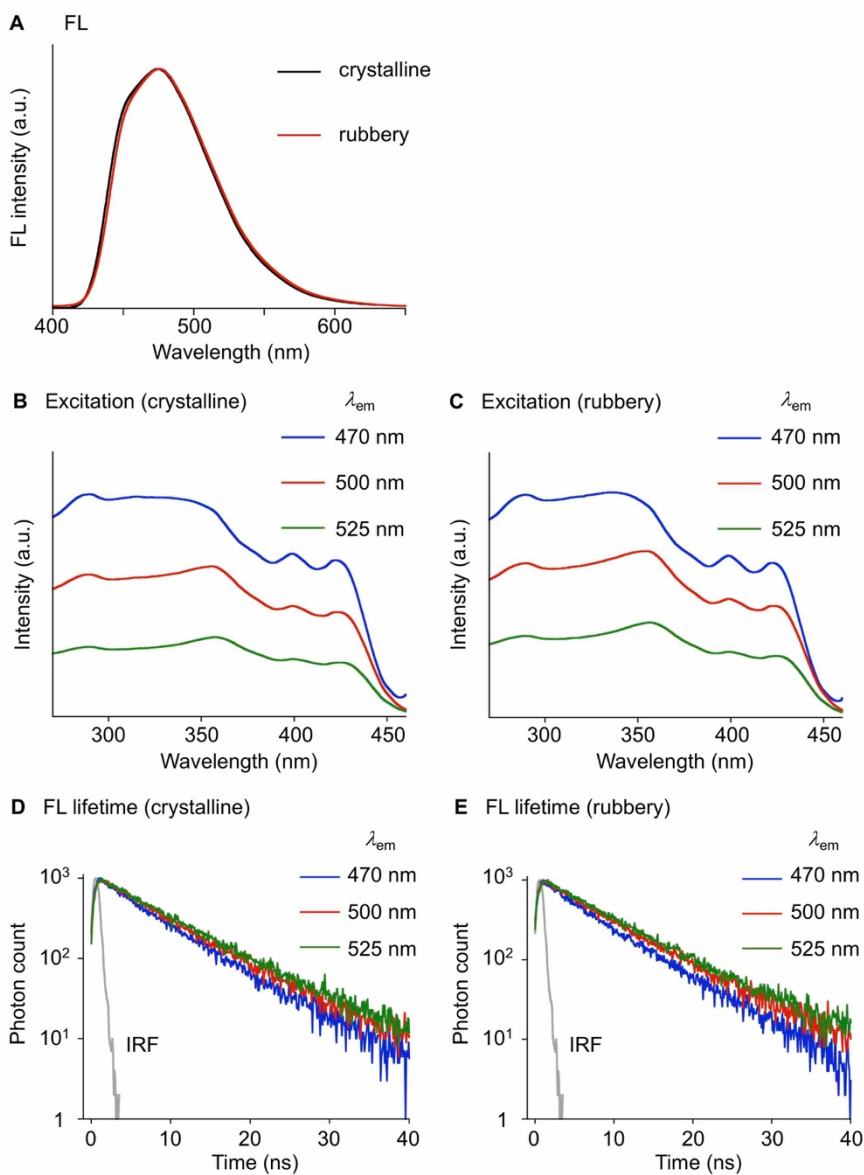


**Fig. S30.** (A) FL spectra of crystalline and rubbery **PU1(0.13)**.  $\lambda_{\text{ex}} = 365$  nm. Excitation spectra of (B) crystalline and (C) rubbery **PU1(0.13)**. FL decay profiles of (D) crystalline and (E) rubbery **PU1(0.13)**.

**Table S27.** Photophysical constants of **PU1(0.13)**.  $\lambda_{\text{ex}} = 365$  nm.

	$\lambda_{\text{em}}$ (nm)	$\chi^2$	$\tau_{\text{FL}}$ (ns)	$\tau_1$ (ns)	$\tau_2$ (ns)	$A_1$	$A_2$
crystalline	470	1.09	6.9	2.1	7.5	26	94
	500	1.02	8.0	6.0	10.3	74	39
	525	1.07	10.3	8.7	13.6	91	19
rubbery	470	1.06	7.1	4.2	8.3	52	64
	500	1.16	7.9	2.9	8.4	29	94
	525	1.09	8.6	5.3	9.8	48	70

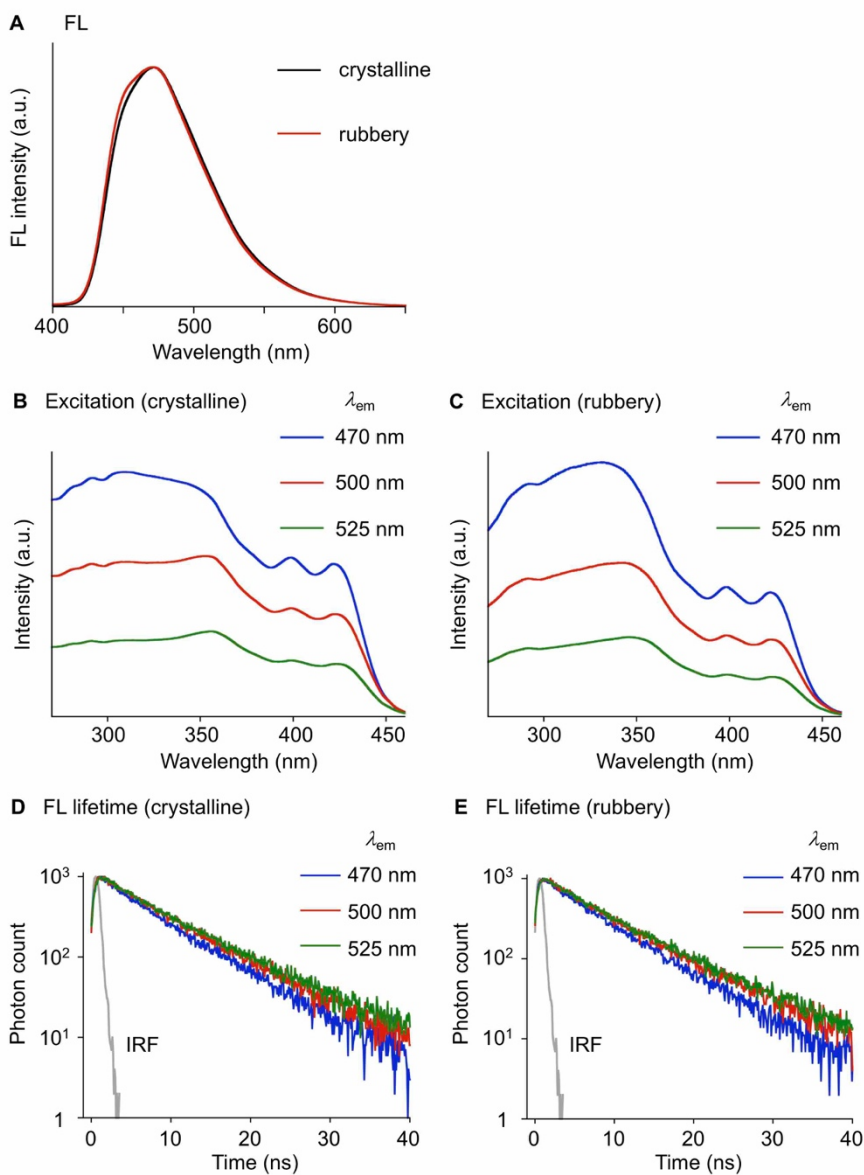


**Fig. S31.** (A) FL spectra of crystalline and rubbery **PU2(0.087)**.  $\lambda_{\text{ex}} = 365$  nm. Excitation spectra of (B) crystalline and (C) rubbery **PU2(0.087)**. FL decay profiles of (D) crystalline and (E) rubbery **PU2(0.087)**.

**Table S28.** Photophysical constants of **PU2(0.087)**.  $\lambda_{\text{ex}} = 365$  nm.

	$\lambda_{\text{em}}$ (nm)	$\chi^2$	$\tau_{\text{FL}}$ (ns)	$\tau_1$ (ns)	$\tau_2$ (ns)	$A_1$	$A_2$
crystalline	470	1.16	6.8	1.6	7.2	30	96
	500	1.01	7.8	3.4	8.4	31	88
	525	1.17	8.5	4.6	9.7	46	69
rubbery	470	0.99	7.0	2.8	7.5	28	94
	500	1.13	8.2	5.1	9.6	56	64
	525	1.02	8.8	6.0	11.4	76	42

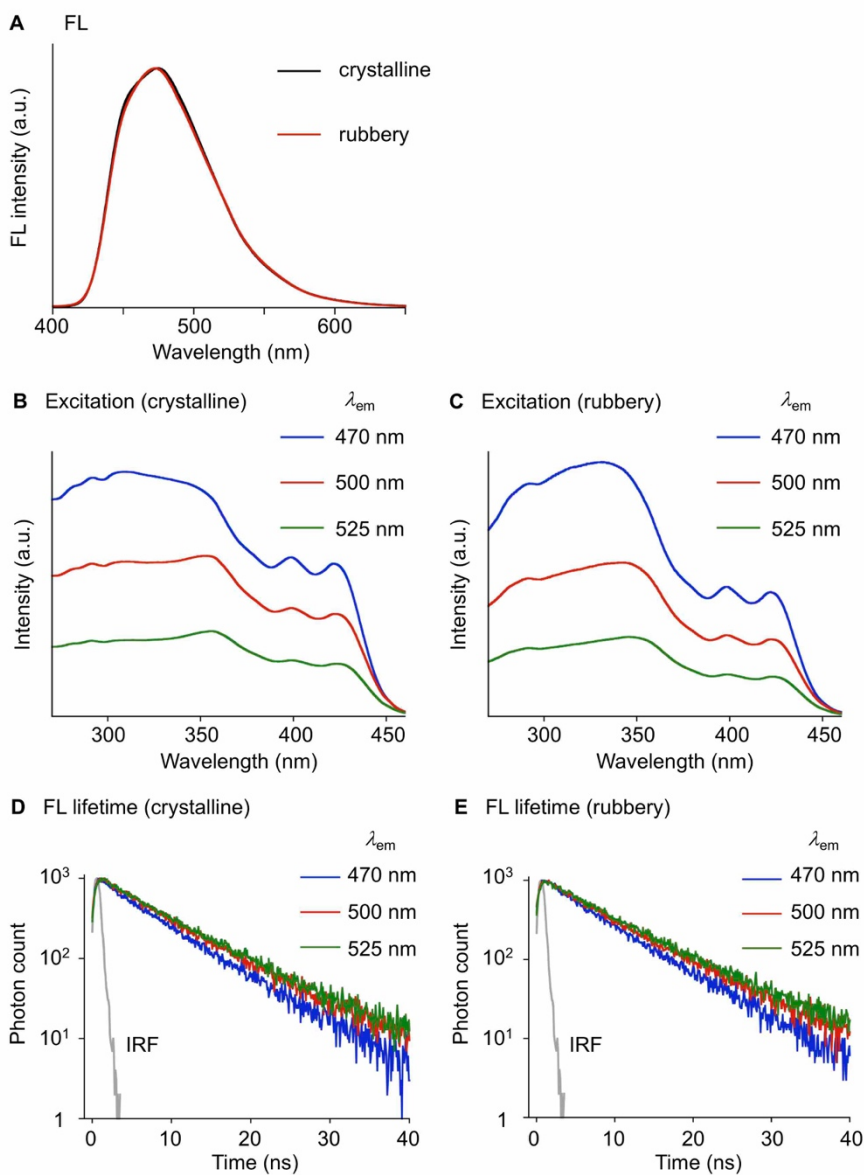


**Fig. S32.** (A) FL spectra of crystalline and rubbery **PU2(0.10)**.  $\lambda_{\text{ex}} = 365$  nm. Excitation spectra of (B) crystalline and (C) rubbery **PU2(0.10)**. FL decay profiles of (D) crystalline and (E) rubbery **PU2(0.10)**.

**Table S29.** Photophysical constants of **PU2(0.10)**.  $\lambda_{\text{ex}} = 365$  nm.

	$\lambda_{\text{em}}$ (nm)	$\chi^2$	$\tau_{\text{FL}}$ (ns)	$\tau_1$ (ns)	$\tau_2$ (ns)	$A_1$	$A_2$
crystalline	470	1.10	6.7	6.8	7.0	36	98
	500	1.04	8.0	4.7	9.4	55	63
	525	1.11	8.3	4.7	9.2	39	76
rubbery	470	1.05	7.1	3.8	7.8	37	86
	500	1.07	8.3	5.1	9.5	49	71
	525	1.24	8.8	5.0	10.0	46	73

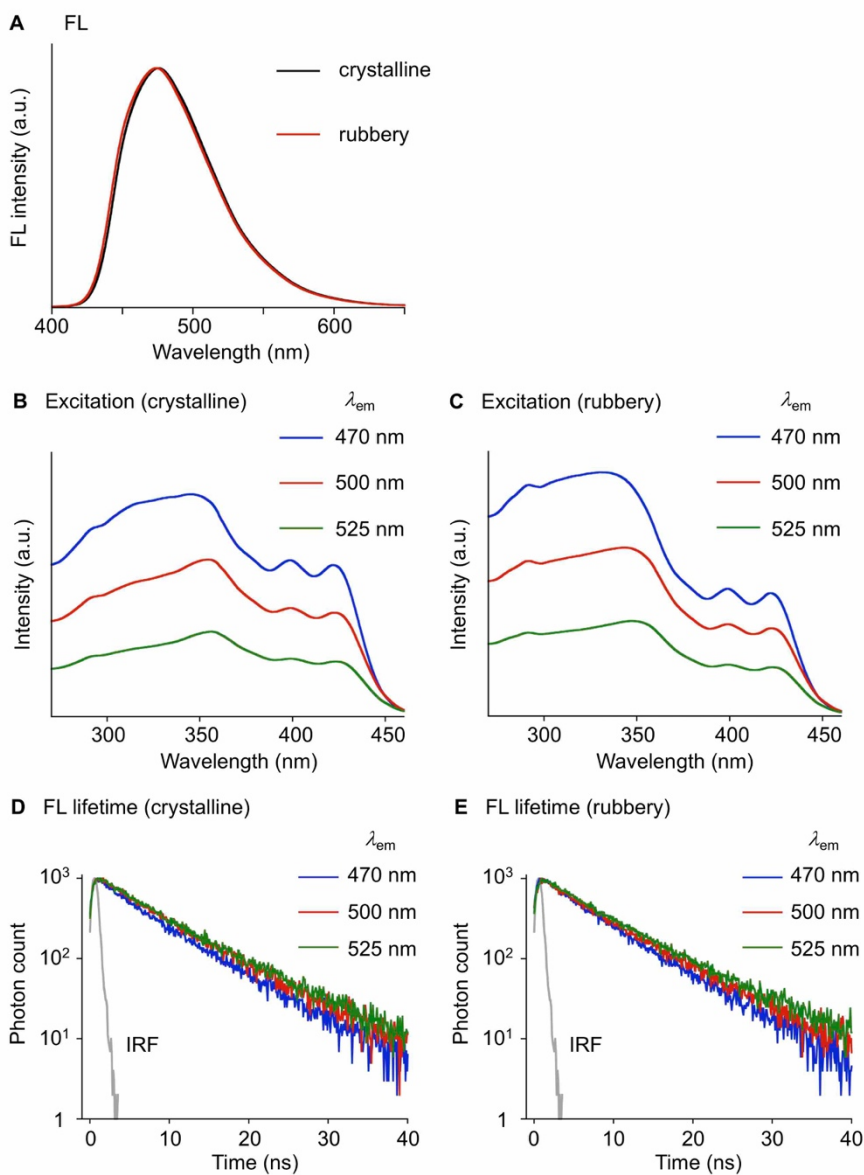


**Fig. S33.** (A) FL spectra of crystalline and rubbery **PU2(0.13)**.  $\lambda_{\text{ex}} = 365$  nm. Excitation spectra of (B) crystalline and (C) rubbery **PU2(0.13)**. FL decay profiles of (D) crystalline and (E) rubbery **PU2(0.13)**.

**Table S30.** Photophysical constants of **PU2(0.13)**.  $\lambda_{\text{ex}} = 365$  nm.

	$\lambda_{\text{em}}$ (nm)	$\chi^2$	$\tau_{\text{FL}}$ (ns)	$\tau_1$ (ns)	$\tau_2$ (ns)	$A_1$	$A_2$
crystalline	470	1.16	7.0	3.6	7.9	42	74
	500	1.24	7.5	2.8	8.1	33	91
	525	1.13	7.9	3.5	8.7	36	86
rubbery	470	1.01	6.9	3.0	7.5	33	91
	500	1.09	8.3	6.2	12.4	91	23
	525	1.23	8.2	3.9	9.0	36	85

## Real-time FL and absorption measurement of rubbery PU

We conducted a real-time FL and absorption measurement during a mechanical test using an Otsuka Electronics MULTI CHANNEL PHOTO DETECTOR MCPD-68000, which composed of an optical fiber and a detector equipped with a photodiode. FL spectra were recorded by a 0.8-s exposure with 2 accumulations (at 1.6-s intervals). Absorption spectra were recorded on the same photodetector by a 1.6-s exposure with 2 accumulations (at 3.2-s intervals). Reference light (initial strength  $I_0$ ) was measured using a 100 W light source at a constant distance before tensile testing. Then, a PU specimen was allowed to be tested as the specimen crossed over a light path. Obtained light strength  $I$  was transformed into absorbance  $A$ .

$$A = -\log\left(\frac{I}{I_0}\right)$$

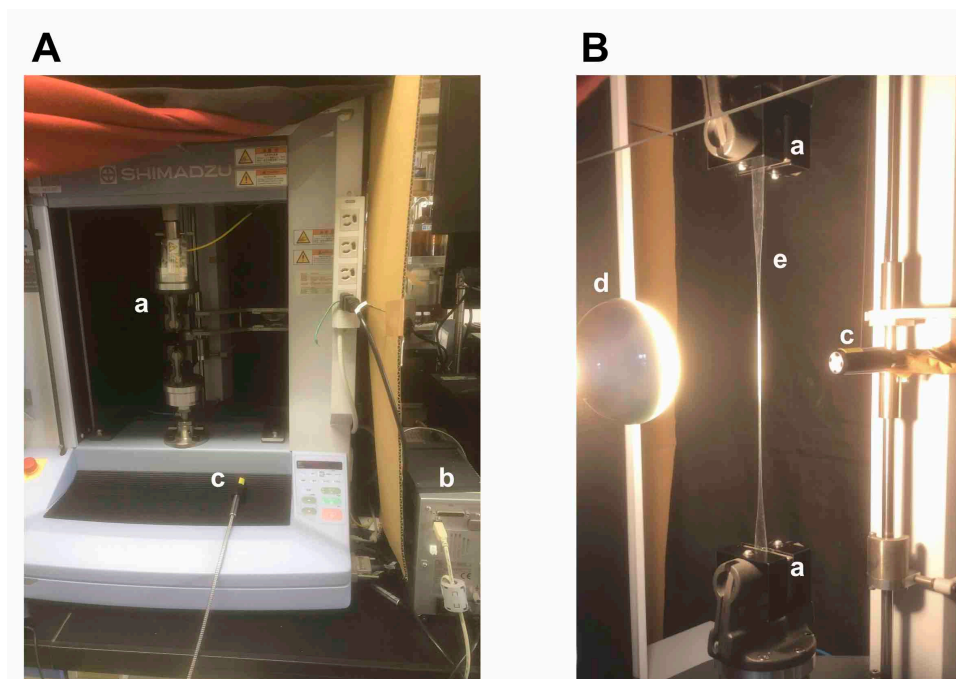


**Fig. S34.** Experimental setup of real-time FL (A) and absorption (B) measurement.

- a:** Upper and lower chuck of a tensile testing machine to hold a specimen.
- b:** Multi-channel detector.
- c:** Tip of the detector that is connected to **b** through an optical fiber.
- d:** 100-W tungsten light.
- e:** PU specimen.

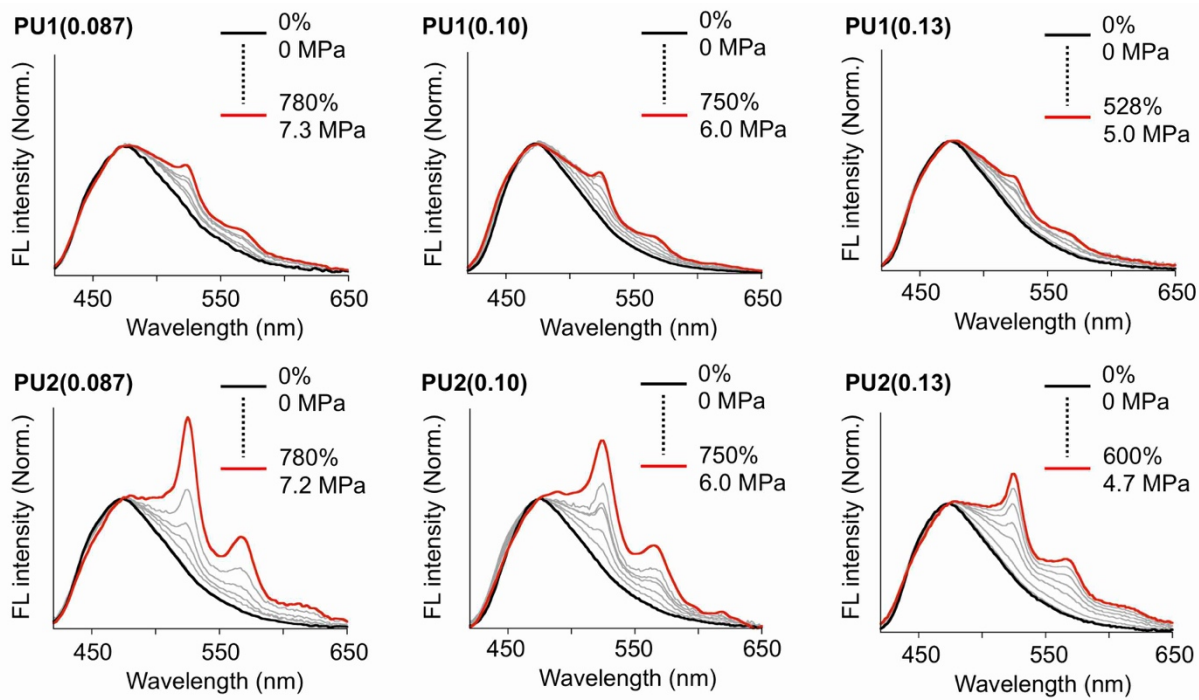


**Fig. S35.** FL spectral changes of rubbery PUs. Normalized at 474 nm.  $\lambda_{ex} = 365$  nm.

## FL spectral changes for loading–unloading cycle testing

In order to reveal that the mechanoresponse was induced by external force in a real-time and repeated manner, we conducted ratiometric FL analysis during the loading–unloading mechanical testing. Fig. S36 shows results of the the cycle test.

Start → **a**: Loading up to 300% strain (purple line).

**a** → **b**: Unloading up to stress of 0.1 MPa (blue line).

**b** → **c**: Loading up to 600% strain (green line).

**c** → **d**: Unloading up to stress of 0.1 MPa (orange line).

**d** → **e**: Loading up to break (red line).

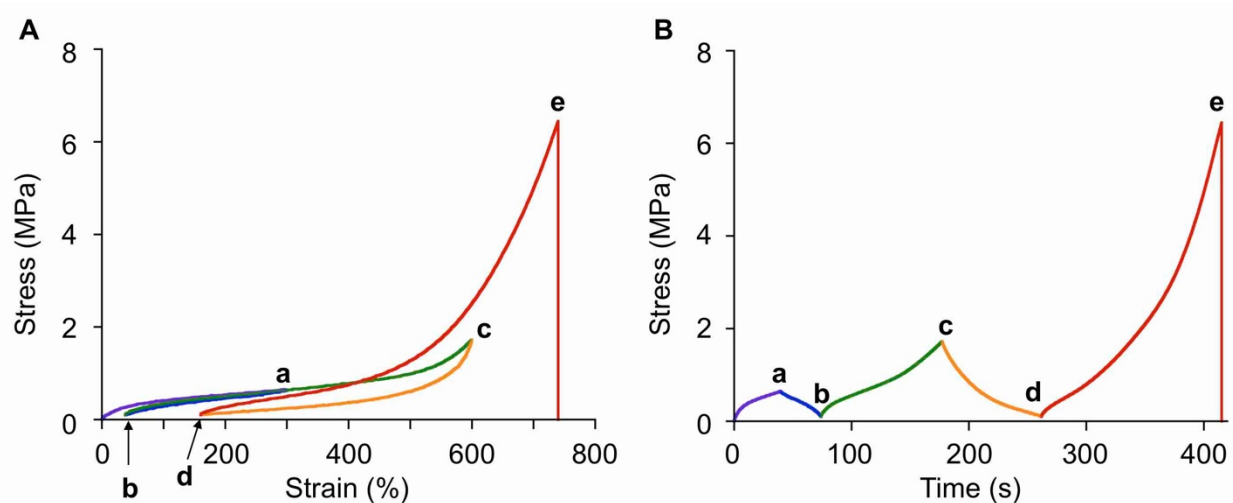


**Fig. S36.** Stress as a function of (A) strain and (B) time for cycle testing.

## Estimation of planarized FLAP mechanophores

We estimated that forcibly planarized FLAP mechanophores based on the FL spectral changes. Fig. S37 shows FL spectra as a function of wavenumber (energy scale). Before extension, FL from the V-shaped geometry was observed. Upon extension, FL spectral changes depicting a green region was observed, which corresponding to the FL from the planar geometry. Based on the area of the spectral changes, we calculated the percentage of forcibly planarized FLAP mechanophores. Although, the molecules to be photoexcited varied over the conformational coordination as shown in Fig. 3 (main text), we employed the representative structures for estimation of V-shaped and planar geometries as  $S_0$  optimized and threshold geometries, respectively.

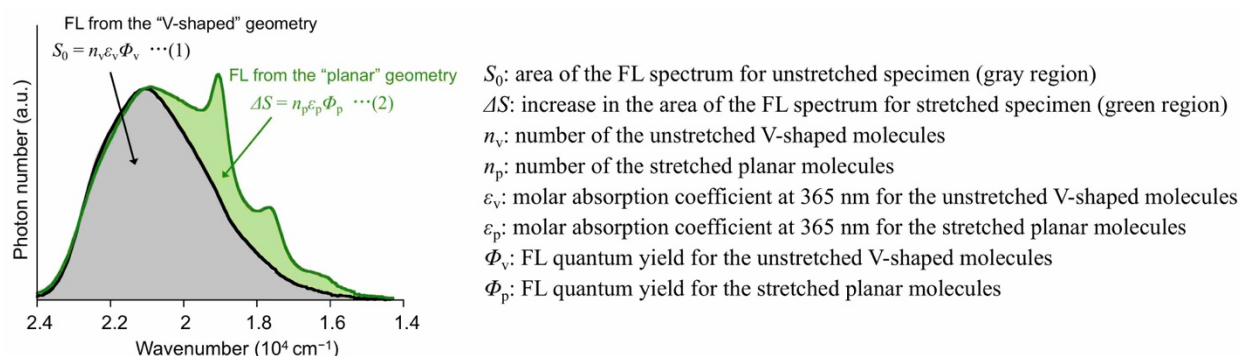


**Fig. S37.** Schematic illustration for estimation of forcibly planarized FLAP mechanophores using FL spectral changes.

The proportion of the planarized FLAP mechanophores can be expressed using (1) and (2) as follows,

$$\frac{n_p}{n_p + n_v} = \frac{1}{1 + \frac{n_v}{n_p}} = \frac{1}{1 + \frac{\epsilon_p \Phi_p S_0}{\epsilon_v \Phi_v \Delta S}} = \frac{1}{1 + \frac{2S_0}{\Delta S}} \quad (3)$$

Here, we estimated that  $\epsilon_p = 140000 \text{ M}^{-1} \text{ cm}^{-1}$  for  $S_0$  threshold geometry and  $\epsilon_v = 70000 \text{ M}^{-1} \text{ cm}^{-1}$  for  $S_0$  optimized geometry of **FLAP1'** and **FLAP2'** at the TD PBE0/6-31+G(d) level of theory. And  $\Phi_v$  is the same extent to  $\Phi_p$  for **PU1** and **PU2** ( $\Phi_v \sim \Phi_p$ ), because  $\Phi_v$  was determined to be  $\sim 0.3$  (Table S9), and  $\Phi_p$  was also estimated to be 0.3 using the results (monomer **FLAP1** and **FLAP2**) in the solution (Table S1).

## FL measurement for PU physically doped with FLAP

In order to verify FL changes were induced by force, we conducted the same experiment for **PU3** that is physically doped with **FLAP3** (*S4*) made from the same composition of PU with crosslinking density of 0.10. The synthesized **PU3** showed similar mechanical and photophysical properties to those of **PU0–PU2**, but no characteristic FL enhancement was observed under mechanical testing.

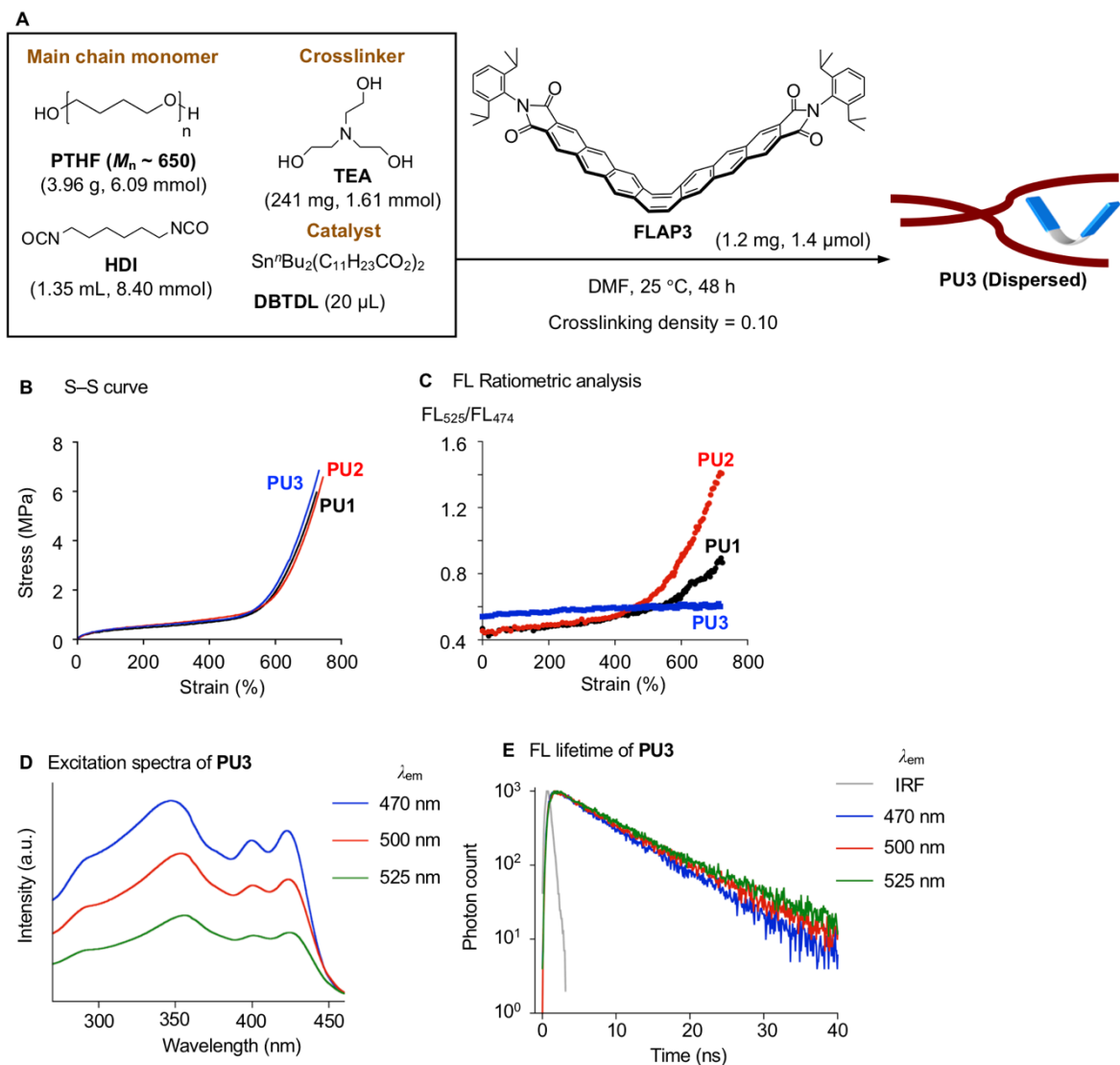


**Fig. S38.** (A) Synthesis of **PU3**. (B) S–S curves of **PU1–PU3**. Strain rate:  $0.17 \text{ s}^{-1}$ . (C) FL ratiometric analysis of **PU1–PU3**. (D) Excitation spectra of **PU3**. (E) FL lifetime profiles of **PU3**.

**Table S31.** Photophysical constants of **PU3**.  $\lambda_{\text{ex}} = 365 \text{ nm}$ .

$\lambda_{\text{em}}$ (nm)	$\chi^2$	$\tau_{\text{FL}}$ (ns)	$\tau_1$ (ns)	$\tau_2$ (ns)	$A_1$	$A_2$
470	1.07	7.1	3.2	7.6	25	96
500	1.10	8.8	7.0	16.5	104	10
525	1.03	9.4	7.4	16.9	102	12

## Real-time FL measurement of crystalline PU

Crystalline samples, which had been stored at room temperature for more than 2 days, were allowed to be tested. Tensile test and FL measurement were conducted under the same condition as in rubbery samples. The degree of crystallization was more pronounced in the smaller cross-linking density.

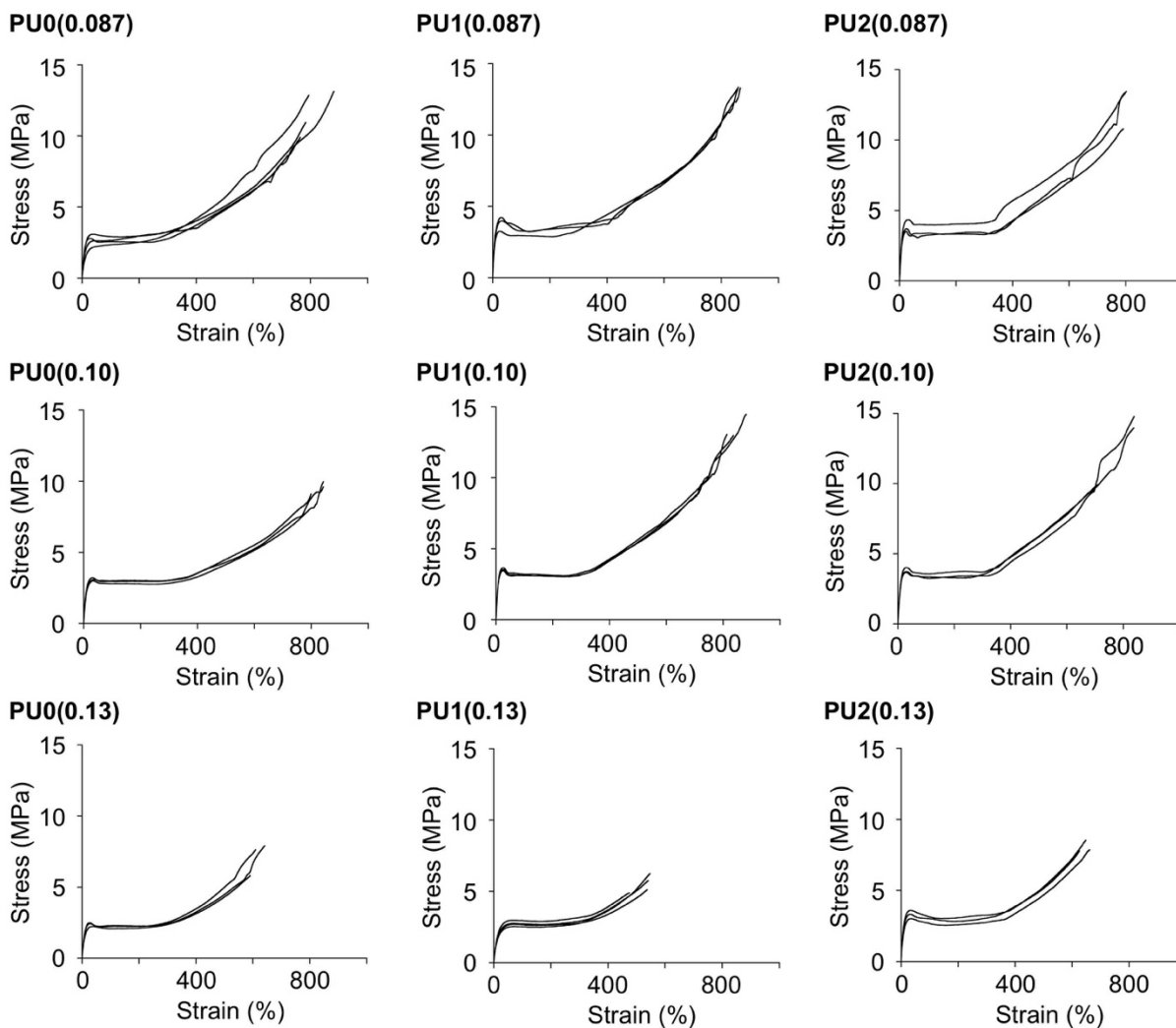


**Fig. S39.** S-S curves of crystalline PUs.

**Table S32.** Summary of mechanical properties of uniaxial tests of crystalline PU.

	Strain at break (%)	Stress at break (MPa)	Toughness at break (MJ m <sup>-3</sup> )	Young's modulus (MPa)
<b>PU0(0.087)</b>	807 ± 52	11.7 ± 1.6	40.1 ± 5.3	18 ± 4
<b>PU1(0.087)</b>	862 ± 5	13.3 ± 0.1	48.9 ± 0.9	30 ± 2
<b>PU2(0.087)</b>	797 ± 5	12.5 ± 1.5	46.0 ± 5.0	30 ± 3
<b>PU0(0.10)</b>	829 ± 25	9.6 ± 0.4	36.5 ± 1.4	22 ± 1
<b>PU1(0.10)</b>	844 ± 34	13.5 ± 0.8	47.7 ± 4.0	28 ± 1
<b>PU2(0.10)</b>	797 ± 72	12.9 ± 2.6	46.6 ± 8.5	28 ± 2
<b>PU0(0.13)</b>	614 ± 26	7.1 ± 1.1	19.9 ± 2.4	17 ± 2
<b>PU1(0.13)</b>	525 ± 34	5.5 ± 0.6	16.7 ± 1.1	15 ± 1
<b>PU2(0.13)</b>	645 ± 18	8.1 ± 0.4	25.7 ± 1.8	24 ± 3

Average ± standard deviation of 3–4 specimens was shown.

FL spectral changes for crystalline PU specimens, are shown in Fig. S40. Due to higher mechanical performance of crystalline specimens than rubbery ones, appearance of the green FL region was more pronounced. Here PU2, which reflected the stress-concentration in the vicinity of cross-linking points, showed more pronounced FL spectral enhancement in the green region.

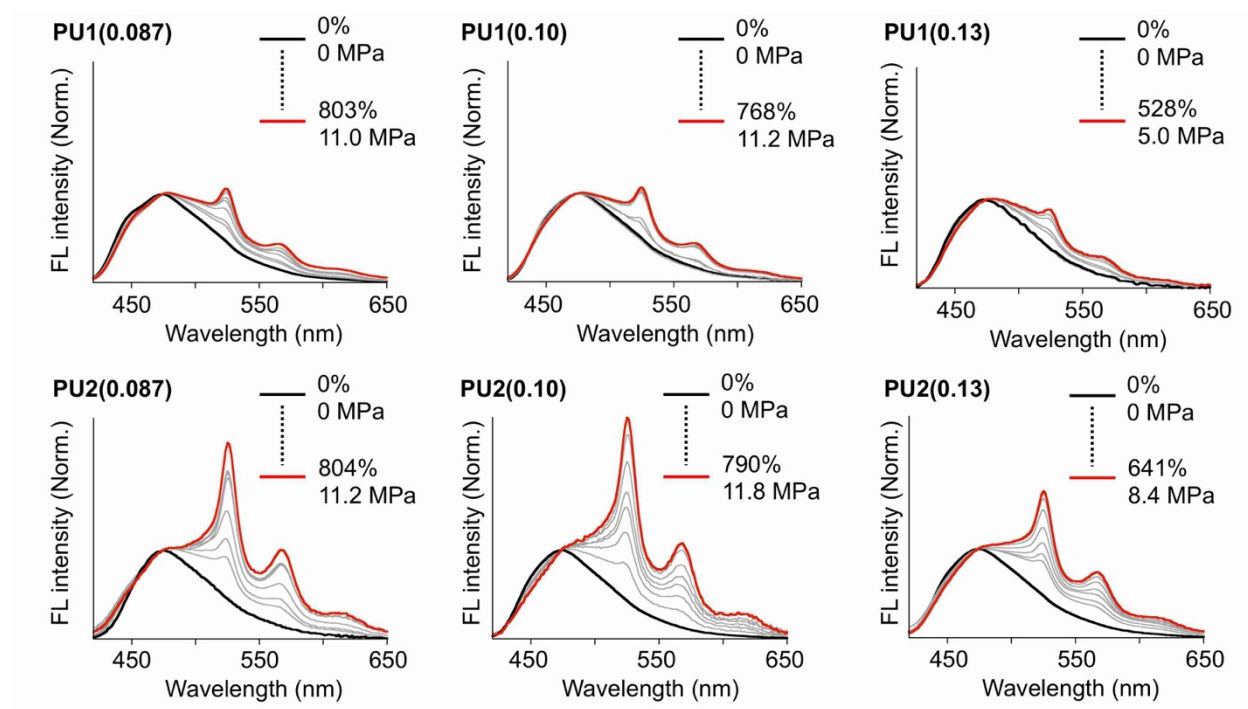


**Fig. S40.** FL spectral changes of crystalline PUs. Normalized at 474 nm.  $\lambda_{\text{ex}} = 365$  nm.

## Inhomogeneous FL spectral changes of crystalline PU in the region of necking and drawing

Although its more pronounced mechanoresponse of crystalline specimens than rubbery ones, FL changes under tensile test was not homogeneous in the region of necking and drawing. These inhomogeneities were analyzed under a fluorescent microscope by using a FLAP-doped PC in the following section.

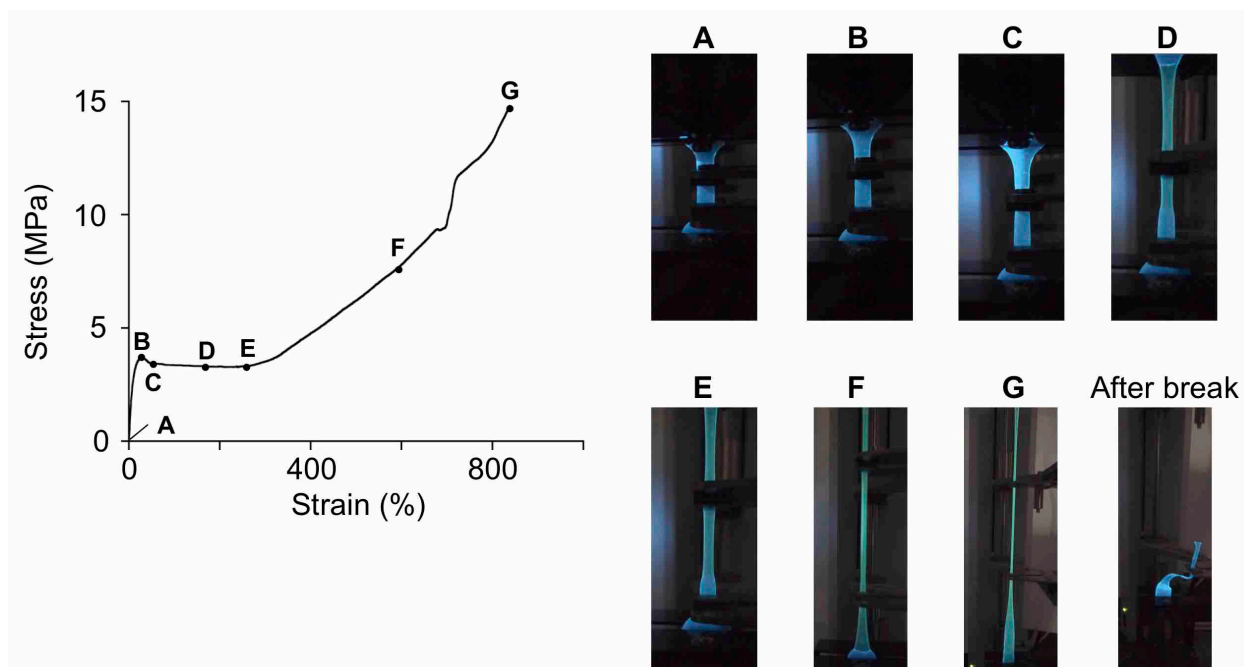


**Fig. S41.** Photographs of FL changes of crystalline PU2(0.10) under tensile test.

## NMR spectra of new compounds

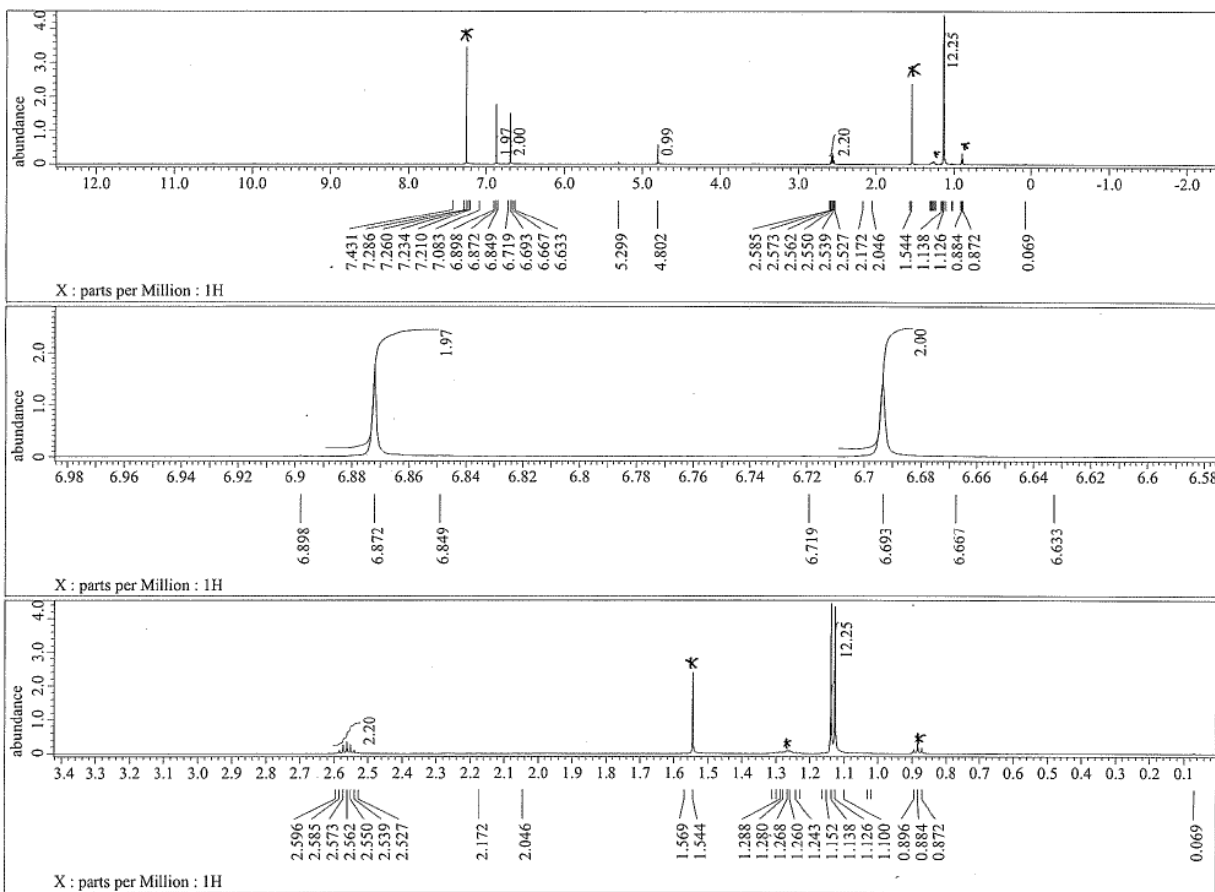


**Fig. S42.**  $^1\text{H}$  NMR spectra of S1 in  $\text{CDCl}_3$  at  $25^\circ\text{C}$ . The peaks marked with \* indicate residual solvents.

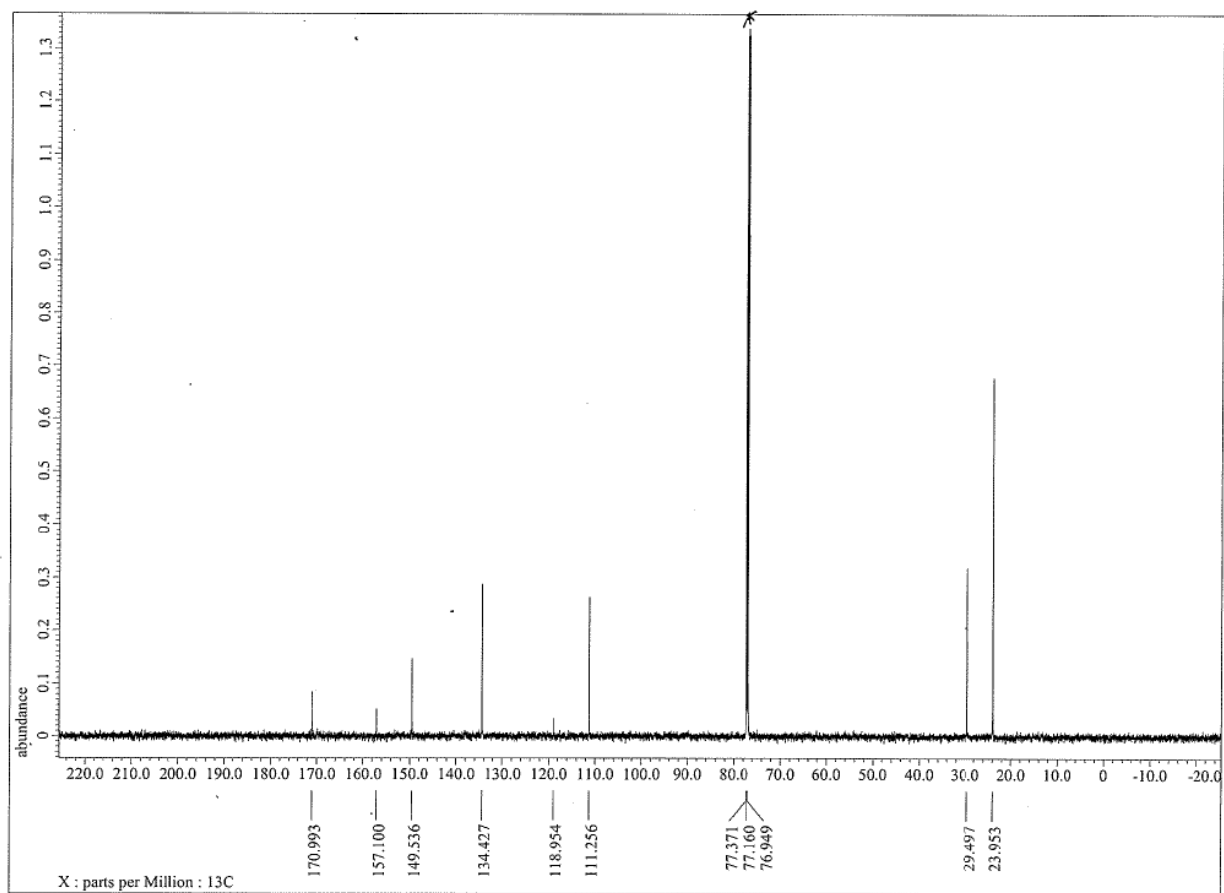


**Fig. S43.**  $^{13}\text{C}$  NMR spectra of **S1** in  $\text{CDCl}_3$  at 25 °C. The peak marked with \* indicates residual solvents.



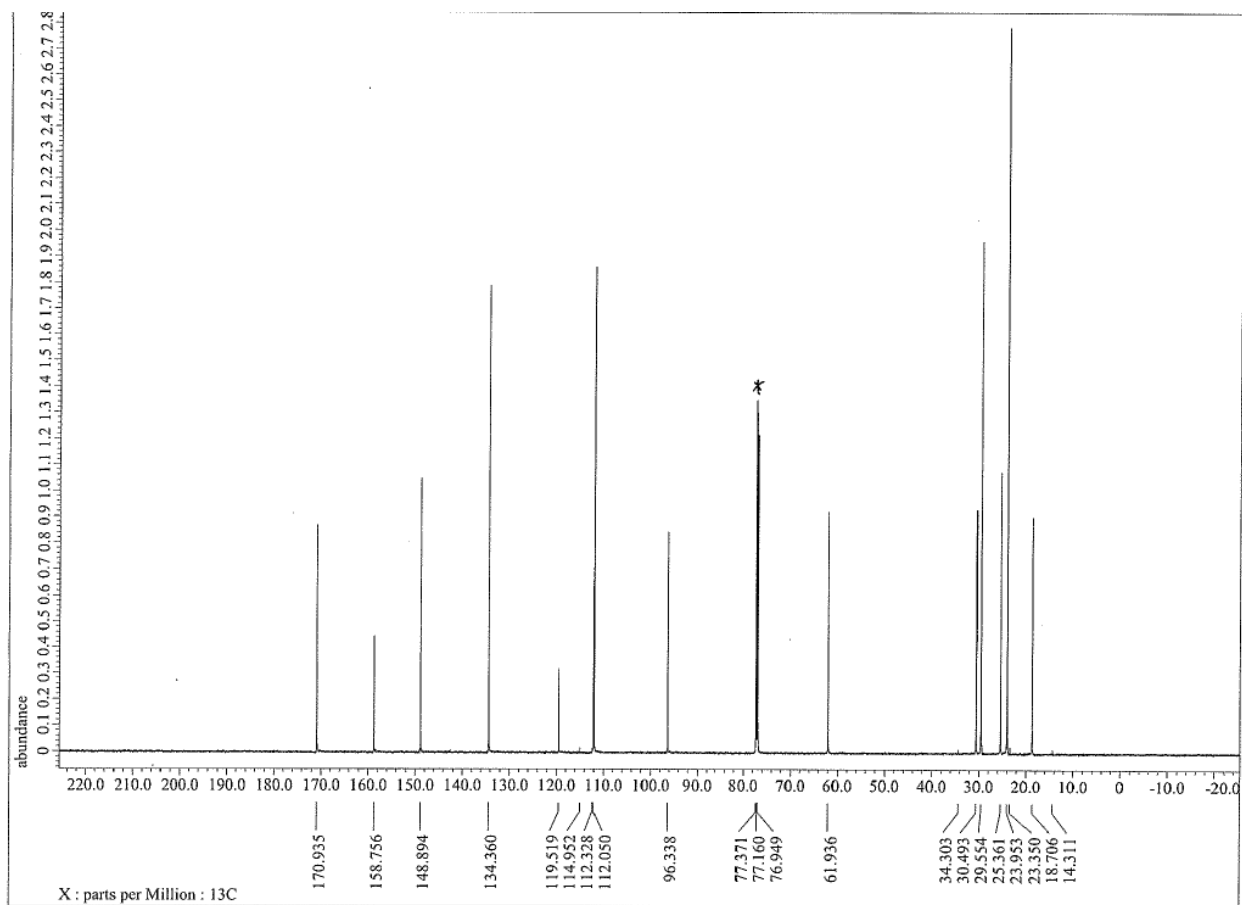


**Fig. S45.**  $^{13}\text{C}$  NMR spectra of **S2** in  $\text{CDCl}_3$  at 25 °C. The peak marked with \* indicates residual solvents.

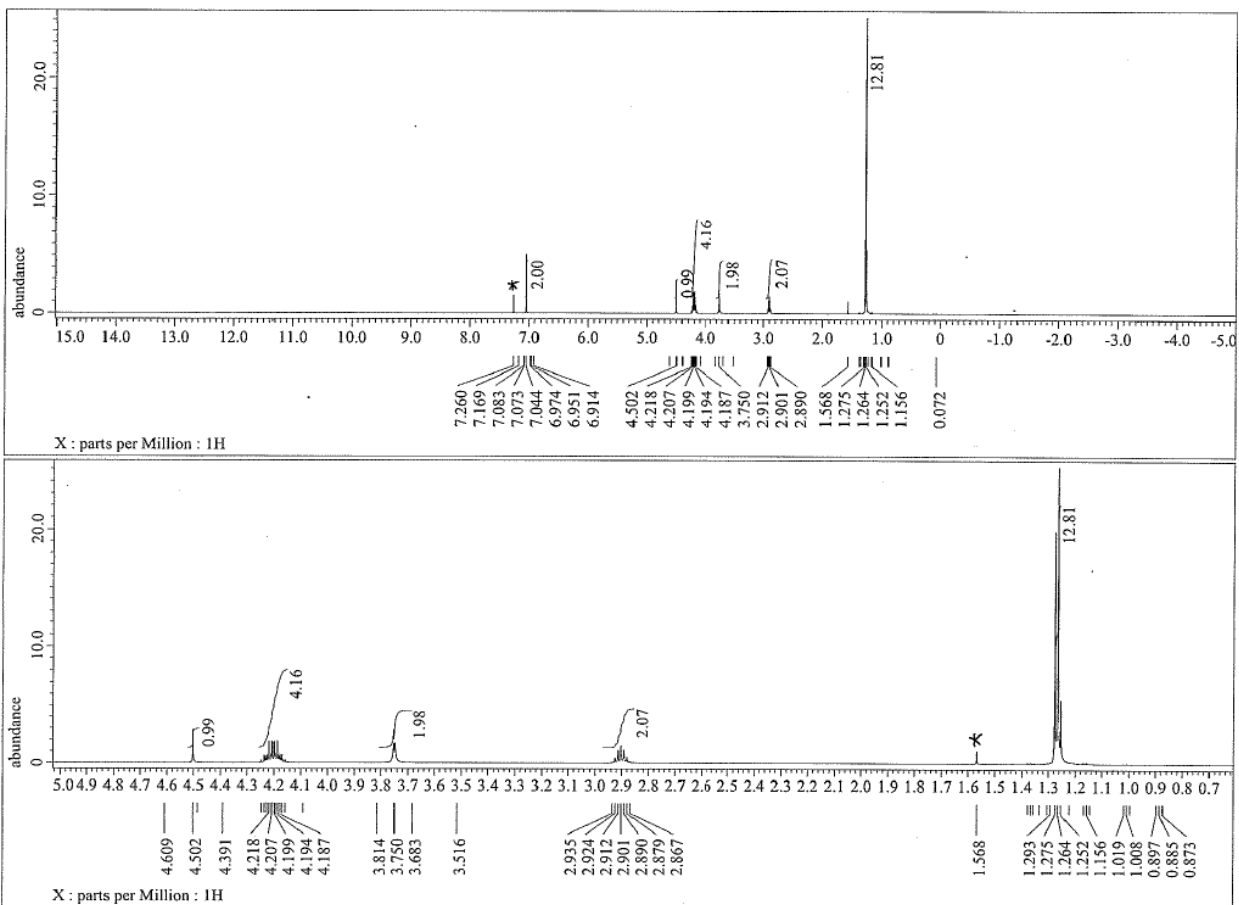


**Fig. S46.**  $^1\text{H}$  NMR spectra of S3 in  $\text{CDCl}_3$  at  $25^\circ\text{C}$ . The peaks marked with \* indicate residual solvents.

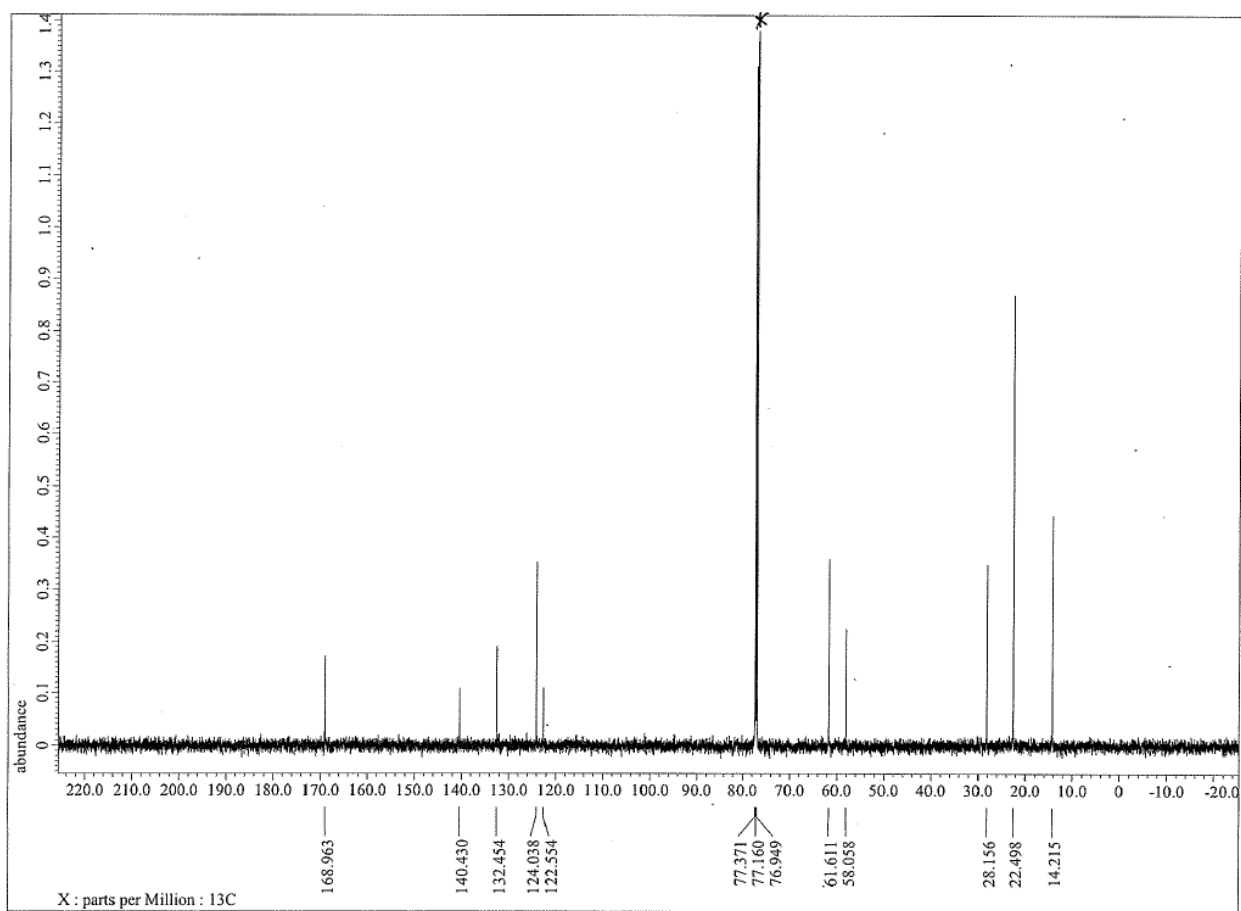


**Fig. S47.**  $^{13}\text{C}$  NMR spectra of S3 in  $\text{CDCl}_3$  at  $25\text{ }^\circ\text{C}$ . The peak marked with \* indicates residual solvents.

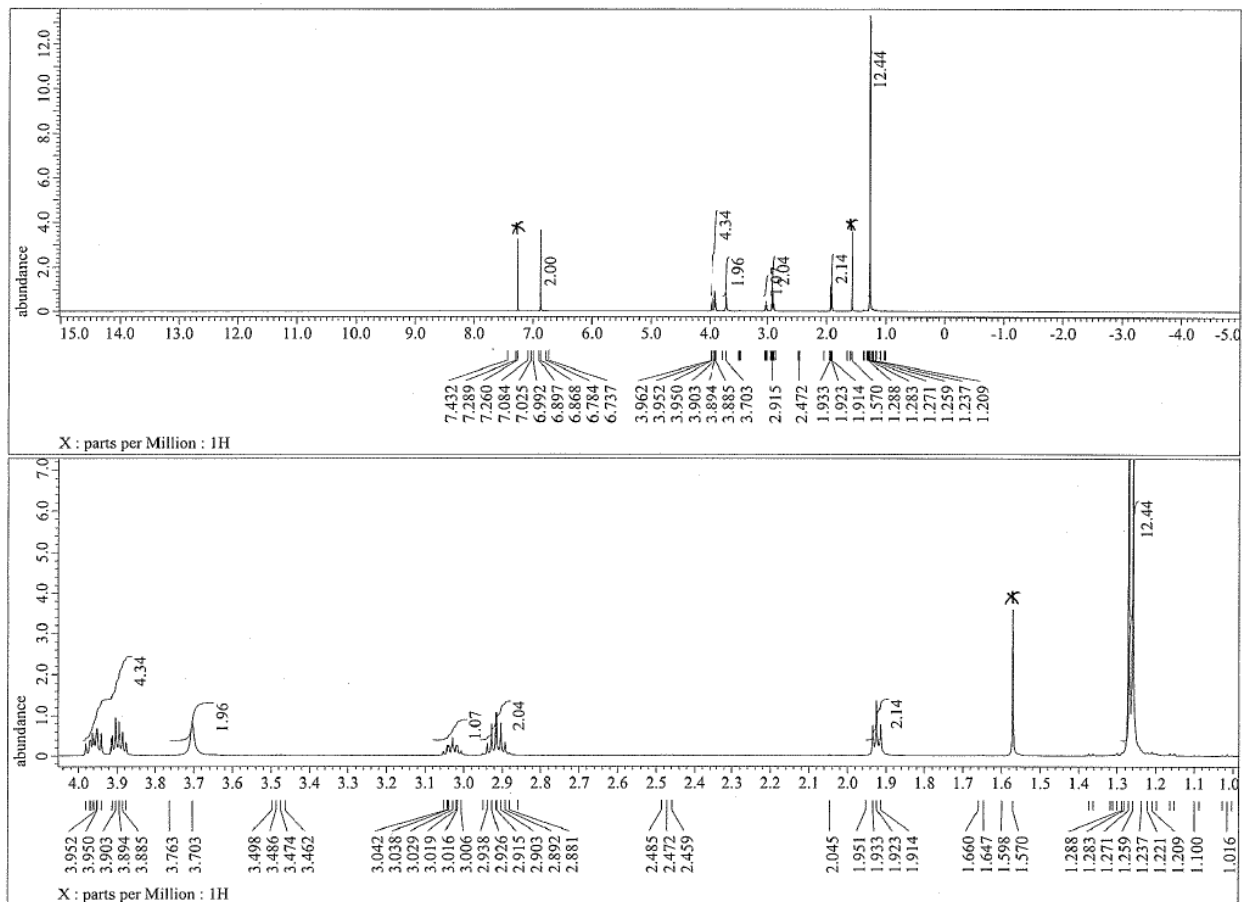


**Fig. S48.** <sup>1</sup>H NMR spectra of S4 in CDCl<sub>3</sub> at 25 °C. The peaks marked with \* indicate residual solvents.

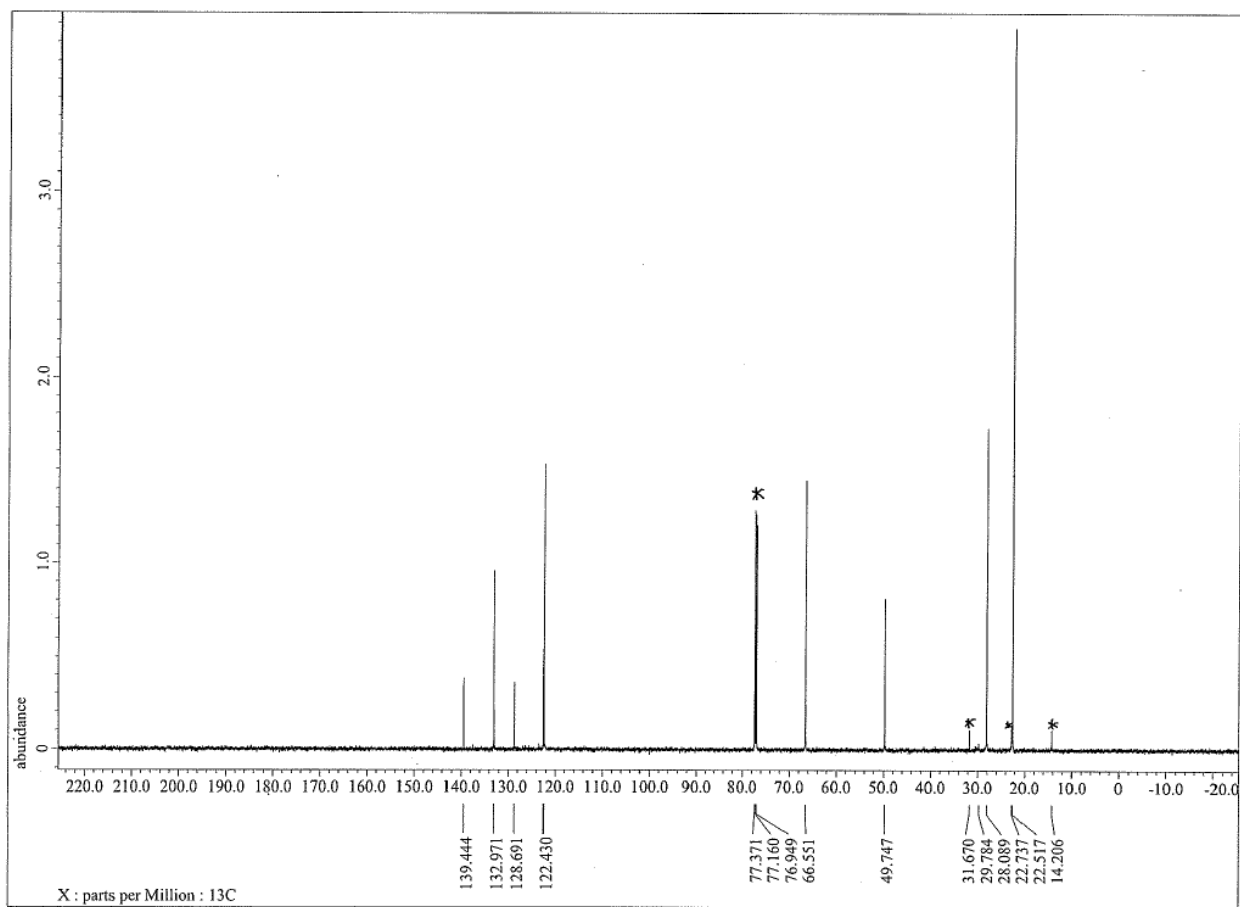


**Fig. S49.** <sup>13</sup>C NMR spectra of **S4** in CDCl<sub>3</sub> at 25 °C. The peaks marked with \* indicate residual solvents.

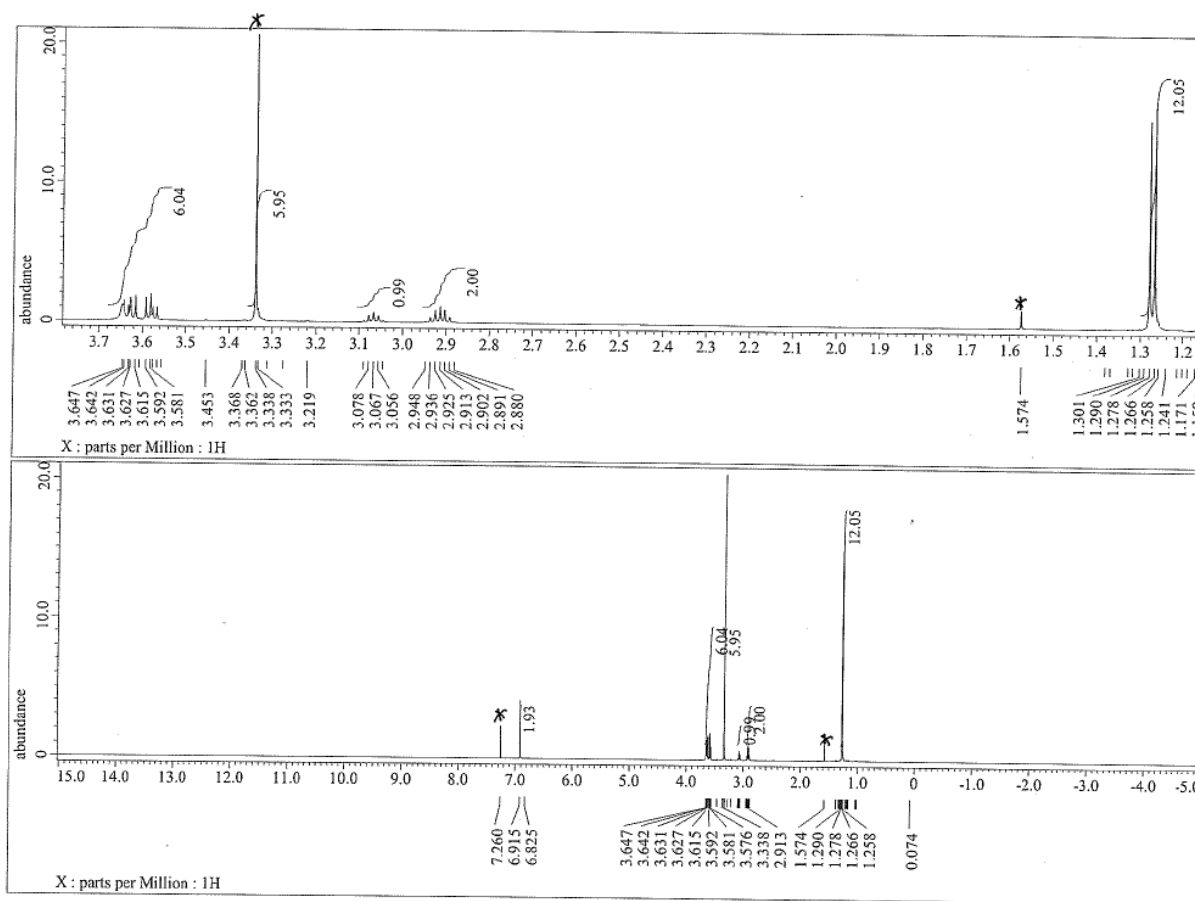


**Fig. S50.** <sup>1</sup>H NMR spectra of S5 in CDCl<sub>3</sub> at 25 °C. The peaks marked with \* indicate residual solvents.

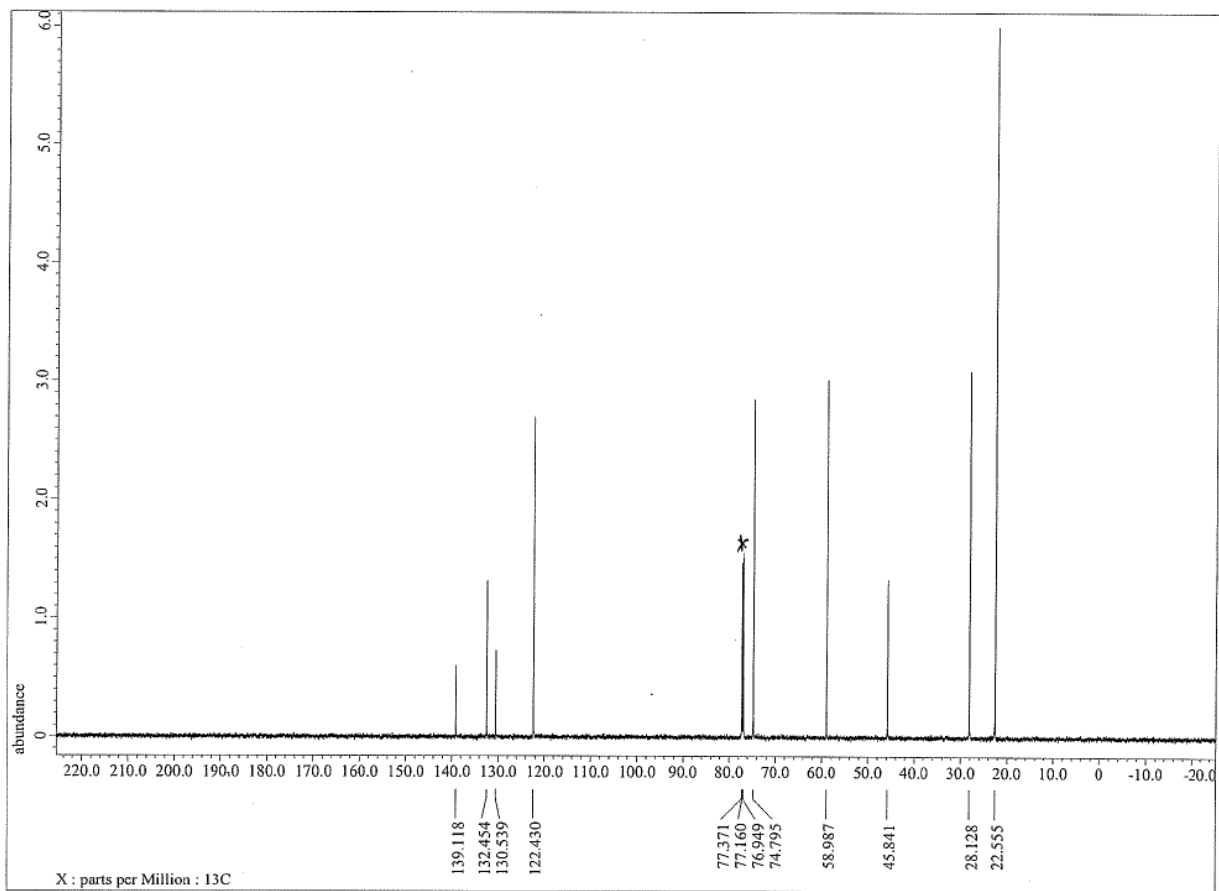


**Fig. S51.**  $^{13}\text{C}$  NMR spectra of **S5** in  $\text{CDCl}_3$  at 25 °C. The peak marked with \* indicates residual solvents.

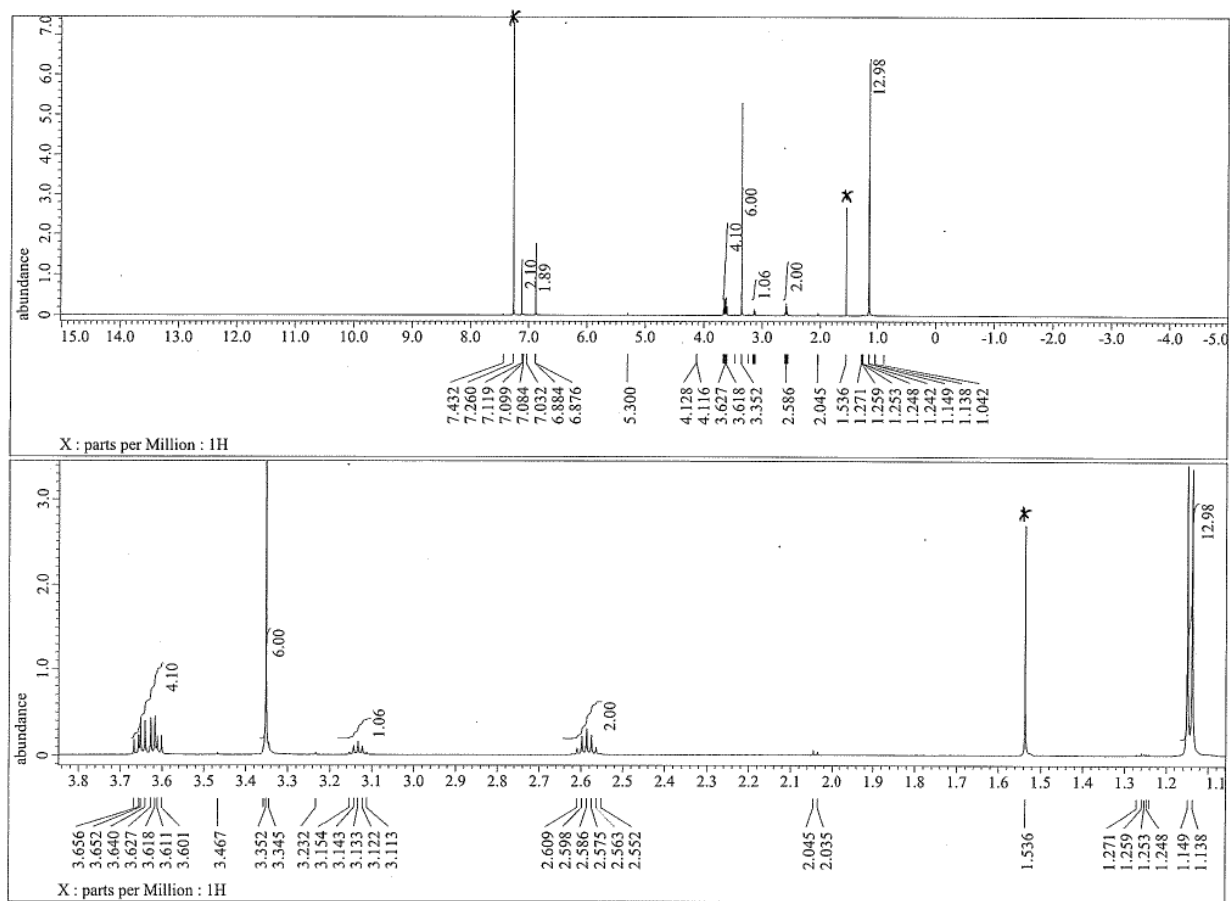


**Fig. S52.**  $^1\text{H}$  NMR spectra of S6 in  $\text{CDCl}_3$  at  $25\text{ }^\circ\text{C}$ . The peaks marked with \* indicate residual solvents.

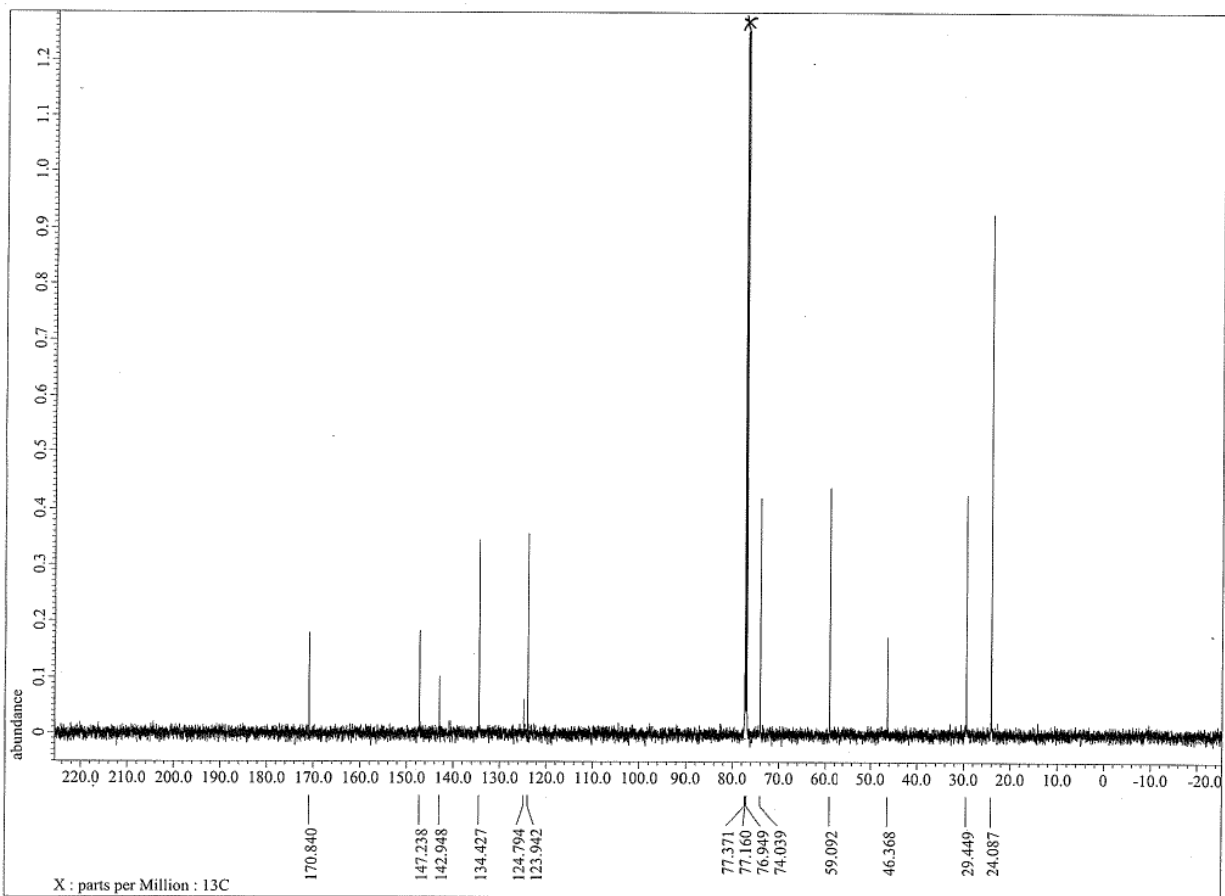


**Fig. S53.**  $^{13}\text{C}$  NMR spectra of **S6** in  $\text{CDCl}_3$  at  $25^\circ\text{C}$ . The peak marked with \* indicates residual solvents.

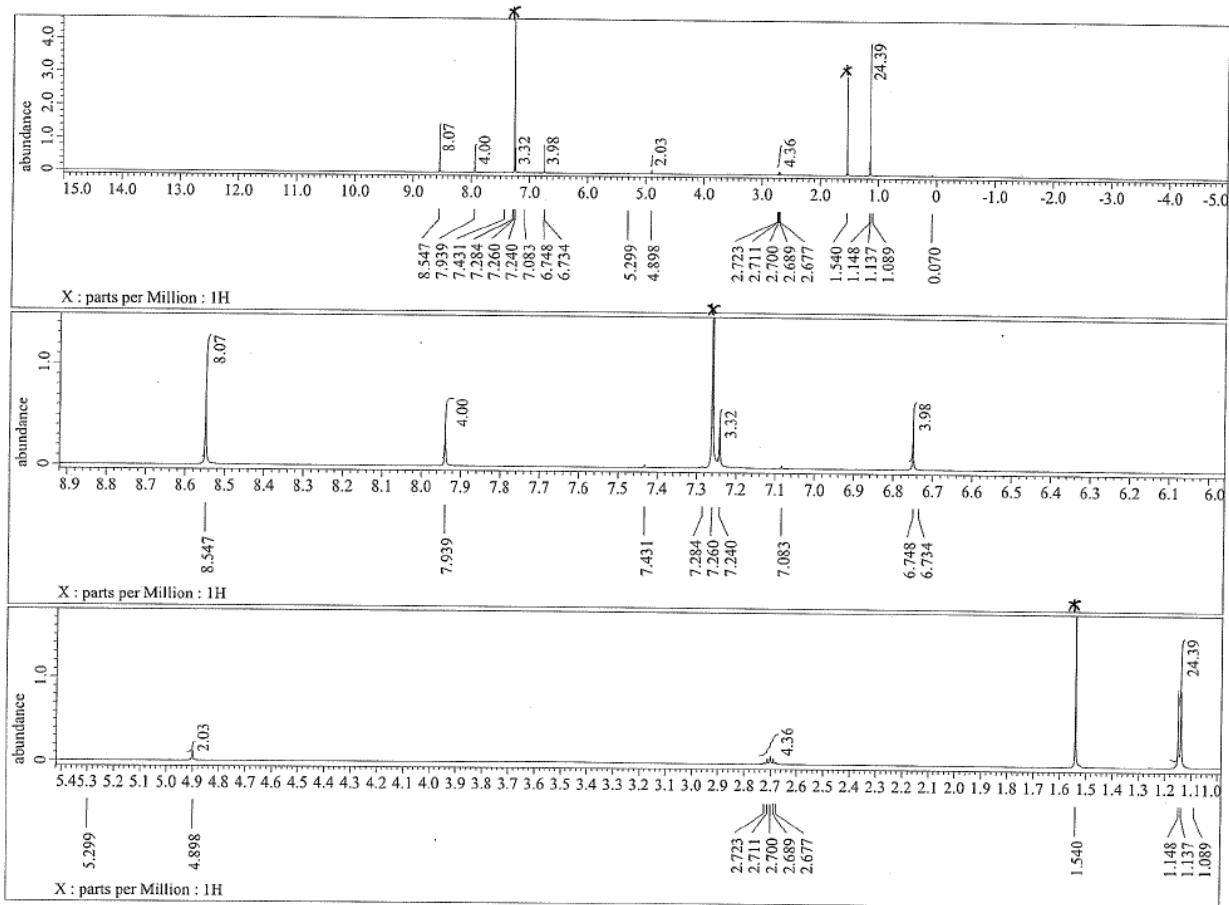


**Fig. S54.**  $^1\text{H}$  NMR spectra of FLAP1 in  $\text{CDCl}_3$  at  $25^\circ\text{C}$ . The peaks marked with \* indicate residual solvents.

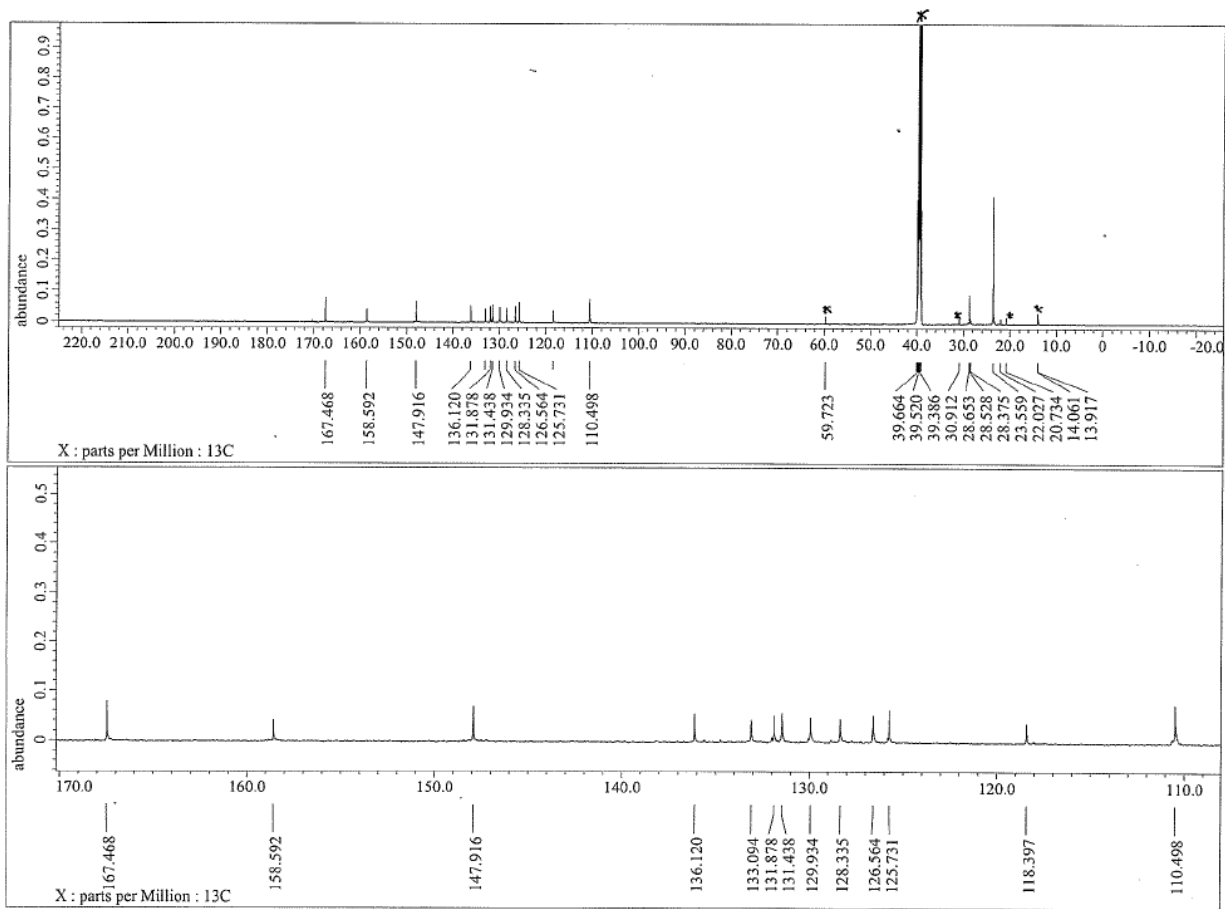


**Fig. S55.**  $^{13}\text{C}$  NMR spectra of FLAP1 in  $\text{DMSO}-d_6$  at  $25\text{ }^\circ\text{C}$ . The peaks marked with \* indicate residual solvents.

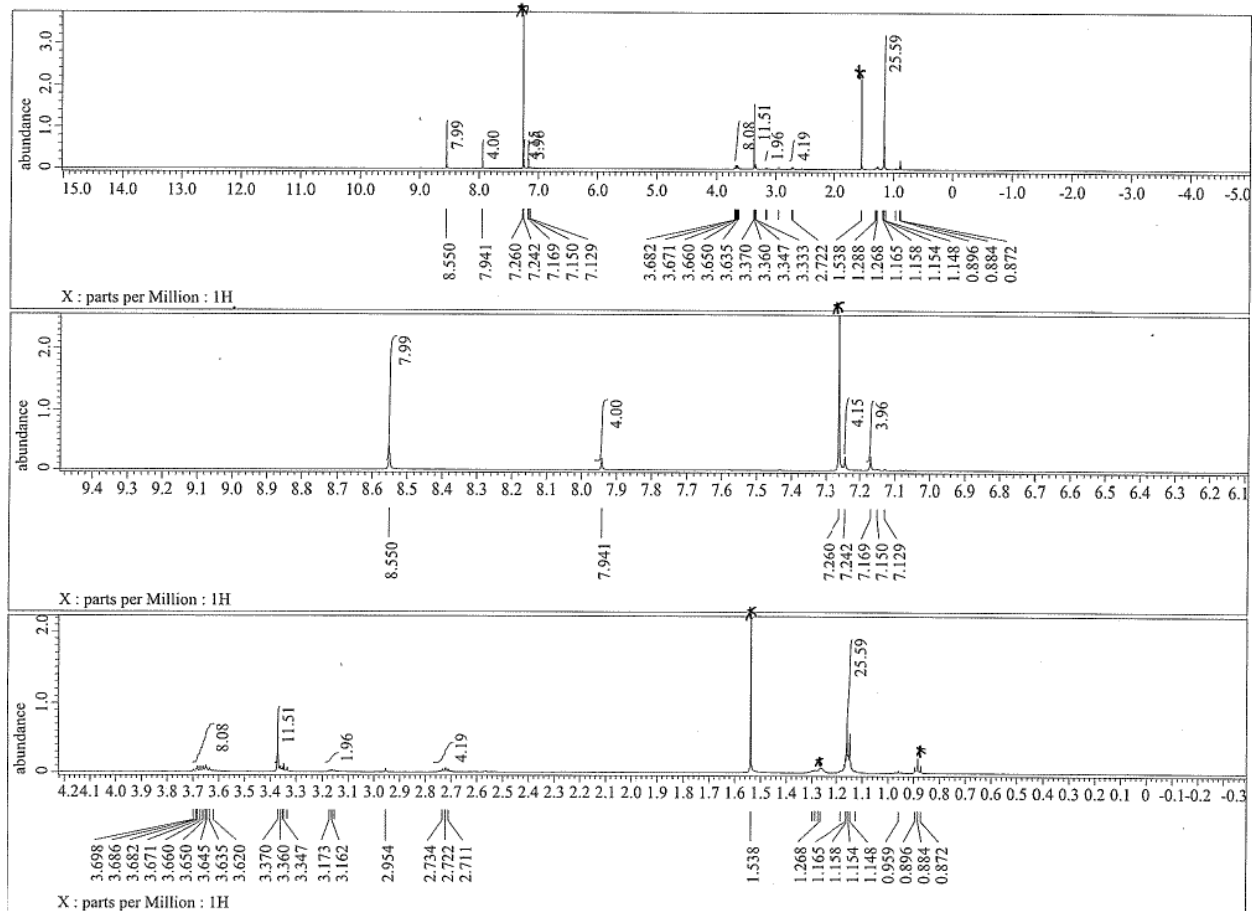


**Fig. S56.**  $^1\text{H}$  NMR spectra of **S8** in  $\text{CDCl}_3$  at  $25^\circ\text{C}$ . The peaks marked with \* indicate residual solvents.

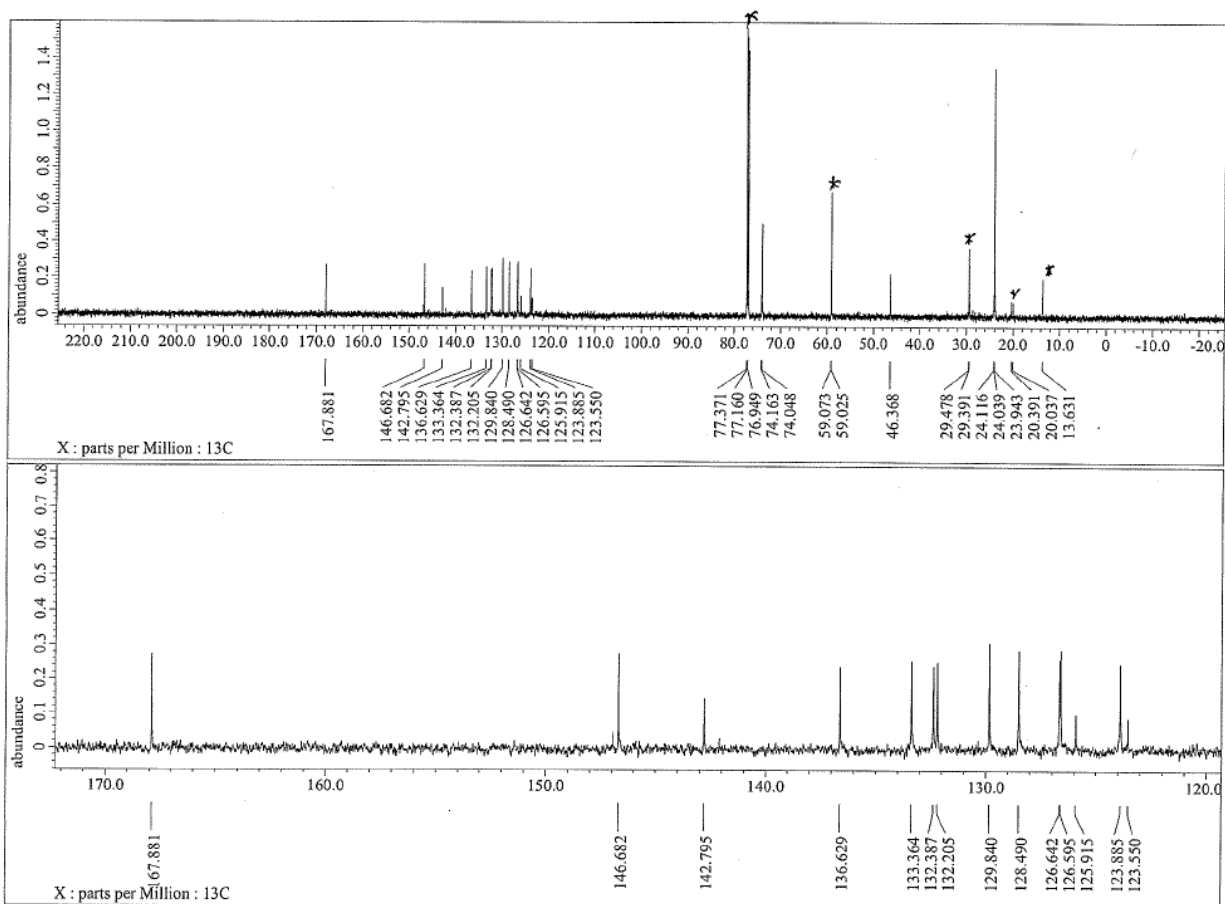


**Fig. S57.**  $^{13}\text{C}$  NMR spectra of S8 in  $\text{CDCl}_3$  at  $25^\circ\text{C}$ . The peaks marked with \* indicate residual solvents.

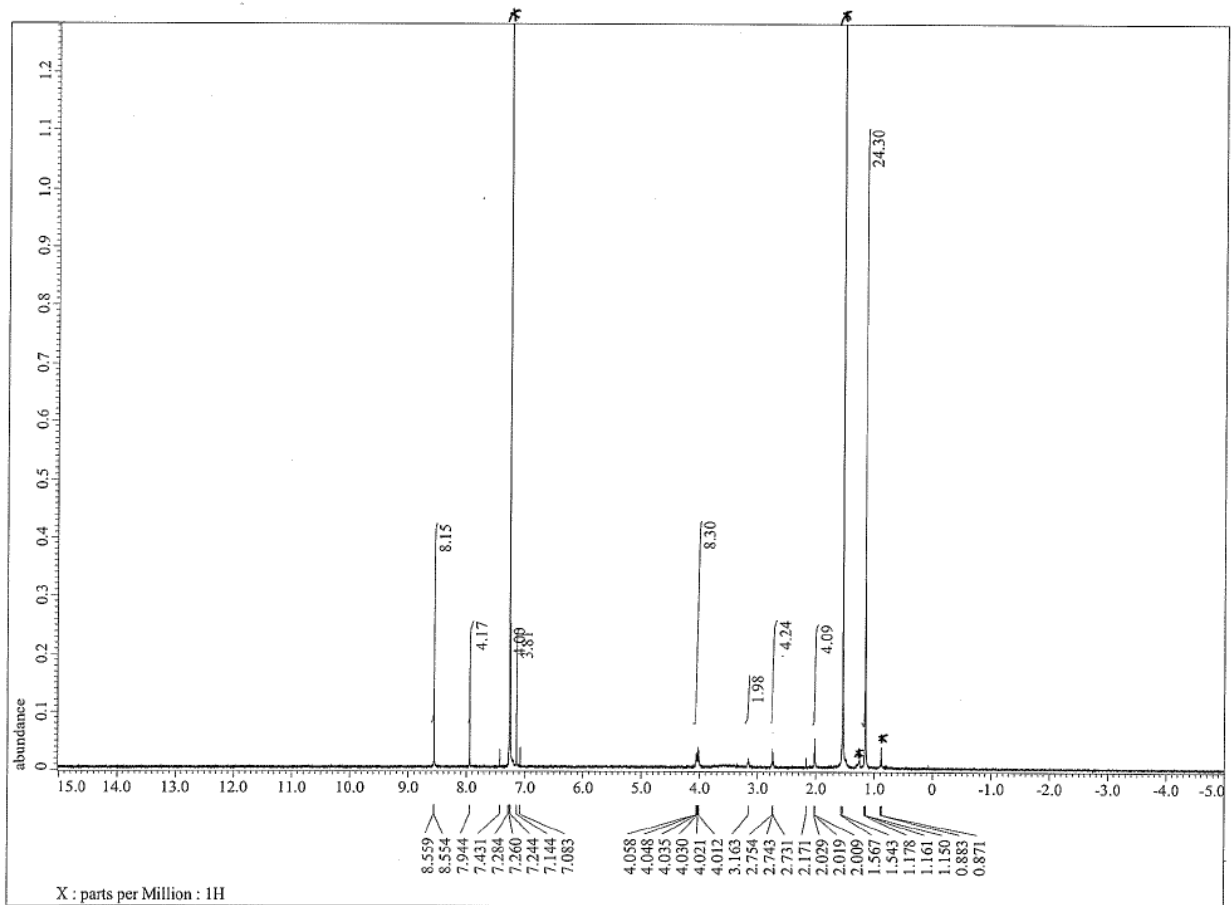


**Fig. S58.** <sup>1</sup>H NMR spectra of FLAP2 in CDCl<sub>3</sub> at 25 °C. The peaks marked with \* indicate residual solvents.

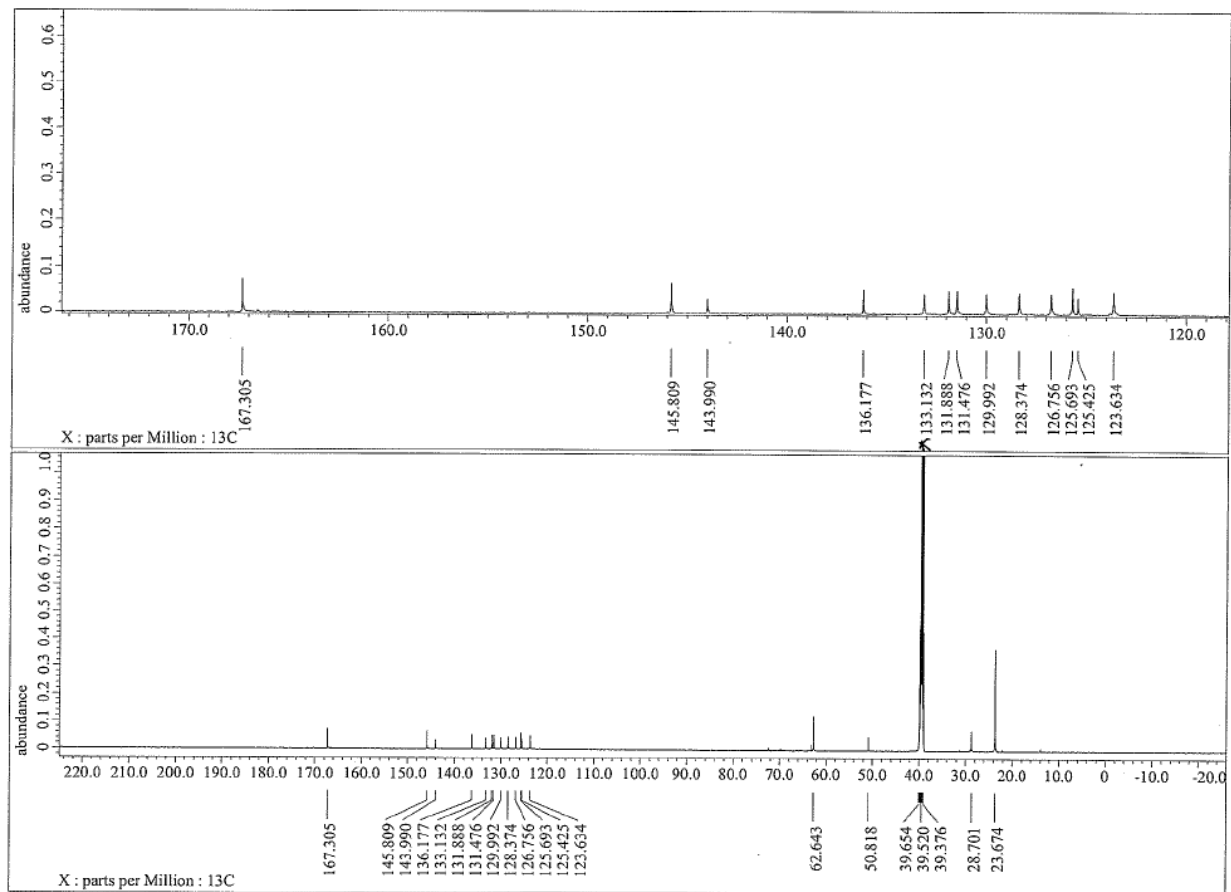


**Fig. S59.**  $^{13}\text{C}$  NMR spectra of FLAP2 in  $\text{DMSO-}d_6$  at  $25\text{ }^\circ\text{C}$ . The peak marked with \* indicates residual solvents.

## Mass spectra of new compounds

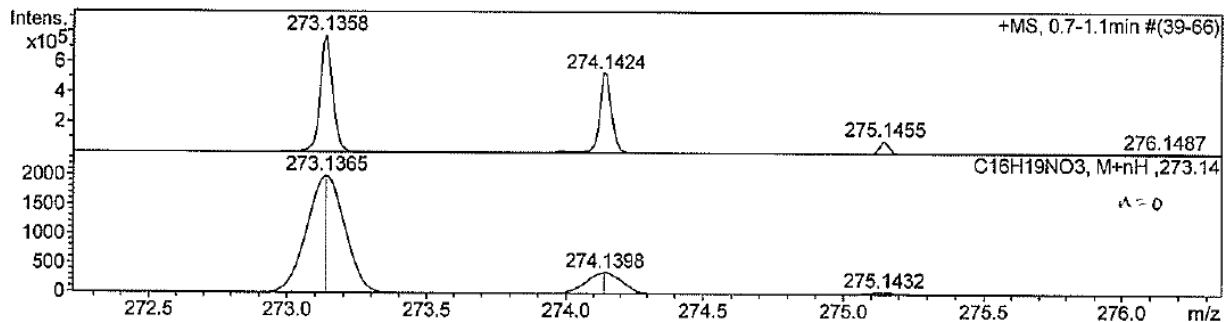


Fig. S60. HR-APCI-TOF mass spectra of S1. Top: observed, bottom: simulated.

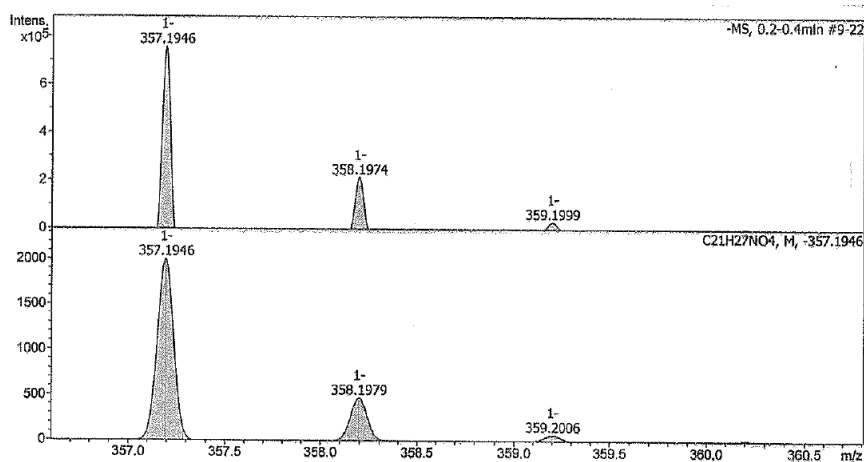


Fig. S61. HR-APCI-TOF mass spectra of S2. Top: observed, bottom: simulated.

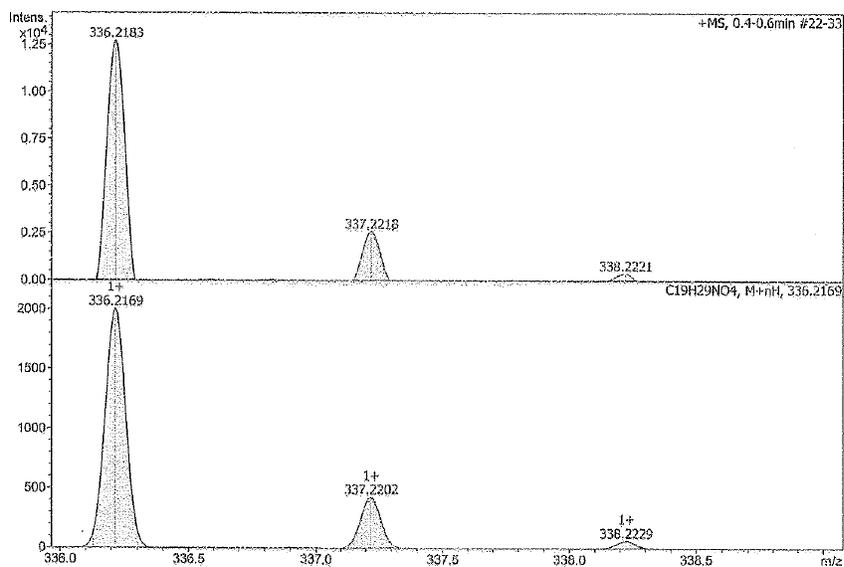
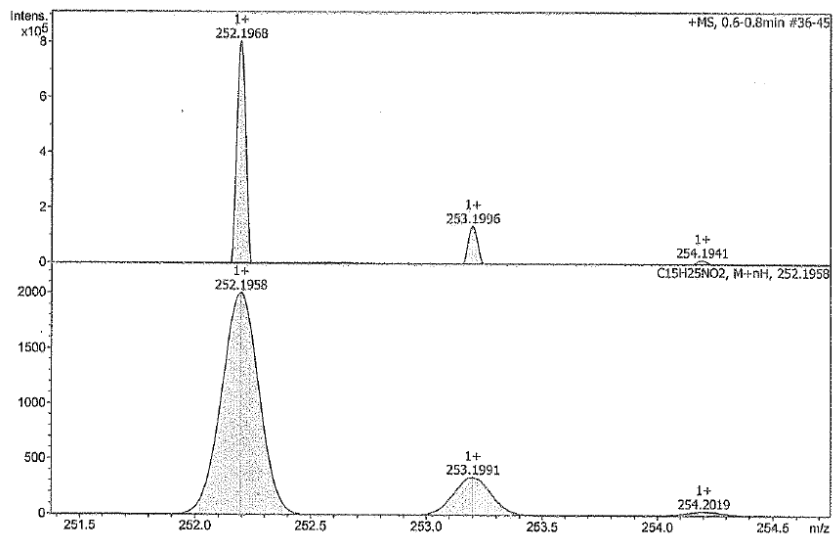
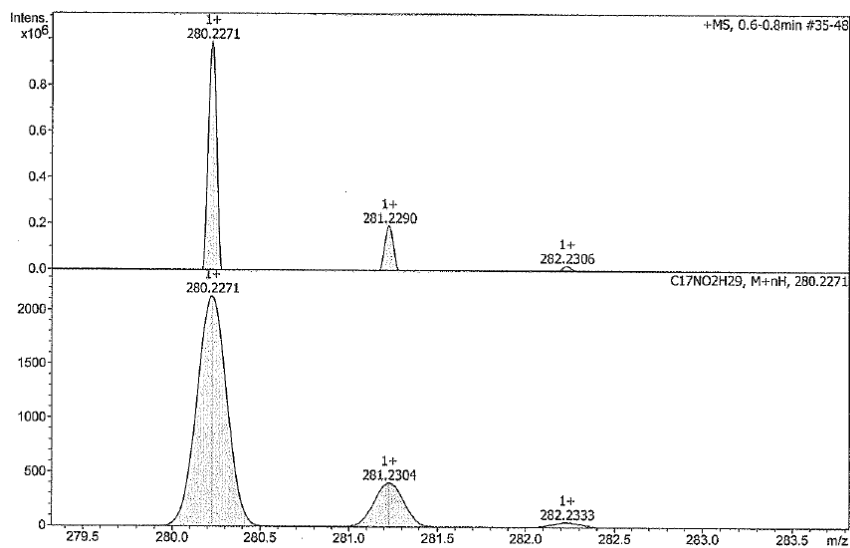


Fig. S62. HR-APCI-TOF mass spectra of S3. Top: observed, bottom: simulated.



**Fig. S63.** HR-APCI-TOF mass spectra of S4. Top: observed, bottom: simulated.



**Fig. S64.** HR-APCI-TOF mass spectra of S5. Top: observed, bottom: simulated.

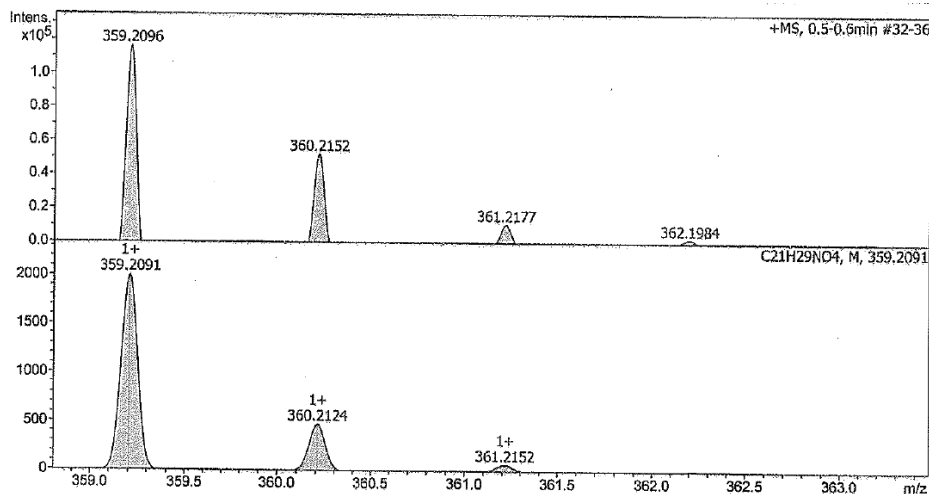


Fig. S65. HR-TOF mass spectra of S6. Top: observed, bottom: simulated.

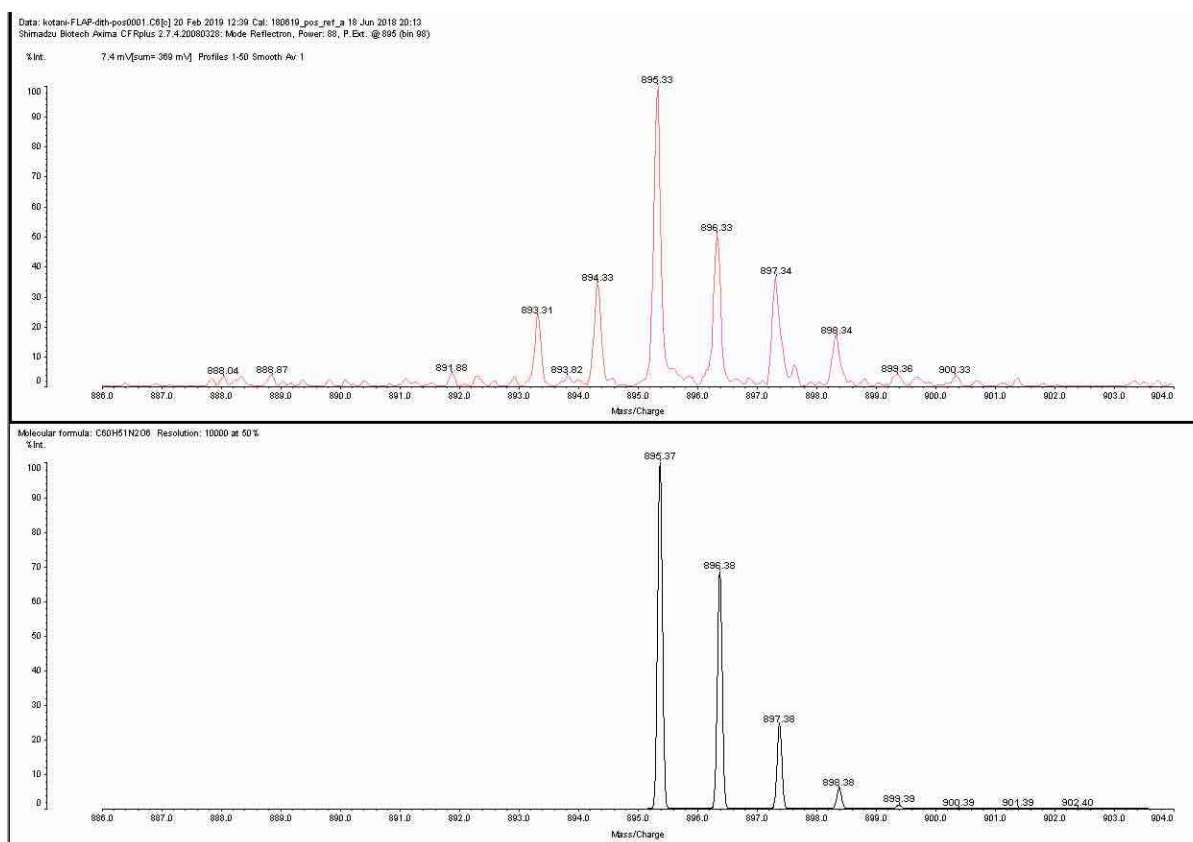
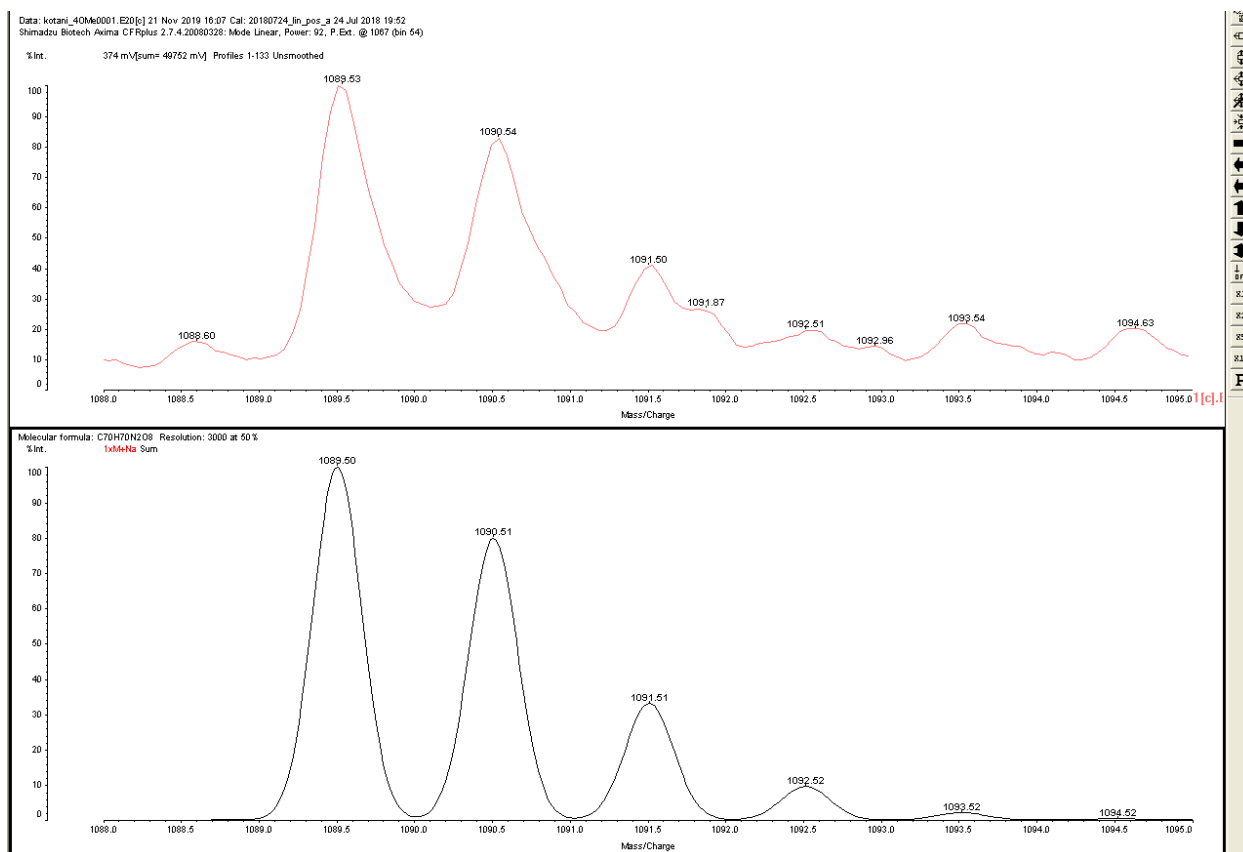
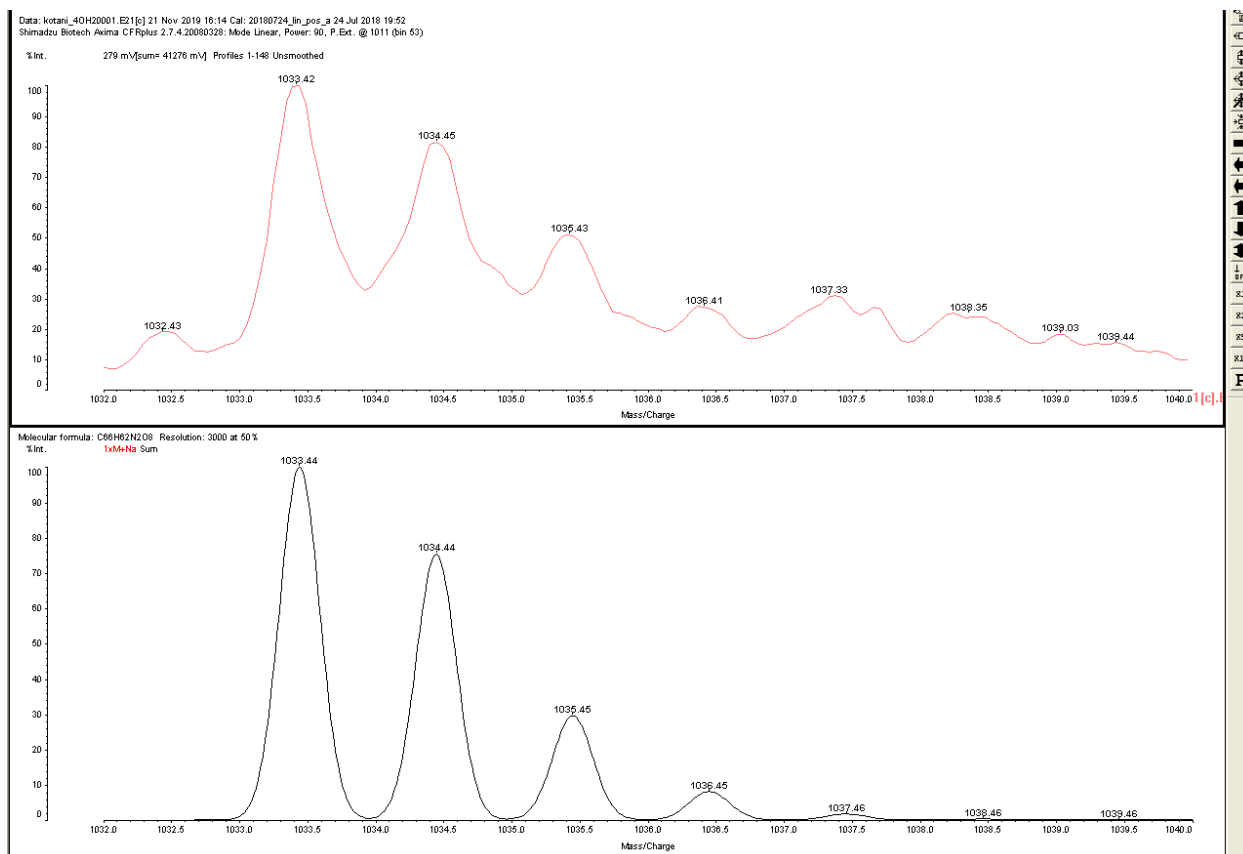


Fig. S66. HR-MALDI-TOF mass spectra of FLAP1. Top: observed, bottom: simulated.



**Fig. S67.** HR-MALDI-TOF mass spectra of **S8**. Top: observed, bottom: simulated.



**Fig. S68.** HR-MALDI-TOF mass spectra of **FLAP2**. Top: observed, bottom: simulated.

## Supplementary References

38. Gaussian 16, Revision A.03, M. J. Frisch, G. W. Trucks, H. B. Schlegel, G. E. Scuseria, M. A. Robb, J. R. Cheeseman, G. Scalmani, V. Barone, G. A. Petersson, H. Nakatsuji, X. Li, M. Caricato, A. V. Marenich, J. Bloino, B. G. Janesko, R. Gomperts, B. Mennucci, H. P. Hratchian, J. V. Ortiz, A. F. Izmaylov, J. L. Sonnenberg, D. Williams-Young, F. Ding, F. Lipparini, F. Egidi, J. Goings, B. Peng, A. Petrone, T. Henderson, D. Ranasinghe, V. G. Zakrzewski, J. Gao, N. Rega, G. Zheng, W. Liang, M. Hada, M. Ehara, K. Toyota, R. Fukuda, J. Hasegawa, M. Ishida, T. Nakajima, Y. Honda, O. Kitao, H. Nakai, T. Vreven, K. Throssell, J. A. Montgomery, Jr., J. E. Peralta, F. Ogliaro, M. J. Bearpark, J. J. Heyd, E. N. Brothers, K. N. Kudin, V. N. Staroverov, T. A. Keith, R. Kobayashi, J. Normand, K. Raghavachari, A. P. Rendell, J. C. Burant, S. S. Iyengar, J. Tomasi, M. Cossi, J. M. Millam, M. Klene, C. Adamo, R. Cammi, J. W. Ochterski, R. L. Martin, K. Morokuma, O. Farkas, J. B. Foresman, and D. J. Fox, Gaussian, Inc., Wallingford CT
39. J. L. Krinsky, A. Martínez, C. Godard, S. Castellón, C. Claver, Modular Synthesis of Functionalisable Alkoxy-Tethered N-Heterocyclic Carbene Ligands and an Active Catalyst for Buchwald–Hartwig Aminations. *Adv. Syn. Cat.* **356**, 460–474 (2014).
40. L. Zhang, X. Ren, Y. Zhang, K. Zhang, Step-Growth Polymerization Method for Ultrahigh Molecular Weight Polymers. *ACS Macro Lett.* **8**, 948–954 (2019).